DEPARTMENT OF AEROSPACE ENGINEERING
COLLEGE OF ENGINEERING AND TECHNOLOGY
OLD DOMINION UNIVERSITY
NORFOLK, VIRGINIA 23529-0247

AN INVESTIGATION OF HIGH-ORDER SHOCK-CAPTURING METHODS FOR COMPUTATIONAL AEROACOUSTICS

By
Dr. Jay Casper and Dr. Oktay Baysal, Principal Investigators

Final Report
February, 1995-March, 1997

Prepared for
National Aeronautics and Space Administration
Langley Research Center
Hampton, VA 23681-0001

Under
Grant# NAG-1-1653
T. L. Thomas, Technical Officer
ODURF #150711

June 1997

DEPARTMENT OF AEROSPACE ENGINEERING
COLLEGE OF ENGINEERING AND TECHNOLOGY
OLD DOMINION UNIVERSITY
NORFOLK, VIRGINIA 23529-0247

AN INVESTIGATION OF HIGH-ORDER SHOCK-CAPTURING METHODS FOR COMPUTATIONAL AEROACOUSTICS

By
Dr. Jay Casper and Dr. Oktay Baysal, Principal Investigators

Final Report
February, 1995-March, 1997

Prepared for
National Aeronautics and Space Administration
Langley Research Center
Hampton, VA 23681-0001

Under
Grant# NAG-1-1653
T. L. Thomas, Technical Officer
ODURF #150711

Submitted by the
Old Dominion University Research Foundation
P.O. Box 6369
Norfolk, VA 23508-0369

June 1997

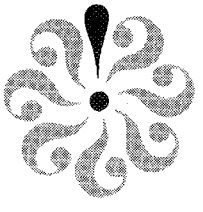

Final Report
NASA Grant NAG1-1653
February, 1995 - March, 1997

AN INVESTIGATION OF HIGH-ORDER SHOCK-CAPTURING METHODS FOR COMPUTATIONAL AEROACOUSTICS

Dr. Jay Casper
Dr. Oktay Baysal
Aerospace Engineering Department
Old Dominion University
Norfolk, Virginia

PROJECT SUMMARY

This project is motivated by the desire to develop numerical methods that will be useful in the study of compressible flows that exhibit aeroacoustic phenomena. Solutions to linear problems have been investigated through the development of a computer code based on the recent dispersion-relation-preserving (DRP) methodology. In regard to nonlinear problems, the class of essentially nonoscillatory (ENO) schemes have been considered as the primary candidates for solving aeroacoustic problems in which discontinuities are involved. Discontinuities in the solution itself (*e.g.* shocks) as well as in the geometry on which the problem is defined have been studied. Two-dimensional nonlinear problems were considered in order to determine if the one-dimensional results obtained in the first phase of this project were extendable to more realistic problems. Conclusions have been drawn in regard to the ability to numerically predict solutions of nonlinear problems with shocks to high-order accuracy.

1. Report Summary

In the remainder of this report, an overview of each of the technical problems and a synopsis of their achievements are presented in Section 2 and Section 3. The details are available in the technical publications listed in Section 4 and are sampled in Section 5

2. High-Order Accurate Methods for Compressible Flows with Shocks

Phase 1 Research

During the first phase of this project, reported in (Casper and Baysal, 1995), a prime objective was to determine the requirements of a numerical to predict a high-order accurate solution of a compressible with shocks. This subsection provides an overview of this Phase 1 work.

A fourth-order accurate ENO-based code was used to investigate the solutions of inviscid, compressible flows with shocks. Design accuracy was achieved in the smooth regions of a steady-state, quasi-one-dimensional, shocked nozzle flow. However, in an unsteady one-dimensional test case, only first-order results were obtained downstream of a sound-shock interaction. Similar results were obtained with a fourth-order compact finite-difference code. The difficulty in obtaining a globally high-order accurate solution to an unsteady discontinuous problem with a shock-capturing method was examined through the study of a simplified, linear model problem. The ENO code was modified with a subcell resolution technique in order to obtain a globally high-order accurate solution. The sound-shock interaction problem was again solved with the modified scheme, and a globally fourth-order accurate solution was achieved. Details of this research can be found in (Casper and Carpenter, 1995).

In addition to questions concerning the accuracy of discontinuous flows, the issue of discontinuous geometries was also a topic of interest. The performance of a fourth-order ENO method was tested on smooth solutions defined on piecewise smooth geometries. The propagation of sound in a quasi-one-dimensional nozzle was considered as a test case. Not only was the geometry for this problem not smooth to the order of the numerical scheme, the mesh was a discontinuous function of the nozzle length. The code was modified through the adaptive stencil strategy employed by ENO methods. The solution's accuracy, with respect to entropy,

was found to be fourth-order accurate, as per the design of the numerical scheme. Details of this research can be found in (Casper, 1995).

Phase 2 Research

The difficult issues raised by the results obtained in Phase 1 are topics of the second phase of this project and are discussed below. The sound-shock interaction was revisited, in order to study the relative merits of linear and nonlinear methods, as well as to quantify the behavior exhibited by these methods in the presence of solution discontinuities. The issue of extension of these methods to more than one spatial dimension was also of concern. Because the extension of subcell resolution techniques to multiple spatial dimensions is impractical, the relative merits of high-order shock-capturing methods had to be reconsidered. A two-dimensional problem was solved in order to compare various methods for their accuracy with respect to their shock resolution.

A sixth-order compact finite-difference scheme was used to investigate various one-dimensional, discontinuous flows: steady-state flow in a nozzle, sound-shock interaction, time-dependent Burgers' equation, and a linear model problem. The results obtained from the solution of the Euler equations reaffirmed the conclusions from the previous research reported in (Casper and Carpenter, 1995). It was found that, although both the linear compact scheme and the fourth-order ENO method were high-order accurate in the steady Euler case, the ENO results were significantly better, perhaps owing to the ability to capture shock in a nonoscillatory fashion. For both schemes, the unsteady Euler solutions were only first-order accurate downstream of the shock. However, the solution of the unsteady Burgers' equation was found to be of design accuracy away from the discontinuity. An interesting result was obtained by revisiting the linear model problem with discontinuous wave speed. It was found that the first-order error made across the discontinuity was largely a phase error, and that post-processing would enable second-order accuracy to be recovered. Details of this research can be found in (Carpenter and Casper, 1996).

A fourth-order compact finite-difference scheme and a third-order ENO scheme were used to predict the two-dimensional, steady flow around a supersonic cylindrical projectile. Because of the previous research that obtained high-order results for a steady one-dimensional shocked flow, high-order results might have been expected for the two-dimensional steady case. However, high-order accuracy was obtained with the ENO method only when the shock was aligned with the computational mesh, in which case the problem becomes one-dimensional. When the problem is determined such that the shock is skew to the mesh, only first-order accuracy is obtained. It

was concluded that such errors are inherent in numerical shock-capturing methods, as presently understood. A better understanding of high-order accurate shock-capturing methods in a general multi-dimensional context will be required before CFD can play a significant role in aeroacoustic applications that involve flows with shocks. Details of this research can be found in (Carpenter and Casper, 1997).

Copies of all reports pertaining to the results obtained from the research associated with this project are included in Section 5.

3. Low-Dispersion Schemes for the Direct Computation of Acoustic Wave Propagati on

Computational aeroacoustics (CAA) may be defined as the application of numerical techniques for the direct calculation of aerodynamic sound generation and propagation starting from the first principles. Most computational fluid dynamics (CFD) schemes, however, are not adequately accurate for solving the aeroacoustics problems (Lighthill, 1992). Their amplitudes are often orders of magnitude smaller, and yet the frequencies are orders of magnitude larger than the flow field variations generating the sound. Further, high-fidelity is paramount for the resolution of acoustic problems; but a consistent, stable, and convergent, high-order scheme is not necessarily dispersion-relation preserving and thus does not necessarily guarantee a good quality numerical wave solution for an acoustic problem. Hence, among the requirements that should be placed on a CAA algorithm are the minimal dispersion and dissipation features.

Therefore, a fourth-order accurate dispersion-relation-preserving (DRP) method (Tam and Webb, 1993) was previously developed for a variety of wave propagation problems by solving the linearized Euler equations. Evaluation of the developed baseline algorithm and the spectral analysis methods for time-series data were reported in a paper (Vanel and Baysal, 1995). In this investigation, a number of observations and recommendations were made for future investigations to extend the scheme to solve some application problems. The present investigation started precisely with this impetus.

The major point of the work accomplished in the first year was a robust low-dispersion-method for the linear Euler equations which was also relatively more versatile and efficient:

(i) The previously written computer code (Baysal, 1995a, Vanel and Baysal, 1995) for the 2D DRP algorithm has been completely revised for a number of reasons. The new version is written using dynamic memory allocations, for example, and it is more tailored to run on workstations.

(ii) The boundary condition routines for the linear DRP method (radiation and outflow boundary conditions) have been complemented for solid walls.

(iii) For improved wave propagation simulations, selective artificial damping has been incorporated and thoroughly tested. The user can now select the band of the error that is wished to be suppressed.

(iv) The method has been tested for various types initial-value and periodic problems generating incident and reflected waves off the walls either inside of the domain or on a side of the domain (from The First Workshop on Benchmark Problems, Hardin et al., 1995).

(v) The method has been extended and the optimized coefficients have been derived for a spatially sixth-order accurate scheme. The spurious waves and nonisotropicity has been reduced to about machine zero.

(vi) The linearized diffusion terms have been derived and discretized with the DRP scheme and the scheme has been extended for the linearized 2D Navier-Stokes equations.

(vii). An optimized, variable-order Runge-Kutta method has been implemented as a low-storage alternative to the time integration method.

(viii) The extension of the method has been successful for the generalized curvilinear coordinates.

Several issues were investigated. Among them were higher-order accuracy, choice of boundary conditions and differencing stencils, effects of viscosity, low-storage time integration, generalized curvilinear coordinates, periodic sources, their reflections and interference patterns from a flat wall and scattering from a circular cylinder. The results were found to be promising en route to the aeroacoustic simulations of realistic engineering problems.

In the second year of the project, the major points of achievement were solving the scattering problems given in the Second Workshop on Benchmark Problems (Hardin and Tam, 1996, 1997), and the nonlinear wave propagation. By and large, the simulations of the propagation of acoustic waves, their reflections and scattering, in particular, the initial-value problem with the acoustic pulse, were successful (Baysal and Kaushik, 1997). Two necessary building blocks to success, once a suitable CAA scheme was selected, were the correct boundary conditions, and an adequate and efficient grid. Notwithstanding the imperfectly orthogonal grids and the required transformation metrics, employing the body-fitted coordinates allowed a straight forward implementation of the boundary conditions.

There are certain important applications, e.g. the jet screech in a wake-vortex interaction flow, boundary layer noise, cavity noise, etc., where the assumption of linear wave propagation in uniform flow would be too compromising. Therefore, the linear dispersion-relation-preserving scheme and its boundary conditions were extended for the nonlinear Euler equations (Baysal et al., 1997). This allows computing, a nonuniform flowfield and a nonlinear acoustic wave propagation in such a medium, by the same scheme. By casting all the equations, boundary conditions, and the solution scheme in generalized curvilinear coordinates, the solutions were made possible for non-Cartesian domains and, for the better deployment of the grid points, nonuniform grid step sizes are also possible.

The methodology has been tested for a number of simple initial-value and periodic-source problems. The wall boundary condition derived from the momentum equations and implemented through a pressure at a ghost point, and the radiation boundary condition derived from the asymptotic solution to the Euler equations, were shown to be effective for the nonlinear equations and nonuniform flows. The non-reflective characteristic boundary conditions had success limited to the nonlinear waves in no mean flow, and failed for nonlinear waves in nonuniform flow.

The methods are now being used to simulate the following two "simplified application" problems: a) noise generated by a 2D, steady, supersonic jet flow, b) noise generated by a 2D cavity flow.

Finally, copies of the papers reporting the results of this project are enclosed in Section 5.

Principal Investigator: Dr. Jay Casper

Co-Principal Investigator: Dr. Oktay Baysal

4. References

Baysal, O., 1995a, "Final Report for the NASA Langley RC Grant NAG-1-1499," Old Dominion University Research Foundation, Norfolk, VA, December.

Baysal, O., and Kaushik, D.K., 1997, "Computation of Acoustic Scattering by a Low-Dispersion Scheme," NASA-CP xxxx, Proceedings of Second Computational Aeroacoustics Workshop on Benchmark Problems, (Nov. 1996), Tallahassee, FL, April. (support under NAG-1-1653) - copy enclosed

Baysal, O., Kaushik, D.K., and Idres, M., 1997, "Low Dispersion Scheme for Nonlinear Acoustic Waves in Nonuniform Flow," AIAA Paper 97-1582, Proceedings of Third CEAS/AIAA Aeroacoustics Conference, Atlanta, GA, pp. 10-18. (support under NAG-1-1653) - copy enclosed

Casper, J., 1995, "Using High-Order Methods on Lower-Order Geometries," Shock Wave," *Proceedings of the Forum on Computational Aeroacoustics, ASME/JSME Fluids Engineering Annual Conference*, Hilton Head, S.C., August, 1995.

Casper, J., and Baysal, O., 1995, "An Investigation of High-Order Shock Capturing Methods for Computational Aeroacoustics," Annual Progress Report for the NASA Langley RC Grant NAG-1-1653, Old Dominion University Research Foundation, Norfolk, VA, October.

Casper, J. and Carpenter, M. 1995, "Computational Considerations for the Simulation of Shock-Induced Sound," NASA Technical Memorandum, NASA Langley Research Center, Hampton, VA, July, 1995. Also, to appear in SIAM Journal for Scientific Computing, Vol. 19, No. 1, January, 1998 - copy enclosed.

Casper, J. and Carpenter, M. 1996, "Computational Considerations for the Simulation of Discontinuous Flows," Proceedings of the Second ICASE/LaRC Industrial Roundtable, October, 1996, Hussani, et. al., eds. - copy enclosed.

Casper, J. and Carpenter, M. 1997, "The Accuracy of Shock Capturing in Two Spatial Dimensions," AIAA-97-2107, to appear in the Proceedings of the 13th Computational Fluid Dynamics Conference, June 29-July 2, 1997 - copy enclosed.

Hardin, J.C., Ristorcelli, J.R., and Tam, C.K.W., (Editors), 1995, ICASE/LaRC Workshop on Benchmark Problems in Computational Aeroacoustics, NASA Conference Publication 3300.

Hardin, J.C., and Tam, C.K.W., (Editors), 1997, Proceedings of Second Computational Aeroacoustics Workshop on Benchmark Problems , NASA Conference Publication xxxx.

Kaushik, D.K., and Baysal, O., 1996, "Algorithmic Extensions of Low-Dispersion Scheme and Modeling Effects for Acoustic Wave Simulation," Proceedings The ASME Fluids Engineering Division Summer Meeting, FED-Vol. 238, San Diego, CA, pp. 503-510. (support under NAG-1-1653) - copy enclosed

Lighthill, J., 1992, "Report on the Final Panel Discussion on Computational Aeroacoustics," ICASE Report No. 92-53, NASA Langley Research Center, Hampton, VA.

Vanel, F.O., and Baysal, O., 1995, "Investigation of Dispersion-Relation-Preserving Scheme and Spectral Analysis Methods for Acoustic Waves," Proceedings of 1st CEAS/AIAA Aeroacoustics

Conference, Munich, Germany, Jun. 10-14, 1995, pp. 675-682. Also, [ASME] Journal of Vibration and Acoustics, Vol. 119, No. 2, Apr. 1997, pp. 250-257. (support under NAG-1-1150 and NAG-1-1499) - copy enclosed

5. Publications (left blank intentionally; please see the following pages)

AIAA 97-1582 CP

Low-Dispersion Scheme for Nonlinear Acoustic Waves in Nonuniform Flow

Oktay Baysal, Dinesh K. Kaushik, and Moumen Idres

Aerospace Engineering Department
Old Dominion University
Norfolk, Virginia 23529-0247

(performed under NASA Grant NAG-1-1653)

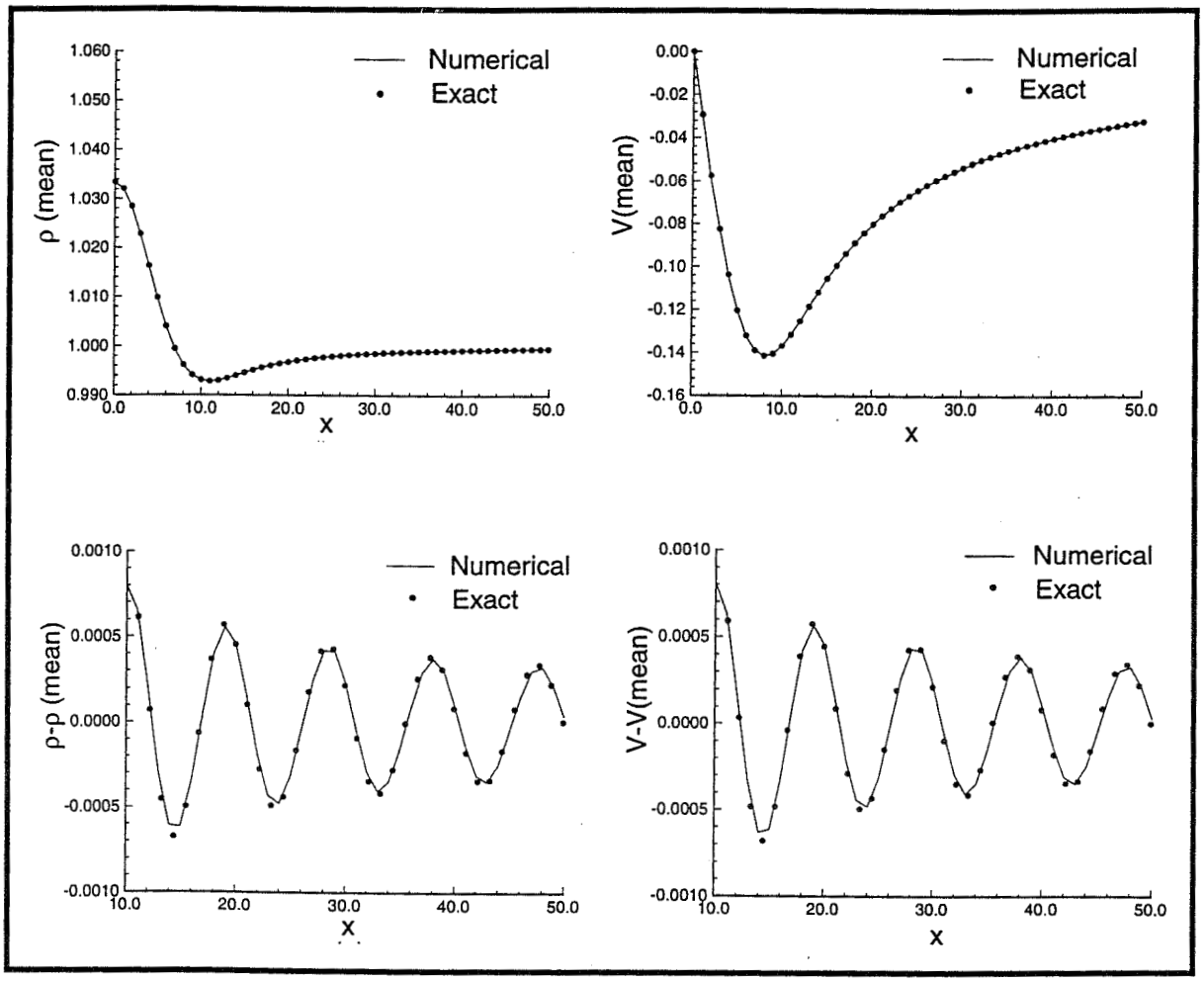

Preprint from Proceedings

3rd AIAA/CEAS Aeroacoustics Conference
May 12-14, 1997 / Atlanta, Georgia

AIAA 97-1582 CP
Proceedings of 3rd AIAA/CEAS Aeroacoustics Conference
May 1997 / Atlanta, GA

LOW-DISPERSION SCHEME FOR NONLINEAR ACOUSTIC WAVES IN NONUNIFORM MEAN FLOW

Oktay Baysal,* Dinesh K. Kaushik,** and Moumen Idres**

Aerospace Engineering Department
Old Dominion University
Norfolk, Virginia 23529-0247 USA

The linear dispersion-relation-preserving scheme and its boundary conditions have been extended to the nonlinear Euler equations. This allowed computing, a nonuniform flowfield and a nonlinear acoustic wave propagation in such a medium, by the same scheme. By casting all the equations, boundary conditions, and the solution scheme in generalized curvilinear coordinates, the solutions were made possible for non-Cartesian domains and, for the better deployment of the grid points, nonuniform grid step sizes could be used. It has been tested for a number of simple initial-value and periodic-source problems. A simple demonstration of the difference between a linear and nonlinear propagation was conducted. The wall boundary condition, derived from the momentum equations and implemented through a pressure at a ghost point, and the radiation boundary condition, derived from the asymptotic solution to the Euler equations, have proven to be effective for the nonlinear equations and nonuniform flows. The nonreflective characteristic boundary conditions also have shown success but limited to the nonlinear waves in no mean flow, and failed for nonlinear waves in nonuniform flow.

Introduction[1]

There are certain aeroacoustics applications, e.g. the jet screech in a wake-vortex interaction flow, boundary layer noise, cavity noise, where the assumption of *linear* wave propagation in *uniform* flow would be too compromising. Consequently, there were some recent progress in the attempts to compute the propagation of *nonlinear* acoustic waves in a *nonuniform* flowfield using high-order schemes. For example, Tam and Shen[1] have reported some extensions of a dispersion-relation-preserving scheme[2] in this direction and solved the inviscid Burger's equation.

Considering accuracy as well as efficiency, some success has so far been reported in direct computations, but they are predominantly limited to modeled periodic noise generation and propagation by assuming linear waves in uniform flow.[3,4] In addition to the cases reported in the First and Second CAA Workshops on Benchmark Problems,[3,4] the authors have shown some successful applications with low-dispersion schemes by solving the linearized Euler or Navier-Stokes equations.[5-7] However, these equations would not be able to represent an aeroacoustic phenomenon, such as, that observed in the case of a high-speed flow past a cavity[8] or the engine internal noise.[9] One way to approach such problems would require the nonlinear equations, and the extension of low-dispersion, high-order schemes and boundary conditions for these equations. This is precisely the goal of the present paper, albeit a modest step in that direction.

Methodology

The present model employs the two-dimensional, compressible, nonlinear Euler equations. Their nondimensionalized and nonconservation form is derived in the generalized curvilinear coordinates. It is contended that, unless strong gradients are expected in the nonuniform mean flow, there should not be discernible differences in employing the equations in conservation or non-conservation forms[1]:

$$Q_t = -R(Q) + S \ , \text{ where } R(Q) = EQ_\xi + FQ_\eta \tag{1}$$

and

$$Q = \begin{bmatrix} \rho \\ u \\ v \\ p \end{bmatrix} , \quad E = \begin{bmatrix} U & \rho\xi_x & \rho\xi_y & 0 \\ 0 & U & 0 & \frac{\xi_x}{\rho} \\ 0 & 0 & U & \frac{\xi_y}{\rho} \\ 0 & \gamma p\xi_x & \gamma p\xi_y & U \end{bmatrix} \tag{2a}$$

$$F = \begin{bmatrix} V & \rho\eta_x & \rho\eta_y & 0 \\ 0 & V & 0 & \frac{\eta_x}{\rho} \\ 0 & 0 & V & \frac{\eta_y}{\rho} \\ 0 & \gamma p\eta_x & \gamma p\eta_y & V \end{bmatrix} , \quad S = \begin{bmatrix} s \\ \frac{-u}{\rho}s \\ \frac{-v}{\rho}s \\ \frac{\gamma p}{\rho}s \end{bmatrix} \tag{2b}$$

$$U = u\xi_x + v\xi_y \ , \quad V = u\eta_x + v\eta_y \ . \tag{3}$$

The density (ρ), pressure (p), and velocity (u,v) are normalized using the freestream values of speed of sound (a_∞) and density. The length is normalized either by the step size (Δx) or the cylinder diameter (D). The metric terms (ξ_x, etc.) are computed analytically for the simple grid cases considered herein.

---

*Professor and Eminent Scholar. Associate Fellow, AIAA.
**Graduate Research Assistant.

For the spatial integration, the dispersion-relation-preserving scheme,[2] which was demonstrated for various linear cases,[5-7] is now extended for the nonlinear equations in generalized coordinates. Even with second-order schemes,[8] when used in resolving the highly nonlinear flow or acoustic phenomena, it is common to have limiters or artificial damping mechanisms, either implicit in the scheme (upwind schemes) or explicitly added (central schemes). Since simulating low-amplitude acoustic waves for a long time and for many wavelengths of travel is the objective in CAA, devising such artificial damping mechanisms requires extreme care. Constant damping over all wave numbers need to be avoided; rather, selective damping,[10] which has small damping over the long wave range but significant damping in the short wave range, should be devised. The present central-difference scheme includes similar terms ($D^n_{\ell,m}$) to overcome the expected spurious oscillations in a highly nonlinear region:

$$(\frac{\partial Q}{\partial t})^{n+1}_{\ell,m} = -R^n_{\ell,m} + S^n_{\ell,m} + D^n_{\ell,m} \ , \qquad (4)$$

where

$$R^n_{\ell,m} = \frac{1}{\Delta\xi}[E^n_{\ell,m} \sum_{j=-N}^{M} a_j Q^n_{\ell+j,m}] + \frac{1}{\Delta\eta}[F^n_{\ell,m} \sum_{j=-N}^{M} a_j Q^n_{\ell,m+j}] \qquad (5)$$

and

$$D^n_{\ell,m} = \frac{-1}{\mathrm{Re}_D} \sum_{j=-N}^{N} d_j [\frac{1}{\Delta\xi^2} Q^n_{\ell+j,m} + \frac{1}{\Delta\eta^2} Q^n_{\ell,m+j}], \ \mathrm{Re}_D = \frac{a_\infty D}{\upsilon_a}. \qquad (6)$$

In eqs. (4) to (6), ℓ and m are the spatial indices and n indicates the time level. The coefficients a_j and d_j were computed by minimizing the dispersion-relation error.[5-7] For N=M, difference is central, for N=0, it is fully forward, and for M=0, it is fully backward. However, since these high-order stencils require multiple layers of boundary cells, all combinations between a central and a fully-one-sided difference need also be derived. Only then, it would be possible to always utilize the information from the nearest possible points for better accuracy. In the present computations, a fourth-order scheme was used, requiring 7-point stencils: N takes values from 6 to 0, M takes values from 0 to 6, and N+M=6. The interior cells were computed using central differences with N=M=3.

For the temporal integration, a low-storage, low-dispersion Runge-Kutta scheme,[11] which was previously,[6,7] demonstrated for various linear cases, is now extended for the nonlinear equations in generalized coordinates:

$$Q^{(0)} = Q^n, \ Q^{(i)} = Q^{(0)} - \beta_i \Delta t (\frac{\partial Q}{\partial t})^{(i-1)} \ ,$$
$$Q^{n+1} = Q^{(p)}, \ i = 1,2,..,p \qquad (7)$$

The indices p and i indicate the order and the stage of the method, respectively. As for the coefficients, β_1 =0 and the other coefficients β_i were determined from,

$$c_i = \prod_{k=2}^{i} \beta_{p-k+2}, \quad i = 2,...,p \ . \qquad (8)$$

The coefficients c_i were computed by considering the amplification factor of the Runge-Kutta scheme, then minimizing the dispersion-relation error. The time steps were determined from the stability as well as the accuracy limits. In the present study, a five-stage (p =5) Runge-Kutta was used, which required two levels of storage and it was at least second-order accurate.

One of the challenges en route to the objective was clearly the implementation of the boundary conditions. Although a number of papers have already reported various types of nonreflecting or absorbing boundary conditions, in representing all forms of waves in nonuniform mean flow, even at the boundary, few were derived for the Euler equations. The boundary conditions proposed by Tam and Dong[12] also assume weakly nonuniform flow at the boundary, hence can be based on the asymptotic solutions. Further, it requires some knowledge of the total mass flux in constructing the mean flow quantities. An improvement by Dong and Mankbadi[9] has eliminated the latter but not the former impediment. Further analysis of this proposed improvement is reported by Dong.[13] The present method implemented these boundary conditions.

Radiation boundary conditions are derived from the asymptotic solutions,[12,13] assuming the mean flow is only weakly nonhomogeneous and, in the farfield, the outgoing disturbances are propagating in the radial direction relative to the noise source at speed V_W. Denoting the acoustic field properties as the difference between the total (Q) and the mean ($\overline{Q}$) properties, they are:

$$\frac{\partial Q}{\partial t} + A\frac{\partial (Q-\overline{Q})}{\partial \xi} + B\frac{\partial (Q-\overline{Q})}{\partial \eta} + C(Q-\overline{Q}) = 0 \qquad (9)$$

where

$$A = V_w \frac{x\xi_x + y\xi_y}{r}, \ B = V_w \frac{x\eta_x + y\eta_y}{r}, \ C = \frac{V_w}{2r}, \ r = \frac{1}{D}\sqrt{x^2+y^2} \qquad (10)$$

$$V_w = \overline{u}\cos\theta + \overline{v}\sin\theta + \sqrt{\overline{a}^2 - (\overline{u}\sin\theta - \overline{v}\cos\theta)^2} \qquad (11)$$

In addition to the acoustic waves, however, vorticity and entropy waves also reach the downstream boundary. For the pressure, the outflow boundary condition,[12] is still derived from eq. (9). However, the density and velocity, lumped into a vector, Q', are derived to be as follows:

$$\frac{\partial Q'}{\partial t} + \hat{M}(Q' - \overline{Q}') = rhs \ , \ \text{where} \ \ \hat{M} = U\frac{\partial}{\partial \xi} + V\frac{\partial}{\partial \eta} \qquad (12)$$

and

$$rhs = [\frac{1}{\overline{a}^2}\frac{\partial p}{\partial t} + \hat{M}(\frac{p-\overline{p}}{\overline{a}^2}), -\frac{1}{\rho}(\xi_x \frac{\partial (p-\overline{p})}{\partial \xi} + \eta_x \frac{\partial (p-\overline{p})}{\partial \eta}),$$
$$-\frac{1}{\rho}(\xi_y \frac{\partial (p-\overline{p})}{\partial \xi} + \eta_y \frac{\partial (p-\overline{p})}{\partial \eta})]^t \qquad (13)$$

To maintain the impermeability at , for example, an $\eta = 0$ solid wall, the normal contravariant velocity is set to zero, $V = \eta_x u + \eta_y v = 0$. Using this condition, an equation for the normal pressure gradient is obtained from the two momentum equations,

$$\frac{\partial p}{\partial \eta} = \frac{-1}{(\eta_x^2+\eta_y^2)}[\rho U(\eta_x \frac{\partial u}{\partial \xi} + \eta_y \frac{\partial v}{\partial \xi}) + p_\xi(\eta_x \xi_x + \eta_y \xi_y)]. \quad (14)$$

By DRP-type finite differencing,[14] this equation at time level n and wall location (ℓ, w), provides the ghost point value (subscript -1) of pressure:

$$p_{\ell,-1} = \frac{-1}{a_{\ell,-1}}[\sum_{j=0}^{N+M-1} a_j p_{\ell,j}] - \frac{\Delta\eta}{a_{\ell,-1}(\eta_x^2+\eta_y^2)_{\ell,w}} \times \{\frac{(\rho U)_{\ell,w}}{\Delta\xi}[(\eta_x)_{\ell,w} \sum_{j=-N}^{M} a_j u_{\ell+j,w} + (\eta_y)_{\ell,w} \sum_{j=-N}^{M} a_j v_{\ell+j,w}] + \frac{(\eta_x\xi_x + \eta_y\xi_y)_{\ell,w}}{\Delta\xi} \sum_{j=-N}^{M} a_j p_{\ell+j,w}\} \quad . \quad (15)$$

In order to derive the nonreflecting characteristic boundary conditions as an alternative to all of the above, first a locally one-dimensional ($\xi^i, i = 1,2$) flow is assumed, then the Euler equations are written in their characteristic form,[15]

$$\frac{\partial p}{\partial t} \mp \rho a \frac{\partial U}{\partial t} + \Gamma^i_{1,3} = 0, \quad \frac{\partial p}{\partial t} - a^2 \frac{\partial \rho}{\partial t} + \Gamma^i_2 = 0 \quad (16)$$

where

$$\Gamma^i_{1,3} = (U^i \mp a)[\frac{\partial p}{\partial \xi^i} \mp \rho a \frac{\partial U^i}{\partial \xi^i}], \quad \Gamma^i_2 = U^i[\frac{\partial p}{\partial \xi^i} - a^2 \frac{\partial \rho}{\partial \xi^i}] \quad (17)$$
$$i = 1,2 \ (no\ sum)$$

In order to have a nonreflecting condition,[15,16] at a given grid point on a boundary, the local perturbations propagated along incoming (to computational domain) characteristics are made to vanish, and perturbations along outgoing characteristics are computed by the one-sided DRP differences. This requires checking the local Mach number ($M^i \equiv \frac{U^i}{a}$), and the signs of the directed unit normal ($\vec{n}^i = \frac{\nabla\xi^i}{|\nabla\xi^i|}$, *no sum*) and its scalar product with the normal contravariant velocity ($\bar{U}^i = \sum_{j=1}^{2} u^j \frac{\partial \xi^i}{\partial x^j} \hat{e}_i$). The tests for the proper choice at a given boundary point in the computational plane are summarized in table 1.

Results

Previously,[5-7] the *linear* algorithm was developed and demonstrated for the following test cases in *uniform* flow: (a) single acoustic pulse, (b) three successive acoustic pulses, (c) two simultaneous acoustic pulses, (d) acoustic pulse near a flat wall, (e) periodic source near a flat wall with and without a circular bump, (f) acoustic pulse near a circular cylinder (scattering problem), (g) *periodic* source near a circular cylinder (scattering problem). The present *nonlinear* algorithm and its boundary conditions are now being evaluated by considering the following numerical examples (table 2): (1) acoustic pulse generated wave propagation computed by the nonlinear algorithm contrasted with that by the linear algorithm;[5-7] (2) acoustic pulse reflected from a flat plate computed with the nonreflective characteristic boundary conditions compared with the solution using radiation boundary conditions; (3) acoustic pulse reflected from a bump on a flat plate; and (4) *periodic* acoustic source in a potential sink (*nonuniform*) flow.

The acoustic waves were generated either by a periodic source to generate both the nonuniform mean flow and the acoustic waves,

$$s(x,y,t) = \bar{s} + s' \cos \omega t \quad (18)$$

where

$$\bar{s} = -\bar{\varepsilon} \exp\{-\bar{\sigma}[(x-x_s)^2 + (y-y_s)^2]\} \quad (19a)$$

$$s' = \varepsilon \exp\{-\sigma[(x-x_s)^2 + (y-y_s)^2]\} \quad (19b)$$

$$\bar{\sigma} \equiv \frac{\ln 2}{\bar{b}^2}, \quad \sigma \equiv \frac{\ln 2}{b^2} \quad . \quad (19c)$$

or by an initial acoustic pulse introduced to the field at $t = 0$ by setting $u = v = 0$ and $s(x,y) = s'$. In eq. (18), the frequency is $\omega = 0.2\pi$ and the rest of the parameter values are given in table 2 for each case.

The propagation in a no mean flow medium of the acoustic waves generated by the pulse (case 1), are presented in fig. 1. When computed by the linear equations,[5-7] the waves travel at a constant speed, hence preserving their shape. Their convection velocity, when computed by the nonlinear equations (1), is a function of local state properties, which in turn, are functions of space and time. This results in a successor wave point taking over the predecessor wave point, manifesting in an ever steepening wave front (fig. 1). For case 2, a solid wall is added as the lower boundary of the domain (figs. 2 and 3). The interference pattern of the incident and the reflected waves is computed by the nonlinear algorithm. Until the waves reach the non-solid boundaries, there virtually is no difference between the two solutions. From t =54 and on, minor differences between the nonreflective characteristic boundary conditions (fig. 2 and eq. (16)) and the radiation boundary conditions (fig. 3 and eq. (9)), are visible.

To generate reflected waves that are nonsimilar to the incident waves, and to check the success of the algorithm with non-rectangular boundaries, hence requiring non-Cartesian treatments, such as, the curvilinear coordinates employed herein, in case 3, a circular bump is placed on the flat plate (fig. 4). The nonlinear wave propagation and the interference are successfully computed with the present algorithm and the radiation boundary condition.

In case 4, a nonuniform flow is generated by placing a potential sink ($\bar{s}$ in eq. (18)) and computed by

the present nonlinear algorithm. The residual is driven to the machine zero (fig. 5a), and the computed distributions of density and velocity along the x-axis are successfully compared with the exact solution[12] (fig. 5). Then, the acoustic waves generated by the periodic source are computed and their nonlinear propagation (distributions of $\rho_{acoustic} = \rho - \overline{\rho}$ and $V_{acoustic} = V - \overline{V}$) are compared (fig. 6) with the exact solution.[12-13]

Conclusions

The linear dispersion-relation-preserving scheme and its boundary conditions have been extended to the nonlinear Euler equations. This allowed computing, a nonuniform flowfield and a nonlinear acoustic wave propagation in such a medium, by the same scheme. By casting all the equations, boundary conditions, and the solution scheme in generalized curvilinear coordinates, the solutions were made possible for non-Cartesian domains and, for the better deployment of the grid points, nonuniform grid step sizes could be used.

The method has been tested for a number of simple initial-value and periodic-source problems. A simple demonstration of the difference between a linear and nonlinear propagation was conducted. The wall boundary condition derived from the momentum equations and implemented through a pressure at a ghost point, and the radiation boundary condition derived from the asymptotic solution to the Euler equations, have proven to be effective for the nonlinear equations and nonuniform flows. The nonreflective characteristic boundary conditions also have shown success but limited to the nonlinear waves in no mean flow, and failed for nonlinear waves in nonuniform flow.

Currently, work is in progress to further improve the boundary conditions. Also, the scheme is being extended to improve its computational efficiency.

References

1. Tam, C.K.W., and Shen, H., 1993, "Direct Computation of Nonlinear Acoustic Pulses using Higher-Order Finite Difference Schemes," Paper 93-4325, 15th AIAA Aeroacoustics Conference, Long Beach, CA.
2. Tam, K. W., and Webb, J. C., 1993, "Dispersion-Relation-Preserving Finite Difference Schemes for Computational Acoustics," *Journal of Computational Physics*, Vol. 107, pp. 262-283.
3. Hardin, J.C., Ristorcelli, J.R., and Tam, C.K.W., (Editors), 1995, ICASE/LaRC Workshop on Benchmark Problems in Computational Aeroacoustics, NASA Conference Publication 3300.
4. Hardin, J.C., and Tam, C.K.W., (Editors), 1997, Proceedings of Second Computational Aeroacoustics Workshop on Benchmark Problems , NASA Conference Publication xxxx.
5. Vanel, F. O., and Baysal, O., 1995, "Investigation of Dispersion-Relation-Preserving Scheme and Spectral Analysis Methods for Acoustic Waves," *Journal of Vibration and Acoustics*, Vol. 119, No. 2, April 1997.
6. Kaushik, D.K., and Baysal, O., 1996, "Algorithmic Extensions of Low-Dispersion Scheme and Modeling Effects for Acoustic Wave Simulation," Proceedings The ASME Fluids Engineering Division Summer Meeting, FED-Vol. 238, San Diego, CA, pp. 503-510.
7. Baysal, O., and Kaushik, D.K., 1997, "Computation of Acoustic Scattering by a Low-Dispersion Scheme," NASA-CP xxxx, Proceedings of Second Computational Aeroacoustics Workshop on Benchmark Problems, Tallahassee, FL, Nov. 1996.
8. Baysal, O., Yen, G.W., and Fouladi, K., 1992, "Navier-Stokes Computations of Cavity Aeroacoustics With Suppression Devices," *Journal of Vibration and Acoustics*, Vol. 116, No. 1, pp. 105-112.
9. Dong, T.Z., and Mankbadi, R.R., 1995, "Direct Numerical Simulation of Engine Internal Noise Propagation and Radiation," Proceedings of First CEAS/AIAA Aeroacoustics Conference, Munich, Germany, pp. 481-489.
10. Tam, C.K.W., Webb, J.C., and Dong, T.Z., 1993, "A Study of the Short Wave Components in Computational Acoustics," *Journal of Computational Acoustics*, Vol. 1, pp. 1-30.
11. Hu, F.Q., Hussaini, M.Y., and Manthey, J., 1996, "Low-dissipation and Low-dispersion Runge-Kutta Schemes for Computational Acoustics," *Journal of Computational Physics*, Vol. 124, pp. 177-191.
12. Tam, C.K.W., and Dong, Z., 1995 "Radiation and Outflow Boundary Conditions for Direct Computation of Acoustic and Flow Disturbances in a Nonuniform Mean Flow," ICASE/LaRC Workshop on Benchmark Problems in Computational Aeroacoustics, NASA Conference Publication 3300, pp. 45-54.
13. Dong, T.Z., 1996, "A Set of Simple Radiation Boundary Conditions for Acoustic Computations in Non-Uniform Mean Flows," Paper 96-0274, 34th AIAA Aerospace Sciences Meeting, Reno, NV.
14. Tam, C.K.W., and Dong, Z., 1994 "Wall Boundary Conditions for High-Order Finite Difference Schemes in Computational Aeroacoustics," Paper 94-0457, 32nd AIAA Aerospace Sciences Meeting, Reno, NV.
15. Hirsch, C., 1990, Numerical Computation of Internal and External Flows, Vol. II, Wiley Publishers, W. Sussex, England, pp. 162 and 369.
16. Thompson, K.W., 1987, "Time-dependent Boundary Conditions for Hyperbolic Systems," *Journal Computational Physics*, Vol. 68, pp. 1-24.

Acknowledgment

This work was partially supported by NASA Langley Research Center Grant NAG-1-1653. The technical monitor was Dr. J.L. Thomas.

Tables and Figures

Table 1. Nonreflective characteristic boundary conditions.

		$\vec{U}^i \cdot \vec{n}^i > 0$		$\vec{U}^i \cdot \vec{n}^i < 0$	
$M^i < 1$	$\vec{n}^i < 0$	Γ_1, Γ_2 by forward DRP	Γ_3 set to zero	Γ_1 by forward DRP	Γ_2, Γ_3 set to zero
	$\vec{n}^i > 0$	Γ_2, Γ_3 by backward DRP	Γ_1 set to zero	Γ_3 by backward DRP	Γ_1, Γ_2 set to zero
$M^i > 1$	$\vec{n}^i < 0$	$\Gamma_1, \Gamma_2, \Gamma_3$ by forward DRP		$\Gamma_1, \Gamma_2, \Gamma_3$ set to zero	
	$\vec{n}^i > 0$	$\Gamma_1, \Gamma_2, \Gamma_3$ by backward DRP			

Table 2. Description of computational cases.

Case	$\bar{\varepsilon}, \varepsilon$	$\bar{b}, b$	x_s, y_s	Grid type, size	$\Delta\bar{t}, \Delta t$	Re	Figure
1: linear and nonlinear pulse; no mean flow	0, 1	0, 6Δx	0, 0	H 141x71	0, 3.7E-1	1E1	1
2: pulse reflected from flat plate; no mean flow	0, 1	0, 6Δx	0, 20Δx	H 141x71	0, 3.7E-1	1E1	2, 3
3: pulse reflected from bump on flat plate; no mean flow	0, 1	0, 0.6D	0, 2D	O 65x65	0, 8E-3	1E3	4
4: periodic source in nonuniform potential sink flow	6.128E-2, 1E-3	6Δx, 3Δx	0,0	H 101x101	2E-1, 8E-2	1E1	5, 6

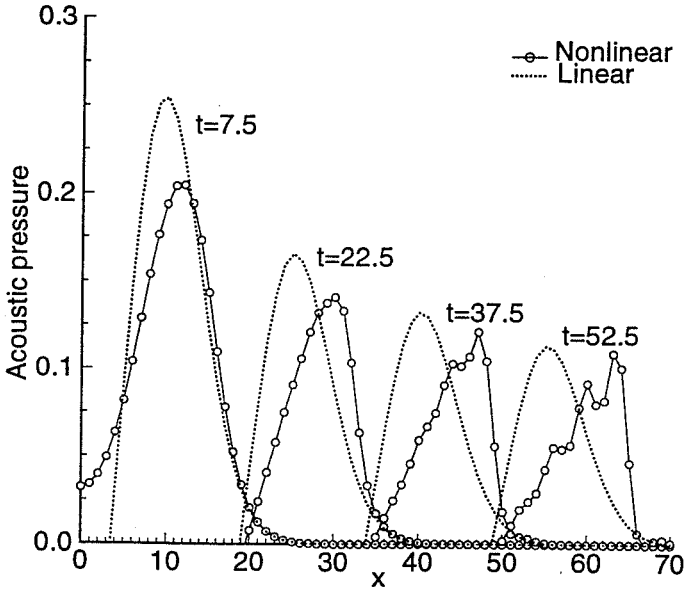

Fig. 1 Linear and nonlinear wave propagation (case 1).
Time history of the positive part of the wave.

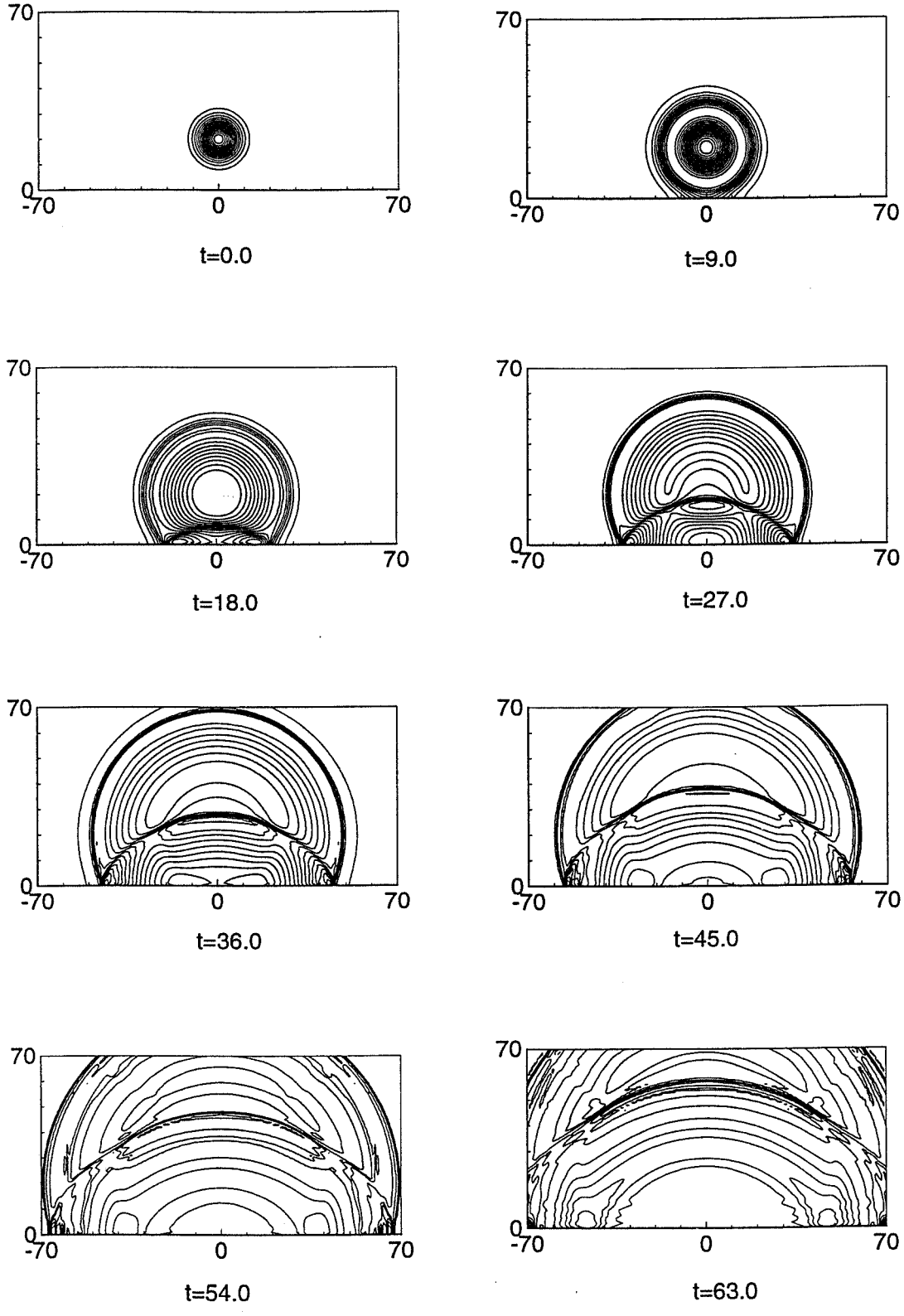

Fig. 2 Reflection of an acoustic pulse from a flat plate (case 2). Acoustic pressure contours computed using characteristic boundary conditions.

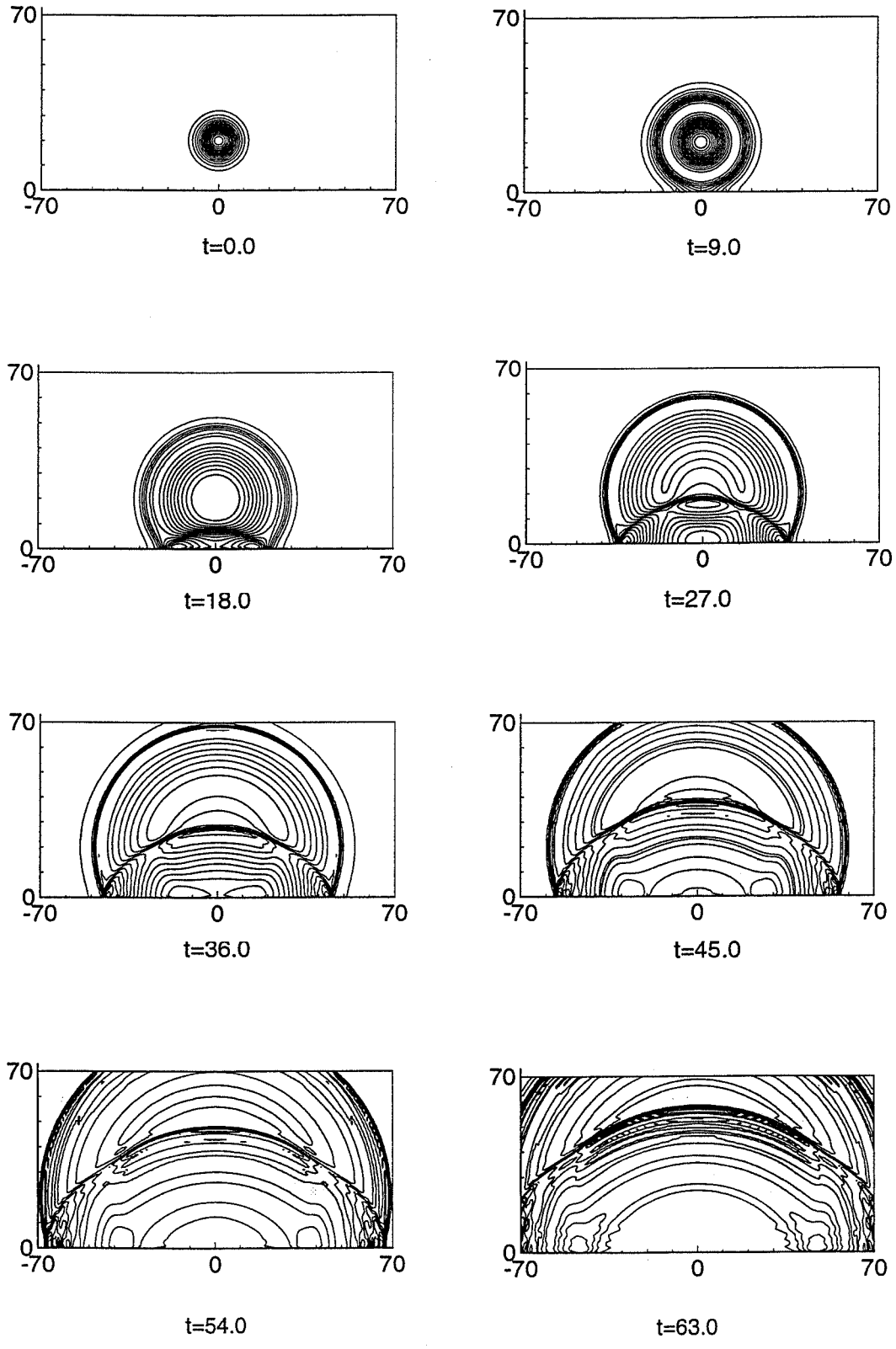

Fig. 3 Reflection of an acoustic pulse from a flat plate (case 2). Acoustic pressure contours computed using radiation boundary conditions.

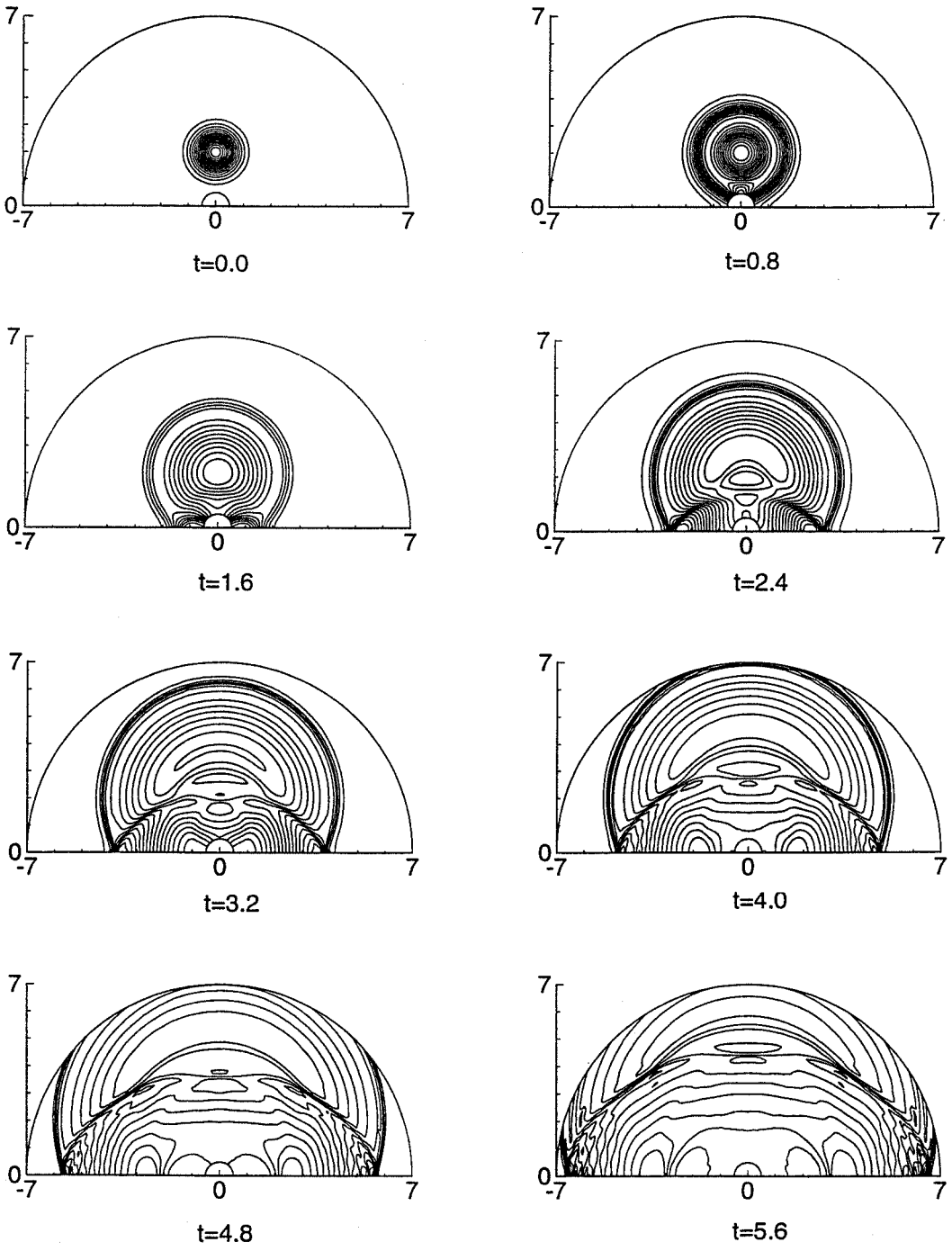

Fig. 4 Reflection of an acoustic pulse from a bump on a flat plate (case 3). Acoustic pressure contours computed using asymptotic boundary conditions

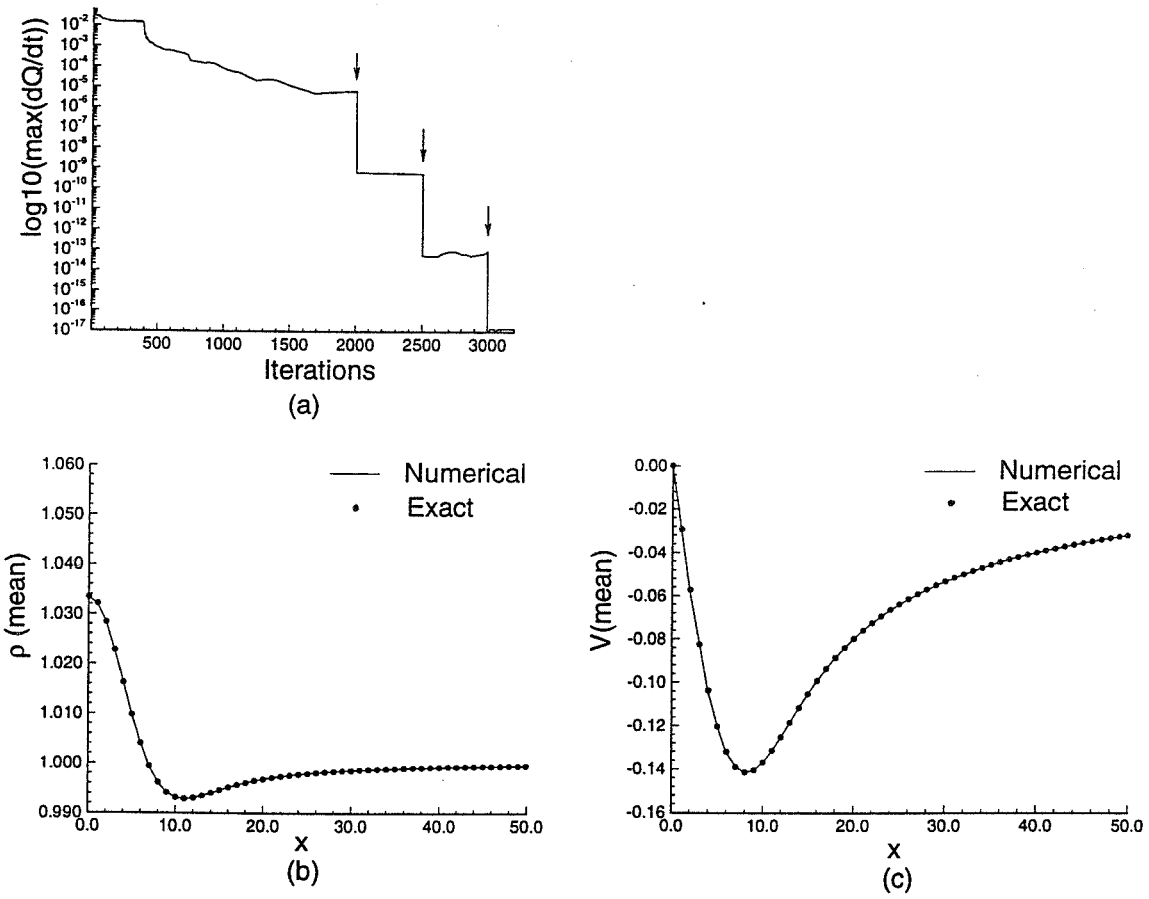

Fig. 5 Nonuniform mean sink flow (case 4) . (a) Residual history, (b) Density distribution and (c) Velocity distribution , along x-axis.

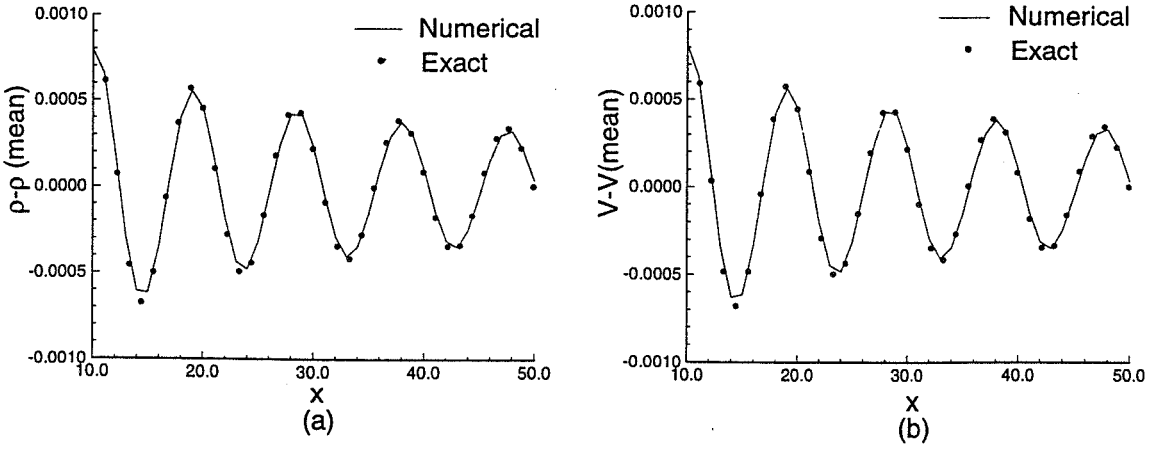

Fig. 6 Nonlinear acoustic wave propagation from a periodic source (case 4). Instantaneous (a) Density distribution, (b) Velocity distribution, along x-axis.

NDB

53-71

Computation of Acoustic Scattering by a Low-Dispersion Scheme

030508
13 p.
28 1562

Oktay Baysal and Dinesh K. Kaushik

Aerospace Engineering Department
Old Dominion University
Norfolk, Virginia 23529-0247 USA

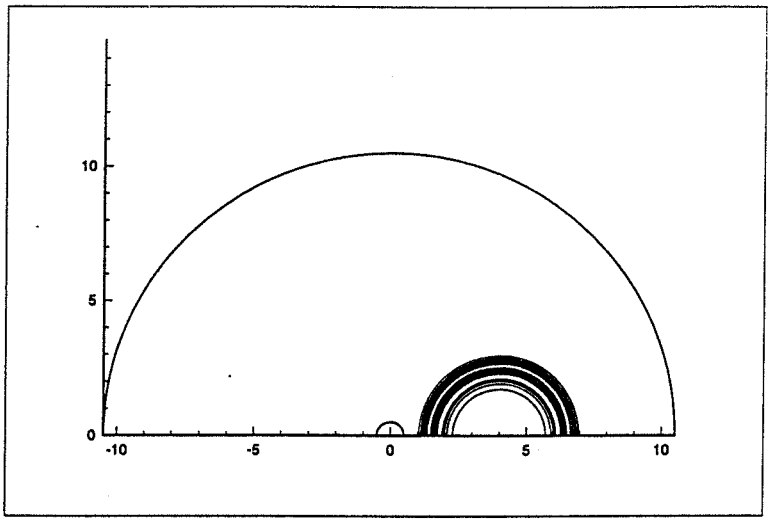

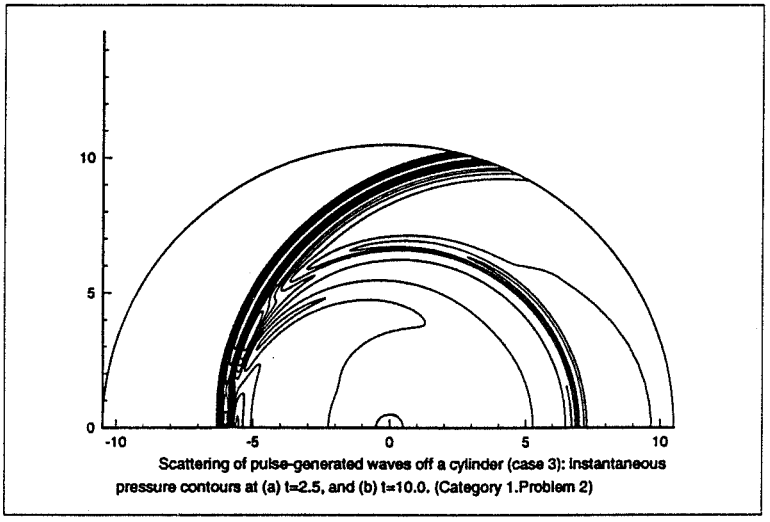

Scattering of pulse-generated waves off a cylinder (case 3): instantaneous pressure contours at (a) t=2.5, and (b) t=10.0. (Category 1.Problem 2)

Proceedings of (NASA-CP March 1997)
Second Computational Aeroacoustics Workshop on Benchmark Problems
Florida State University, Tallahassee, FL / November 4-5, 1996

COMPUTATION OF ACOUSTIC SCATTERING BY A LOW-DISPERSION SCHEME

Oktay Baysal and Dinesh K. Kaushik

Department of Aerospace Engineering
Old Dominion University, Norfolk, Virginia 23529-0247

Physical problem and background

The objective is the evaluation of a proposed computational aeroacoustics (CAA) method in simulating an acoustic scattering problem. An example may be the sound field generated by a propeller scattered off by the fuselage of an aircraft. The pressure loading on the fuselage would be an input to the interior noise problem. To idealize the problem, the fuselage is assumed to be a circular cylinder and the noise generation by the propeller is represented by a line source.

A typical CFD algorithm may not be adequate for this aeroacoustics problem: amplitudes are an order of magnitude ϑ smaller yet frequencies are ϑ larger than the flow variations generating the sound. For instance, an $\vartheta(2)$ CFD method was previously used for a nonlinear wave propagation problem in unsteady, nonuniform mean flow (Baysal et al., 1994). It was observed that a direct simulation of acoustic waves using a higher-order CFD would become prohibitively expensive, due to the required excessive number of grid points per wavelength (PPM). Also, CAA would need minimal dispersion and dissipation, which would preclude a typical $\vartheta(2)$ CFD method from a long-term wave propagation simulation. Furthermore, a consistent, stable, convergent, high-order scheme is not necessarily dispersion-relation preserving, i.e. no guarantee for a quality numerical solution. Therefore, a baseline $\vartheta(4)$ dispersion-relation-preserving (DRP) method (Tam and Webb, 1993) was investigated (Vanel and Baysal, 1997) for a variety of wave propagation problems, such as, single-, simultaneous-, and successive-acoustic-pulses. Then, a number of algorithmic extensions were performed (Kaushik and Baysal, 1996), when the following were studied: viscous effects by solving the linearized Navier-Stokes equations, low-storage and low-CPU time integration by an optimized Runge-Kutta scheme, generalized curvilinear coordinates for curved boundaries, higher-order accuracy by comparing $\vartheta(4)$ DRP vs. $\vartheta(6)$ DRP, and choice of boundary conditions and differencing stencils. The scheme is now being investigated for nonlinear wave propagation in nonuniform flow (Baysal et al., 1997).

Mathematical approach

The linearized, two-dimensional, compressible, Euler equations were considered in generalized curvilinear coordinates

$$(1) \qquad \frac{\partial \hat{U}}{\partial t} = -R(\hat{U}) + S \ , \qquad \text{where} \quad R(\hat{U}) = \frac{\partial \hat{E}}{\partial \xi} + \frac{\partial \hat{F}}{\partial \eta} \ .$$

The primitive variables, $\hat{U}$, and the transformed fluxes, $\hat{E}$ and $\hat{F}$, are,

$$(2) \qquad \hat{U} = \frac{1}{J}[\rho \quad u \quad v \quad p]^T \ , \qquad \hat{E} = \frac{1}{J}[\xi_x E + \xi_y F], \qquad \hat{F} = \frac{1}{J}[\eta_x E + \eta_y F] \ .$$

and the physical fluxes and the source vector are,

$$(3) \qquad E=\begin{bmatrix} u+M_0\rho \\ M_0u+p \\ M_0v \\ M_0p+u \end{bmatrix}, \quad F=\begin{bmatrix} v \\ 0 \\ p \\ v \end{bmatrix}, \quad S=\begin{bmatrix} 0 \\ 0 \\ 0 \\ S_4 \end{bmatrix}.$$

The perturbed values of density (ρ), pressure (p), and velocity (u,v) are denoted without a subscript, but those of the mean flow are demarcated using the subscript 0. These variables were normalized using the cylinder diameter (D) for length, speed of sound (a_0) for velocity, D/a_0 for time, ρ_0 for density, and $\rho_0(a_0)^2$ for pressure.

Dispersion relation of a proposed numerical scheme should match closely that of eq. (1) for large range of resolution; i.e. $\overline{\alpha}$ and $\overline{\omega}$ be close approximations to α and ω. Assuming $\overline{\alpha}\Delta x$ was a periodic (2π) function of $\alpha\Delta x$ with, Fourier-Laplace transforms rendered,

$$(4) \qquad \overline{\alpha}=\frac{-i}{\Delta x}\sum_{j=-L}^{M} a_j e^{i\cdot\alpha j\Delta x} \quad \text{and} \quad \overline{\omega}=\frac{i\left(e^{-i\cdot\omega\Delta t}-1\right)}{\Delta t\sum_{j=0}^{N} b_j e^{i\cdot j\omega\Delta t}}.$$

Finite difference coefficients were obtained from Taylor series expansions as one-parameter family, and the remaining coefficient from an error minimization, where the integration limit ε depended on the shortest wavelength to be simulated:

$$(5) \qquad min\ E_I = min\int_{-\varepsilon}^{\varepsilon}\left|\alpha\Delta x-\overline{\alpha}\Delta x\right|^2 d(\alpha\Delta x) \quad \text{where} \quad |\alpha\Delta x|\prec\varepsilon \quad \text{and} \quad \varepsilon=\begin{Bmatrix}\pi/2\\ 1.1\end{Bmatrix} \text{ for } \begin{Bmatrix}4.5\Delta x\\ 7\Delta x\end{Bmatrix}.$$

The time integration of eq. (1) was performed in two different ways. In the first approach, a four-point finite difference, which in a standard sense could be up to third-order accurate, was derived from the Taylor series as a one-parameter family. The remaining coefficient (b_j) was determined, as in the spatial coefficients, by minimizing the discrepancy between the effective and the exact dispersion relations. After discretizing all the terms in eqs. (1)-(3), the resulting $\vartheta(\Delta t^2,\Delta x^{N+M-2})$ DRP scheme was as follows:

$$(6) \qquad \hat{U}_{\ell,m}^{n+1}=\hat{U}_{\ell,m}^{n}+\Delta t\sum_{j=0}^{3} b_j R_{\ell,m}^{n-j} \quad \text{where} \quad R_{\ell,m}^{n}=\frac{-1}{\Delta\xi}\sum_{j=-N}^{M} a_j \hat{E}_{\ell+j,m}^{n}-\frac{1}{\Delta\eta}\sum_{j=-N}^{M} a_j \hat{F}_{\ell,m+j}^{n}.$$

In eq. (6), ℓ and m are the spatial indices and n indicates the time level. For N=M, difference is central, for N=0, it is fully forward, and for M=0, it is fully backward. All the interior cells were computed using central differences with N=M=3. However, since these high-order stencils require multiple layers of boundary cells, all combinations between a central and a fully-one-sided difference need also be derived. Only then, it would be possible to always utilize the information from the nearest possible points for better accuracy. In the present computations a fourth-order scheme was used, requiring 7-point stencil: N takes values from 6 to 0, M takes values from 0 to 6, and N+M=6.

The numerically stable maximum time step Δt was calculated from the Courant-Friedrichs-Lewy relation. For example, for the fourth-order scheme in Cartesian coordinates, the stable CFL number was found to be 0.4. However, after analyzing the numerical damping of the time integration scheme, the CFL value was set to the more stringent value of 0.19. Since, however, time integration with DRP would require the storage of four time levels, a lower storage alternative, the low-dissipation and low-dispersion

five-stage Runge-Kutta scheme (Hu et al., 1996) was adapted and implemented. The resulting scheme had the spatial integration identical to eq. (6), but the time integration was replaced by the following:

$$(7) \qquad \hat{U}^{(0)} = \hat{U}^n, \quad \hat{U}^{(i)} = \hat{U}^{(0)} - \beta_i \Delta t R^{(i-1)}, \quad \hat{U}^{n+1} = \hat{U}^{(p)}, \qquad i = 1,2,..,p \quad .$$

The indices n, p and i indicate the time level, and the order and the stage of the Runge-Kutta method, respectively. As for the coefficients, β_1=0 and the other coefficients β_i were determined from

$$(8) \qquad c_i = \prod_{k=2}^{i} \beta_{p-k+2} \quad , \qquad i = 2,\ldots, p \quad .$$

The coefficients c_i were computed by considering the amplification factor of the Runge-Kutta scheme, then minimizing the dispersion-relation error. The time steps were determined from the stability as well as the accuracy limits. In the present study, a five-stage Runge-Kutta (p =5) was used, which required two levels of storage and it was at least second-order accurate. When it was used with the present 7-point spatial stencil to solve the scalar linear wave equation, the CFL limit from the stability was found to be 3.05, but it was only 1.16 from the accuracy limit. Since, however, this still was larger than the CFL limit of the DRP time integration, this method was also more efficient in processing time.

Usually low-order schemes are used in resolving the highly nonlinear flow or acoustic phenomena. Even with second-order schemes, it is common to have limiters or artificial damping mechanisms, either implicit in the scheme or explicitly added. Since simulating low-amplitude acoustic waves for a long time and for many wavelengths of travel is the objective in CAA, devising such artificial damping mechanisms requires extreme care. For example, constant damping over all wave numbers need to be avoided. Tam et al. (1993) suggested terms, which have small damping over the long wave range but significant damping in the short wave range. The present central-difference scheme includes similar terms with a user specified artificial Reynolds number, to overcome the expected spurious oscillations:

$$(9) \qquad D^n_{\ell,m} = \frac{1}{\mathrm{Re}_D} \sum_{j=-N}^{N} c_j \left[\frac{1}{\Delta\xi^2}\hat{U}^n_{\ell+j,m} + \frac{1}{\Delta\eta^2}\hat{U}^n_{\ell,m+j}\right], \quad \text{where} \quad \mathrm{Re}_D = \frac{\rho_0 a_0 D}{\mu_a} \quad .$$

The boundaries should be transparent to the acoustic disturbances reaching them to avoid any degradation of the numerical solution. From the asymptotic solutions of the finite difference form of the Euler equations, a set of radiation boundary conditions, were derived and implemented. Therefore, following Tam and Webb (1993) and from the asymptotic solutions of the finite difference form of eq. (1), a set of *radiation* boundary conditions were derived,

$$(10) \qquad \frac{\partial \hat{U}}{\partial t} + A\frac{\partial \hat{U}}{\partial \xi} + B\frac{\partial \hat{U}}{\partial \eta} + C\hat{U} = 0, \text{ where}$$

$$(11) \qquad A \equiv V\frac{x\xi_x + y\xi_y}{r}, \quad B \equiv V\frac{x\eta_x + y\eta_y}{r}, \quad C \equiv \frac{V}{2r} \text{ and } r = \frac{1}{D}\sqrt{x^2+y^2}, \quad V = \frac{x}{r}M_0 + \sqrt{1-(M_0\frac{y}{r})^2} \quad .$$

For an inviscid solid wall (w) or a symmetry plane, the impermeability condition dictates that the normal contravariant velocity be zero at all times:

$$(12) \qquad \hat{v} = \eta_x u + \eta_y v = 0 \quad .$$

When this equation was constructed from the η- and ξ-momentum equations, after multiplying them by the appropriate metrics and adding, the wall value of pressure at the ghost point (subscript -1) was obtained,

$$p_{\ell,-1}=\frac{-\Delta\eta}{a_{\ell,-1}(\eta_x^2+\eta_y^2)_{\ell,w}}\{\frac{M_0}{\Delta\xi}[(\eta_x\xi_x)_{\ell,w}\sum_{j=-N}^{M}a_j u_{\ell+j,w}+(\eta_y\xi_x)_{\ell,w}\sum_{j=-N}^{M}a_j v_{\ell+j,w}$$

$$+(\eta_x)_{\ell,w}^2\sum_{j=w}^{N+M}a_j u_{\ell,j}]+\frac{(\eta_x\xi_x+\eta_y\xi_y)_{\ell,w}}{\Delta\xi}\sum_{j=-3}^{3}a_j p_{\ell+j,w}\}-\frac{1}{a_{\ell,-1}}[\sum_{j=w}^{N+M}a_j p_{\ell,j}] \quad (13)$$

The coefficients for all the boundary conditions (Tam and Dong, 1994) were derived by an analogous method to that of the boundary region cells. At the corners, two separate ghost points were used, one for each boundary, hence both boundaries' conditions were satisfied.

Results

The present method and its boundary conditions were evaluated by considering a number of reflection or scattering cases (table 1), all in quiescent medium, i.e. $M_0=0$. The acoustic waves were generated either by an initial acoustic pulse introduced to the field at $t=0$ by setting $S=u=v=0$, and

$$p=\hat{p}\exp\{-\ln 2\,[\frac{(x-x_s)^2+(y-y_s)^2}{b^2}]\} \quad \text{(Category 1\_Problem 2),} \quad (14)$$

or by a periodic source with $\omega=8\pi$,

$$S_4=\hat{s}\exp\{-\ln 2\,[\frac{(x-x_s)^2+(y-y_s)^2}{b^2}]\}\sin(\omega t) \quad \text{(Category 1\_Problem 1).} \quad (15)$$

Table 1. Description of computational cases

Case	Equation	$\hat{p}$ or $\hat{s}$	b	x_S, y_S	Grid	Δt	Figure
1	14	1.0	3D	4D, 0	H 251x101	1.00E-2	1
2	14	1.0	0.2D	4D, 0	O 401x181	5.00E-3	-
3*	14	1.0	0.2D	4D, 0	O 801x181	5.00E-3	3, 4
4	15	0.01	3D	0, 2D	H 251x101	1.00E-2	5
5	15	1.0	3D	0, 2D	H 251x101	1.00E-2	6
6	15	1.0	0.2D	4D, 0	O 801x181	2.5E-3	7
7**	15	1.0	0.2D	4D, 0	O 361x321	2.50E-3 1.25E-3	8, 9

*Category 1_Problem 2 **Category 1_Problem 1

Gaussian pulse: an initial-value problem

In case 1, a coarse H-grid was generated, where the ξ-lines were along the cylinder and the centerline, and the η-lines were perpendicular to the centerline. The transformed computational domain was rectangular with *uniform steps* in each direction and *orthogonal* grid lines, as needed by the DRP scheme. Despite some smearing of the wave front, the initial pulse, its propagation and scattering off the cylinder, were simulated fairly well (fig. 1). However, some oscillations inside the domain and spurious reflections off the boundaries started to emerge.

Then, the grid topology was changed to an O-grid with a radius of 10.5D (cases 2 and 3). The grid had ξ-lines as concentric circles, with the first and last circles being respectively the cylinder and the outer boundary, and the η-lines emanated radially from the cylinder to the outer boundary (fig. 2). The time step Δt = 5.0E-3 was less than one-half of the accuracy limit for eq. (7) as applied to a linear wave equation, but about five times that needed for eq. (6). Although, the results with the 401 ξ-lines appeared adequate (case 2), doubling these lines rendered a truly symmetric initial pulse (case 3). On an SGI R10K computer in a time-shared mode, case 3 required 24 megabytes of run-time memory and 16 hours of CPU

processing. The unit processing time was computed to be about 0.2 ms/Δt/node. At three locations, given in their cylindrical coordinates, A(5D, $\pi/2$), B(5D, $3\pi/4$), C(5D, π), the pressure history was recorded from $t = 6$ to $t = 10$ at intervals of 0.01 (fig. 3). The computed results matched the analytical solution very well. The peak reached these points at about $t \approx 6.3$, 8.2 and 9.0, respectively, and it appeared slightly attenuating (0.06, 0.052, 0.048, respectively) due to the scattering. The peak-trough pair was followed by another set with lower amplitudes. All the waves were crisply simulated with virtually no numerical reflections from the boundaries (fig. 4). This very feature, i.e. the success of the boundary conditions, appeared to be pivotal for this problem.

Periodic source: a limiting-cycle problem

In the preparatory cases of 4 and 5, the equations were solved on an H-grid conforming to the wall shape: a flat plate in the former (fig. 5), and a circular bump on a flat plate in the latter case (fig. 6). The objective was to check the implementation of the boundary conditions and the suitability of the grid. The interference patterns from the cascades of incident and reflected waves reached a periodic state (limiting cycle), after some transient time, as could also be observed by the wall pressure (figs. 5 and 6). Note that the source amplitude was 1% in case 4.

In cases 6 and 7, the scattering off a cylinder was simulated on O-grids and the directivity,

$$(16) \qquad D(\theta) = \lim_{r \to \infty} \left\{ r \overline{p^2} \right\} \equiv \frac{R}{n_2 - n_1} \sum_{n_1}^{n_2} p_n^2 \quad ,$$

was computed at $r=R$ and from time step n_1 to n_2. In case 6, the solution was obtained on a 801x181 O-grid with 10.5D radius. This resulted in 20 PPW radially, and PPW circumferentially were: 28.6 on cylinder, 2.86 at $r=5.0$, and 1.36 at the outer boundary. However, from eq. (5), the theory required 4.5 PPW, which was satisfied for points with $r < 3.18$. Consequently, despite the periodic response attained, e.g. on the cylinder (fig 7), neither the computed directivity pattern nor its amplitudes at R=10.5D were satisfactory.

Hence, another O-grid was generated with 361x321 points and a radius of 8.5D (case 7). This resulted in 10 PPW radially, and PPW circumferentially were: 57.3 on cylinder, 5.73 at $r=5.0$, and 3.37 at the outer boundary. The theoretically required 4.5 PPW was satisfied for points with $r < 6.36$. (Practice may prove the safer requirement to be 8 PPW, which was satisfied for points with $r < 3.58$.) Initially, Δt was 2.5E-3, but after t=15, it was reduced to 1.25E-3, which was one-fourth of the accuracy limit for eq. (7) as applied to a linear wave equation, but 2.5 times that needed for eq. (6). At $r = R = 5$ and θ from 0 to $\pi/2$, the periodic response was detected after 100 periods of source excitation, then the results were recorded at $r = R = 5$ and θ from 0 to π at 0.5-deg intervals. The computed directivity is presented in fig. 8. Although, the directivity had not yet attained the limiting cycle values at t=26.25, the number of peaks matched analytical values well. Since the results were relatively better for $\theta < \pi/2$, and for $\theta > \pi/2$, they improved with the elapsed time, it was deemed that all the transients had not yet left the domain. Also due to the marginal PPW circumferentially at $r=5$ and the uncertainty about the sufficient artificial viscosity to be used (Re in eq. (9) was set to 1.0E4), some oscillations were detected. This computed scattering pattern is also depicted via its pressure contours at two instants (fig. 9). Finally, on an SGI R10K computer in a time-shared mode, case 7 required 19.2 megabytes of run-time memory and 100 hours of CPU processing. Conceivably, the elapsed time for the scattering shown should have been doubled, which, naturally, would have required twice as much computing time.

Conclusions

By and large, the present simulations of the propagation of acoustic waves, their reflections and scattering, in particular, the initial-value problem with the acoustic pulse, were successful. Two necessary building blocks to success, once a suitable CAA scheme was selected, were the correct boundary conditions, and an

adequate and efficient grid. Notwithstanding the imperfectly orthogonal grids and the required transformation metrics, employing the body-fitted coordinates allowed a straight forward implementation of the boundary conditions. The role of the grid became more accentuated in the periodic source case. The spread of the source (b in eq. (15)) and the intervals that the directivity was requested (1-deg) proved narrow enough to necessitate too fine a grid resolution, which superseded the benefits of a low PPW scheme. A better deployment of the grid points, such as, some sort of domain decomposition, could reduce the required computational resources. Also, since it took longer for the periodic behavior to be established at $\theta=\pi$, it would have been less resource taxing to request the data up to, say, $\theta=3\pi/4$. Further, the definition of directivity included the $r \to \infty$, leading one to place the outer boundary as far away as possible; however, the benchmark analytical solution was integrated virtually at any $r=R$ value. Finally, a parametric study of the required amount of artificial dissipation proved to be another prerequisite.

References

Baysal, O., Yen, G.W., and Fouladi, K., 1994, "Navier-Stokes Computations of Cavity Aeroacoustics With Suppression Devices," *Journal of Vibration and Acoustics*, Vol. 116, No. 1, pp. 105-112.

Baysal, O., Kaushik, D.K., and Idres, M., 1997, "Low Dispersion Scheme for Nonlinear Acoustic Waves in Nonuniform Flow," AIAA Paper 97-1582, *Proceedings of Third CEAS/AIAA Aeroacoustics Conference*, Atlanta, GA.

Hu, F.Q., Hussaini, M.Y., and Manthey, J., 1996, "Low-dissipation and Low-dispersion Runge-Kutta Schemes for Computational Acoustics," *Journal of Computational Physics*, Vol. 124, pp. 177-191.

Kaushik, D.K., and Baysal, O., 1996, "Algorithmic Extensions of Low-Dispersion Scheme and Modeling Effects for Acoustic Wave Simulation," *Proceedings The ASME Fluids Engineering Division Summer Meeting*, FED-Vol. 238, San Diego, CA, pp. 503-510.

Tam, C.K.W., Webb, J.C., and Dong, T.Z., 1993, "A Study of the Short Wave Components in Computational Acoustics," *Journal of Computational Acoustics*, Vol. 1, pp. 1-30.

Tam, C.K.W., and Dong, Z., 1995 "Radiation and Outflow Boundary Conditions for Direct Computation of Acoustic and Flow Disturbances in a Nonuniform Mean Flow," *ICASE/LaRC Workshop on Benchmark Problems in Computational Aeroacoustics*, NASA Conference Publication 3300, pp. 45-54.

Tam, C.K.W., and Dong, Z., 1994 "Wall Boundary Conditions for High-Order Finite Difference Schemes in Computational Aeroacoustics," AIAA Paper 94-0457, 32nd Aerospace Sciences Meeting, Reno, NV.

Tam, C.K. W., and Webb, J. C., 1993, "Dispersion-Relation-Preserving Finite Difference Schemes for Computational Acoustics," *Journal of Computational Physics*, Vol. 107, pp. 262-283.

Vanel, F. O., and Baysal, O., 1997, "Investigation of Dispersion-Relation-Preserving Scheme and Spectral Analysis Methods for Acoustic Waves," *Journal of Vibration and Acoustics*, Vol. 119, No. 2.

Acknowledgments

This work was supported by NASA Langley Research Center Grant NAG-1-1653. The technical monitor was J.L. Thomas. Authors thank D.E. Keyes for the helpful discussions.

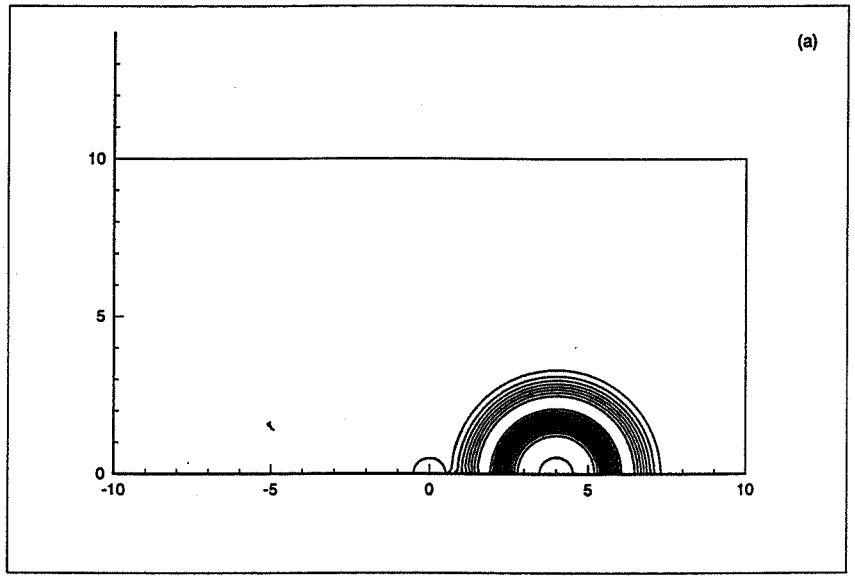

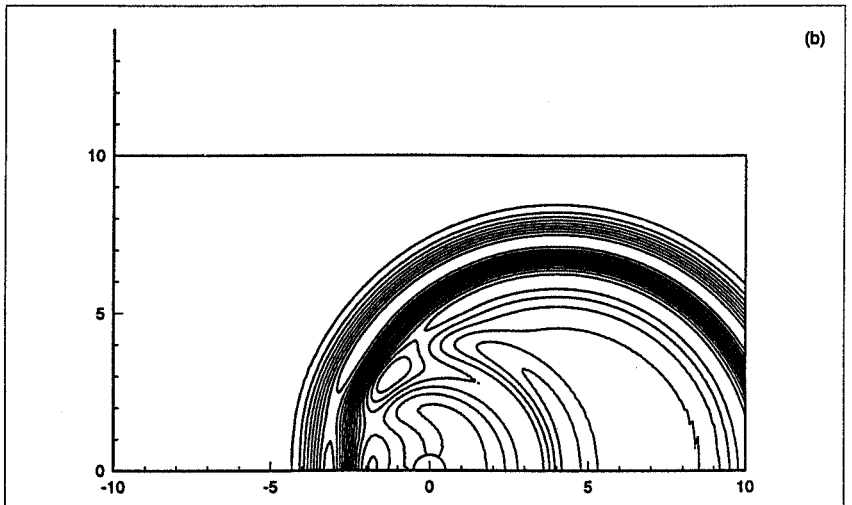

Fig. 1 Scattering of pulse-generated waves off a cylinder (case1): instantaneous pressure contours at (a) t=2.0, and (b) t=7.0.

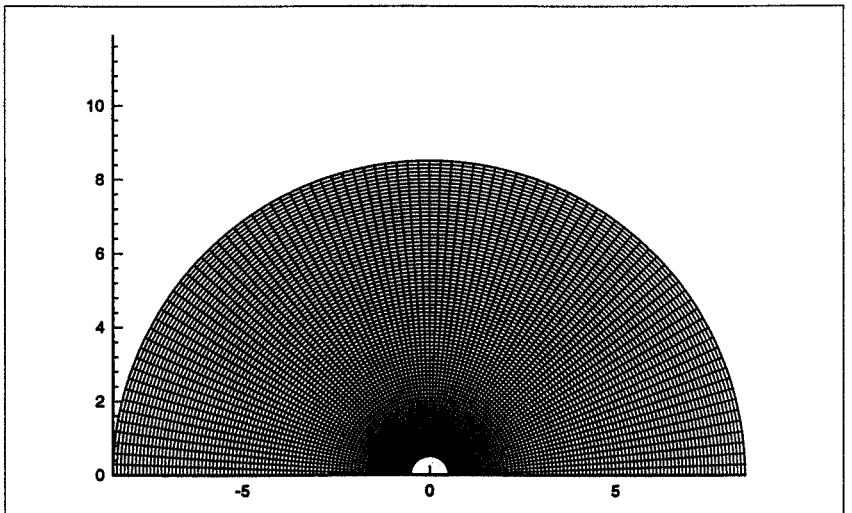

Fig. 2 Representative O-grid conforming to the surface of a circular cylinder.

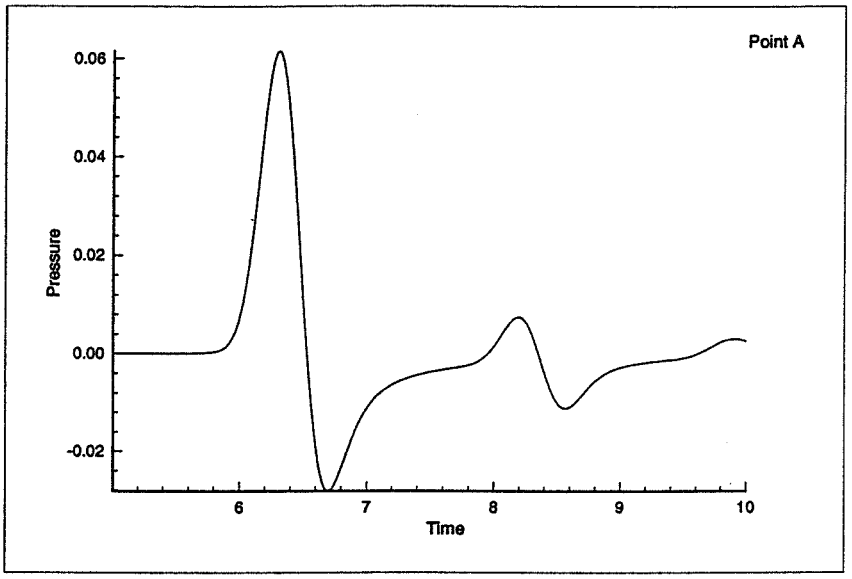

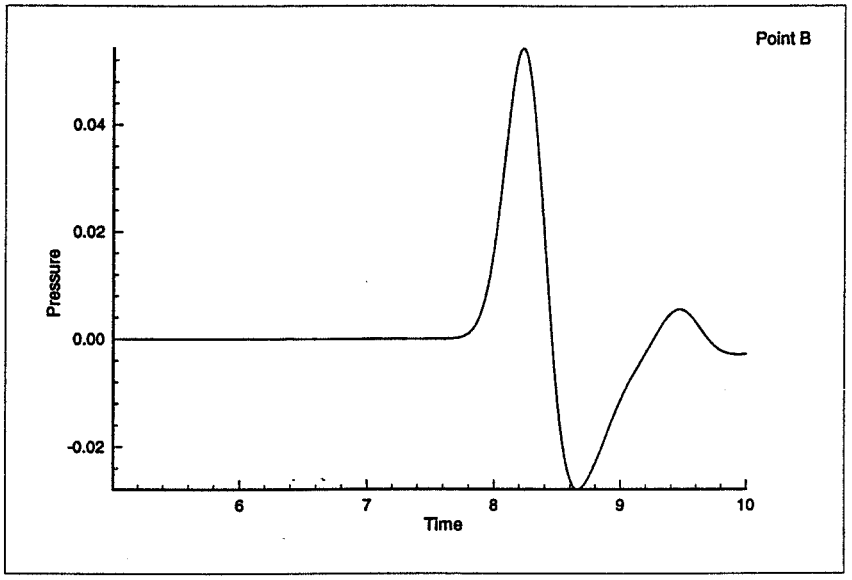

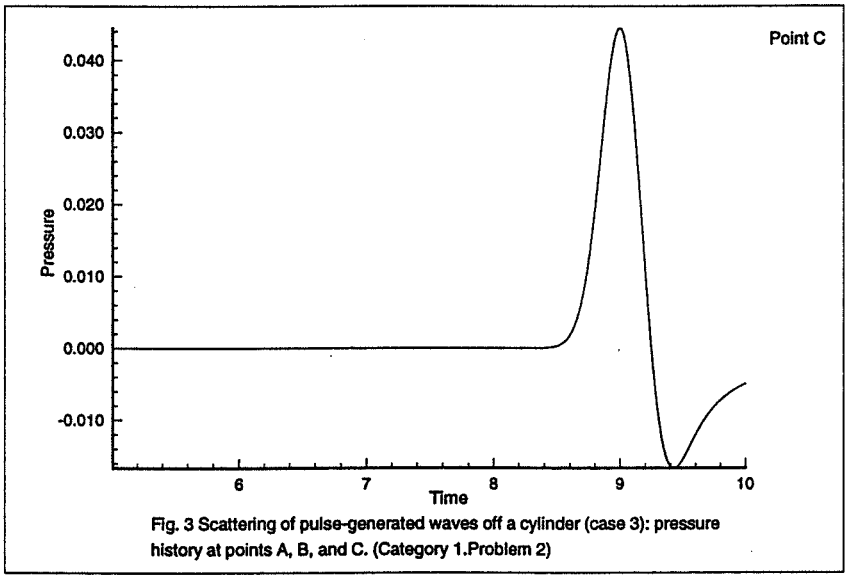

Fig. 3 Scattering of pulse-generated waves off a cylinder (case 3): pressure history at points A, B, and C. (Category 1.Problem 2)

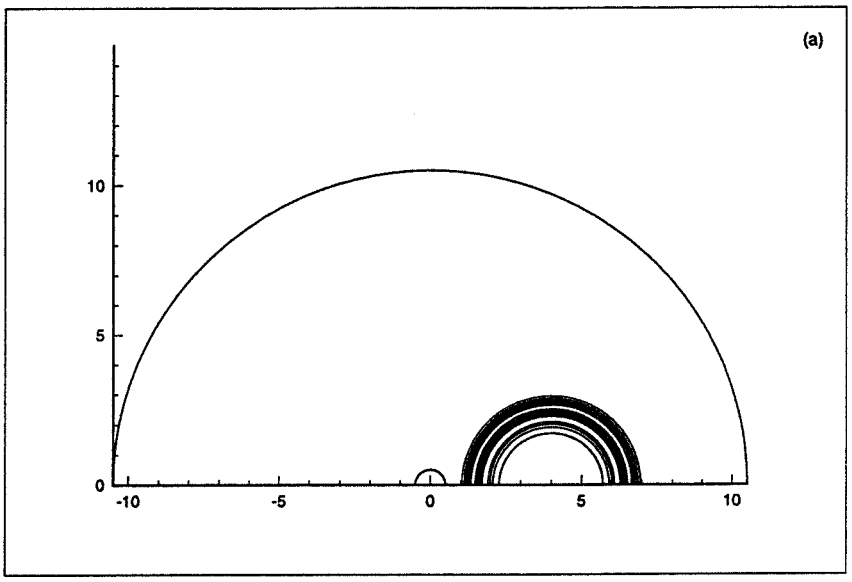

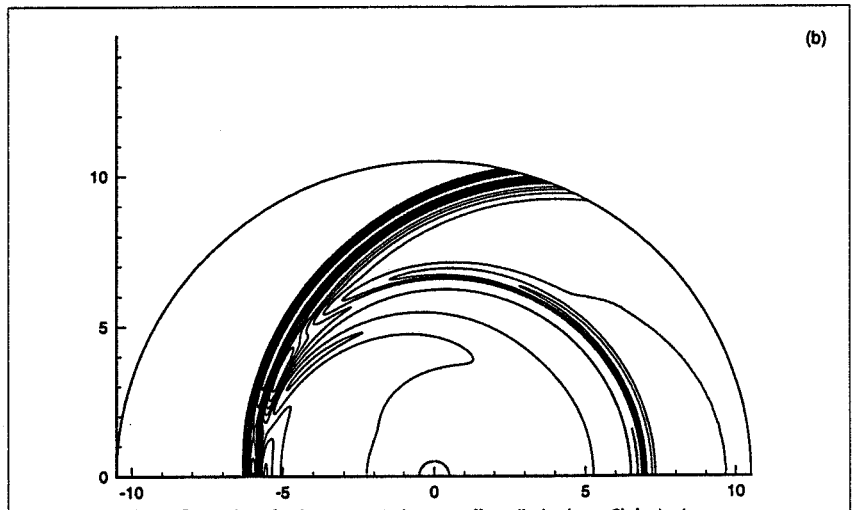

Fig. 4 Scattering of pulse-generated waves off a cylinder (case 3): instantaneous pressure contours at (a) t=2.5, and (b) t=10.0. (Category 1.Problem 2)

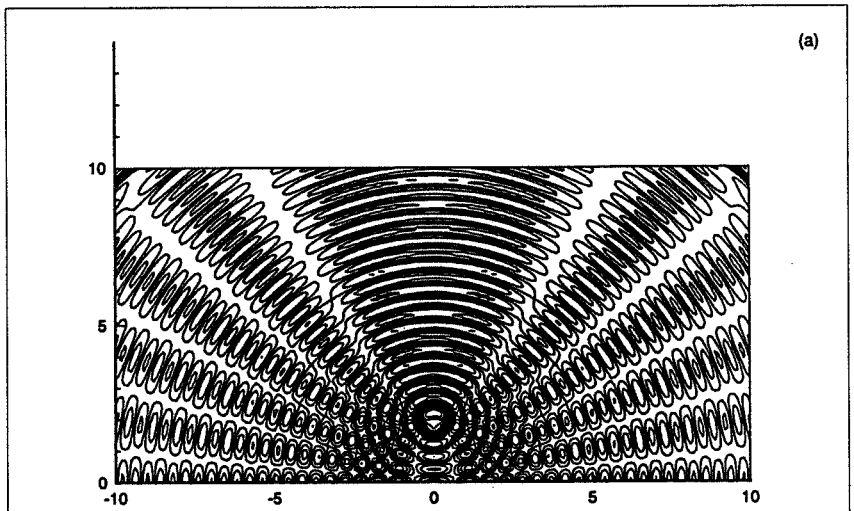

Fig. 5 Interference pattern of a periodic source reflected from a flat plate (case 4). (a) pressure contours, and (b) wall pressure values.

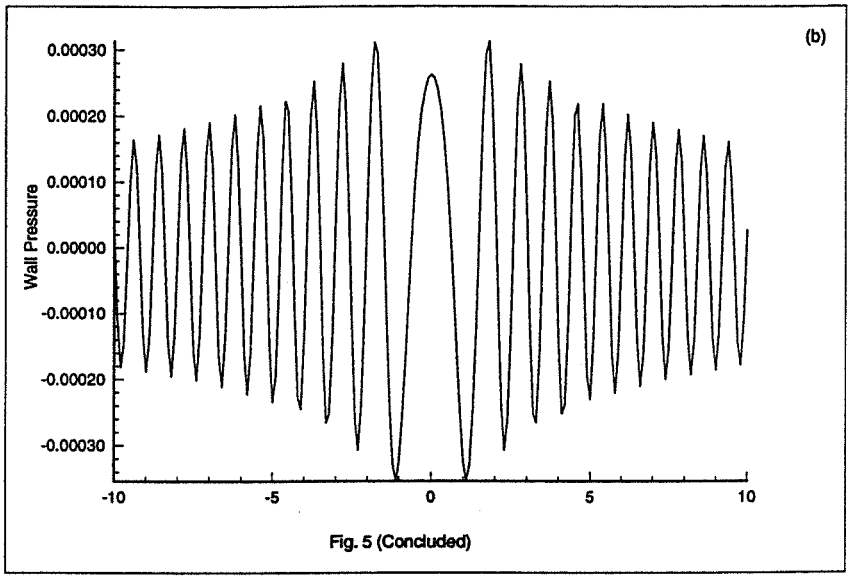

Fig. 5 (Concluded)

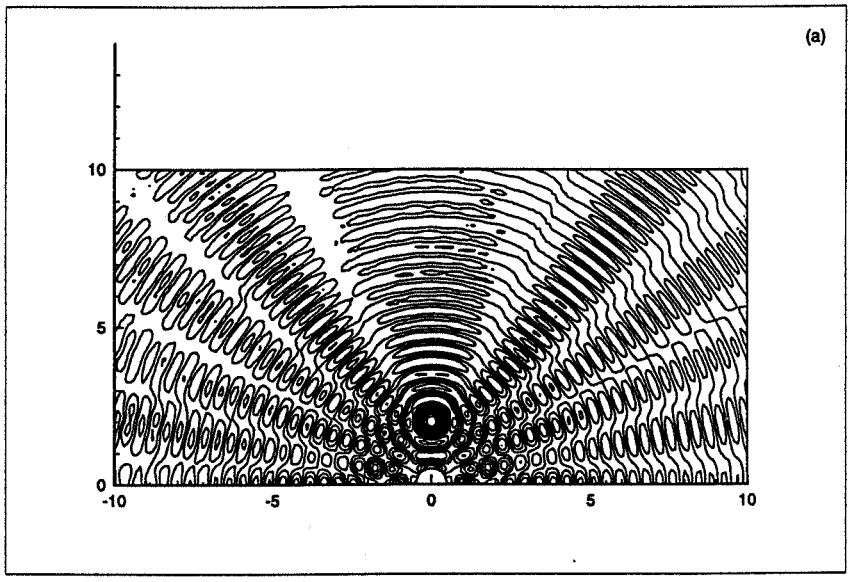

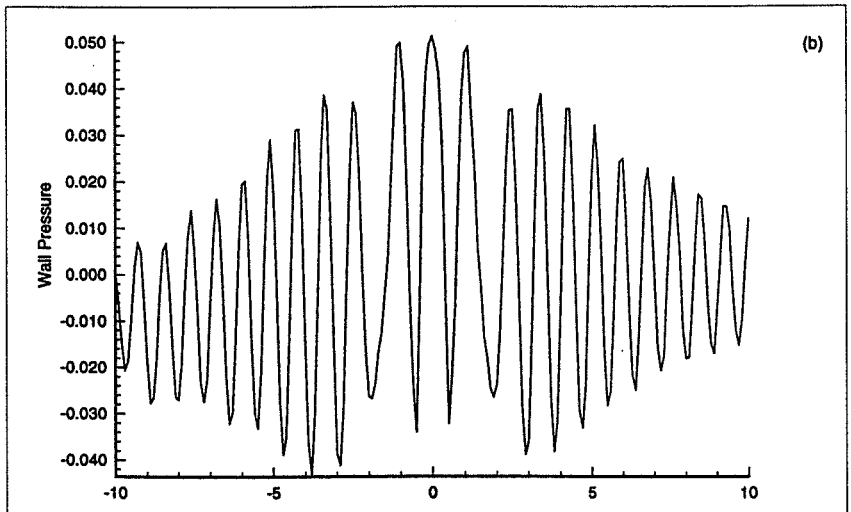

Fig. 6 Interference pattern of aperiodic source reflected from a bump on a flat plate (case 5). (a) pressure contours, and (b) wall pressure values.

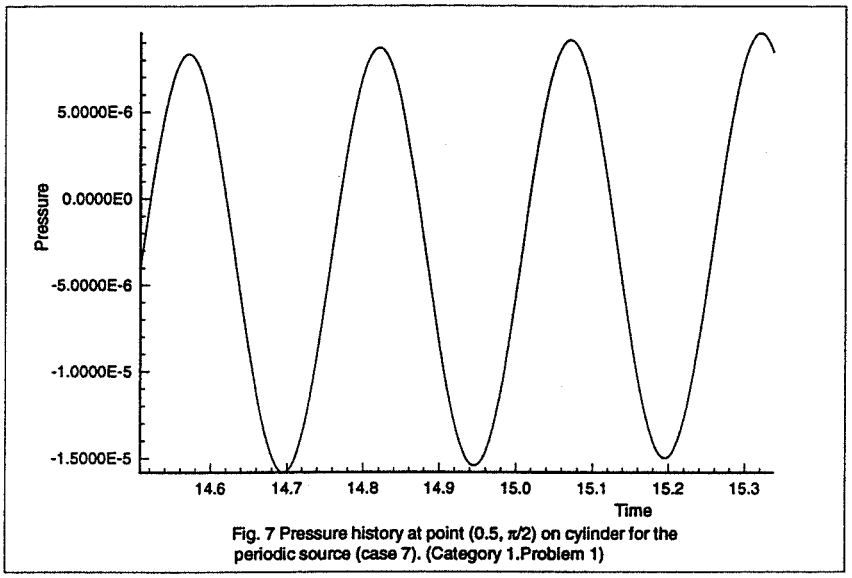

Fig. 7 Pressure history at point (0.5, π/2) on cylinder for the periodic source (case 7). (Category 1.Problem 1)

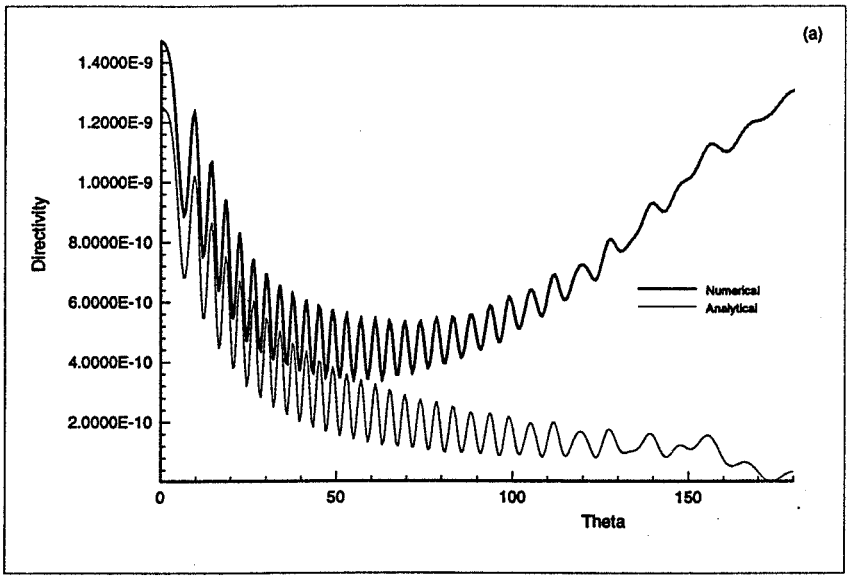

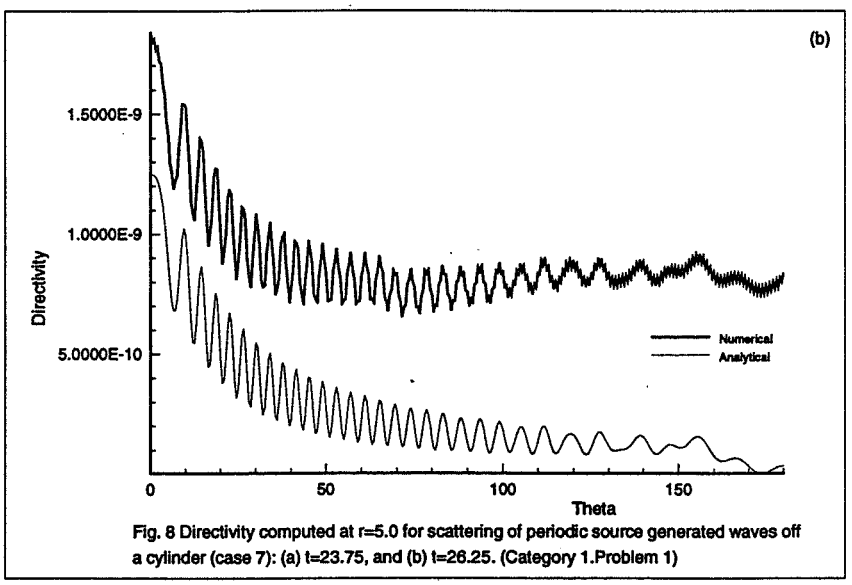

Fig. 8 Directivity computed at r=5.0 for scattering of periodic source generated waves off a cylinder (case 7): (a) t=23.75, and (b) t=26.25. (Category 1.Problem 1)

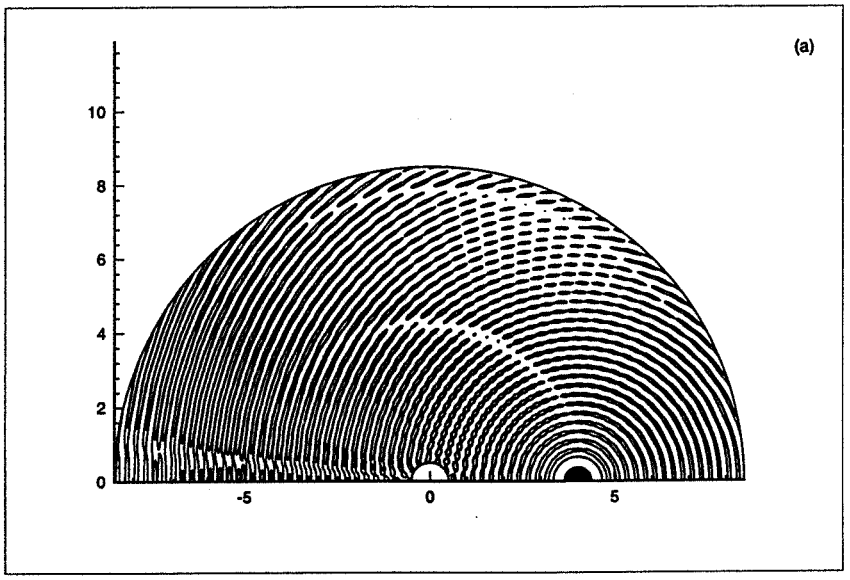

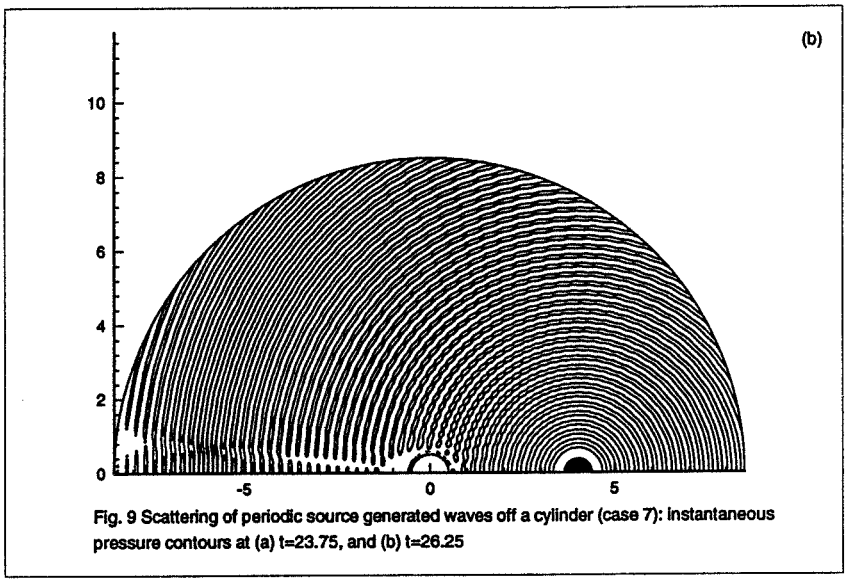

Fig. 9 Scattering of periodic source generated waves off a cylinder (case 7): Instantaneous pressure contours at (a) t=23.75, and (b) t=26.25

Investigation of Dispersion-Relation-Preserving Scheme and Spectral Analysis Methods for Acoustic Waves

Florence O. Vanel
Former Graduate Student.

Oktay Baysal
Eminent Professor.
Fellow ASME

Aerospace Engineering Department,
Old Dominion University,
Norfolk, VA 23529-0247

Important characteristics of acoustic wave propagation are encoded in their dispersion relations. Hence, a computational algorithm, which attempts to preserve these relations, was investigated. Considering the linearized, 2-D Euler equations, simulations were performed to validate this scheme and its boundary conditions. The results were found to agree favorably with the exact solutions. The boundary conditions were transparent to the outgoing waves, except when the disturbance source was close to a corner boundary. The time-domain data generated by such computations were often intractable until their spectra was analyzed. For this purpose, the relative merits of three spectral analysis methods were considered. For simple, periodic waves with steep-sloped spectra, the periodogram method produced better estimates than the Blackman-Tukey method, and the Hanning window was more effective when used with the former. For chaotic waves, however, the weighted-overlapped-segment-averaging and Blackman-Tukey methods were better than the periodogram method. Therefore, it was observed that the spectral representation of time-domain data was significantly dependent on the particular method employed.

1 Introduction

Computational aeroacoustics (CAA) may be defined as the employment of numerical techniques for the direct calculation of all aspects of aerodynamic sound generation and propagation starting from the time-dependent governing equations (Hardin, 1993). Most computational fluid dynamics (CFD) schemes, however, are not adequately accurate for solving the aeroacoustics problems (Lighthill, 1992). Their amplitudes are often orders of magnitude smaller, and yet the frequencies are orders of magnitude larger than the flow field variations generating the sound. Further, high-fidelity is paramount for the resolution of acoustic problems; but a consistent, stable, and convergent, high-order scheme is not necessarily dispersion-relation preserving and thus does not necessarily guarantee a good quality numerical wave solution for an acoustic problem. Hence, among the requirements that should be placed on a CAA algorithm are the minimal dispersion and dissipation features. Demonstrated in the present paper is an independent evaluation of a dispersion-relation-preserving (DRP) scheme, first introduced by Tam and Webb (1993) based on the group velocity considerations, and a compatible set of radiation and outflow boundary conditions.

In the recent past, most commonly used computational methods have been of the acoustic analogy type. With such a method, the aeroacoustic problem is reduced to a nonhomogeneous wave equation for the noise, with its right side equal to a distribution of acoustic sources of strength related directly to the characteristics of the flow (Farassat and Brentner, 1988). Another method is the Kirchhoff approach, where exploiting the similarities between the aeroacoustic and the electrodynamics equations, the solution is obtained by integrating the wave equation external to some real or imaginary surface on which the relevant acoustic data is known (Lyrintzis, 1994). Perturbation methods for the linear potential equations have also been applied for the aeroacoustic problems. Since a quiescent or a uniform flow is generally assumed, the potential methods are similar to the acoustic analogy equations except that the dependent variable in the wave/convective-wave operator is the perturbation velocity potential (Atassi et al., 1990).

Perturbation Euler techniques have recently received attention from the aeroacoustics (Hariharan and Bayliss, 1985) as well as the unsteady-flow communities (Meadows et al., 1993). The direct simulations of acoustic wave propagation have also been tried by solving the full Navier-Stokes equations. For example, Ridder and Beddini (1992) simulated the radiation of sound from resonance tubes, and Baysal et al. (1994) investigated two devices to suppress the high tones generated by a high-speed cavity flow.

What is almost always common to these CAA solutions is the often intractable amount of time-dependent data generated. One way of reducing this data to understand the underlying physical phenomena is analyzing their spectrum, i.e., spectral analysis. A variety of methods are available to perform this task (Hardin, 1986). The spectra obtained from such analyses, however, may depend on the particular method that has been used.

Therefore, considering this *numerical data reduction* as an integral part of CAA, three spectral analysis methods were included in the present study: Blackman-Tukey (1959), periodogram (Bartlett, 1950), and weighted-overlapped-segment-averaging (Welch, 1967) methods. The former two of these methods were implemented using box-car and Hanning windows. The latter method was compared for different amounts of data-segment overlaps. Finally, these methods were applied not only for periodic but also for chaotic process data. For brevity, however, some details reported by Vanel (1994) were not included herein.

2 DRP Scheme

The two-dimensional, compressible Euler equations were considered to simulate the propagation of waves in a uniform mean flow. By superimposing small perturbations on a mean

Contributed by the Technical Committee on Vibration and Sound for publication in the JOURNAL OF VIBRATION AND ACOUSTICS. Manuscript received Jan. 1995; revised Oct. 1995. Associate Technical Editor: C. Fuller.

flow field, then by neglecting the higher order terms in perturbed quantities, these equations were *linearized:*

$$\frac{\partial U}{\partial t} + \frac{\partial E}{\partial x} + \frac{\partial F}{\partial y} = 0 \tag{2.1.a}$$

where the vector of unknowns (U) and flux vectors (E, F) were

$$U = \begin{bmatrix} \rho \\ u \\ v \\ p \end{bmatrix} \quad E = \begin{bmatrix} \rho_0 u + \rho u_0 \\ u_0 u + p/\rho_0 \\ u_0 v \\ u_0 p + \gamma p_0 u \end{bmatrix}$$

$$F = \begin{bmatrix} \rho_0 v \\ 0 \\ p/\rho_0 \\ \gamma p_0 v \end{bmatrix} \tag{2.1.b}$$

The density (ρ), pressure (p), and velocity (u, v) of the perturbed quantities are denoted without a subscript, but those of the mean flow are demarcated using the subscript 0. These variables were normalized using the following scales for length, velocity, time, density, and pressure, respectively: Δx (mesh step size), a_0 (speed of sound), $\Delta x/a_0$, ρ_0, and $\rho_0 a_0^2$.

Equations (2.1) support the acoustic, the entropy as well as the vorticity waves. The propagation characteristics of these waves (dispersion, dissipation, group and phase velocities, and isotropy or anisotropy) are encoded in their dispersion relations, which relate the angular frequency of the waves (ω) to the wave numbers of the space variables (α and β).

In order to capture the correct wave propagation characteristics, the dispersion relation of the finite-difference scheme should match as closely as possible the dispersion relation of the partial differential equations (PDE). This is equivalent to requiring that the effective wave number ($\bar{\alpha}$) and angular frequency ($\bar{\omega}$) of the numerical scheme must be close approximations to those of the PDE system for a large range of resolution. Such a scheme, therefore, is called a *dispersion-relation preserving* (DRP) scheme. In the remainder of this section, the way in which a DRP scheme was accomplished for the present computations is summarized.

The spatial derivatives of the linearized Euler equations (2.1) were discretized using a central seven-point stencil. For example, the derivative $\partial f/\partial x$ was approximated at the lth node of a *uniform* grid as

$$\left(\frac{\partial f}{\partial x}\right)_l \approx \frac{1}{\Delta x} \sum_{j=-3}^{3} a_j f_{l+j} \tag{2.2}$$

Expanding the right side of (2.2) in a Taylor series, five of the coefficients a_j were determined by equating coefficients of the same powers of Δx (standard way), leaving two coefficients, say a_1 and a_{-1}, to be determined. Since for a central difference $a_1 = -a_{-1}$, the resulting single parameter was determined by requiring that the numerical scheme and its corresponding original set of governing equations would have the same dispersion relation. This process starts with the Fourier transform of the finite difference approximation and the partial derivative term (right and left sides of (2.2), respectively). The result was the following relation between the numerical and exact wave numbers:

$$\bar{\alpha} = \frac{-i}{\Delta x} \sum_{j=-3}^{3} a_j e^{i\alpha j \Delta x} \tag{2.3}$$

Note that, $\bar{\alpha}\Delta x$ is a periodic function of $\alpha\Delta x$ with a 2π period. Then, a_1 was determined so that the integrated error E_1 between Δx and $\alpha\Delta x$ was minimum:

$$E_1 = \int_{-\eta}^{\eta} |\alpha\Delta x - \bar{\alpha}\Delta x|^2 d(\alpha\Delta x) \tag{2.4}$$

where $|\alpha\Delta x| < \eta$. The integration limit η is determined depending on the deviation of Eq. (2.3) from the 45-deg line (for $\alpha\Delta x > 1.45$) and the shortest wavelength desired to be simulated. (Note that if Real$(\bar{\alpha}\Delta x) = (\alpha\Delta x)$, the scheme is nondispersive, and if Imaginary$(\bar{\alpha}\Delta x) = 0$, the scheme is nondissipative.) Here this length was chosen to be the minimum possible, 4.5 Δx, hence $\eta = \pi/2$. (The choice of $\eta = 1.1$, which corresponds to the shortest wave length of 7 Δx, was later shown by Tam and Shen (1993) to produce better results for some waves.) This is a remarkable improvement over a standard, non-optimized, 6th-order scheme which can only resolve wave lengths longer than 10 Δx.

As for the time derivative $\partial U/\partial t$, it was approximated by a four-level finite difference, which, in a standard sense, could be up to 3rd-order accurate:

$$U^{n+1} - U^n \approx \Delta t \sum_{j=0}^{3} b_j \left(\frac{dU}{dt}\right)^{n-j} \tag{2.5}$$

where n is the time index. For the present scheme, however, the coefficients b_1, b_2 and b_3 were determined in terms of b_0, so that when both sides were expanded in Taylor series, Eq. (2.5) was satisfied to order $(\Delta t)^2$. Taking the Laplace transform of the left and right sides of Eq. (2.5), but with t defined as a continuous variable, the effective angular frequency $\bar{\omega}$ of the time discretization was found to be

$$\bar{\omega} = \frac{i(e^{-i\omega\Delta t} - 1)}{\Delta t \sum_{j=0}^{3} b_j e^{ij\omega\Delta t}} \tag{2.6}$$

The free parameter b_0 was then chosen to minimize the integrated error E_1 between $\bar{\omega}\Delta t$ and $\omega\Delta t$:

$$E_1 = \int_{-0.5}^{0.5} \left\{ \begin{matrix} \sigma[\mathrm{Re}(\bar{\omega}\Delta t - \omega\Delta t)]^2 \\ +(1-\sigma)[\mathrm{Im}(\bar{\omega}\Delta t - \omega\Delta t)]^2 \end{matrix} \right\} d(\omega\Delta t) \tag{2.7}$$

where σ is a weight that allows adjusting the compromise wished to impose on the optimization process between the dispersion (real part) and dissipation characteristics (imaginary part). The present long-term time computations were performed with $\sigma = 0.36$, which slightly biased the scheme in favor of a better dissipation character.

After discretizing all the terms in Eq. (2.1), the resulting DRP scheme for the *interior* points was as follows:

$$U_{l,m}^{n+1} = U_{l,m}^n + \Delta t \sum_{j=0}^{3} b_j K_{l,m}^{n-j} \tag{2.8a}$$

where

$$K_{l,m}^n = -\frac{1}{\Delta x} \sum_{j=-3}^{3} a_j E_{l+j,m}^n - \frac{1}{\Delta y} \sum_{j=-3}^{3} a_j F_{l,m+j}^n \tag{2.8b}$$

l and m are the spatial indices and n indicates the time level. The numerically stable maximum time step Δt was calculated from the Courant-Friedrichs-Lewy relation to be

$$\Delta t = \frac{\mathrm{CFL}}{1.75[M + \{1 + (\Delta x/\Delta y)^2\}^{1/2}]} \frac{\Delta x}{a_0} \tag{2.9}$$

where M denotes the mean flow Mach number and CFL = 0.4. However, after analyzing the numerical damping of the time integration scheme and with $\sigma = 0.36$, the CFL value was set to the more stringent value of 0.19.

Moving from the interior of the domain to the boundaries, they should be transparent to the disturbances reaching them to avoid any degradation of the numerical solution. For a right-

moving uniform mean flow as represented by the linearized Euler equations, and when all the disturbances (acoustic, entropy and vorticity) are generated in the interior of the domain, only acoustic waves reach the upper, lower and upstream boundaries; but, in addition to the acoustic waves, entropy and vorticity waves can reach the downstream boundary. Therefore, following Tam and Webb (1993) and from the asymptotic solutions of the finite difference form of Eq. (2.1), a set of radiation boundary conditions for all but the downstream boundary (in nondimensional form),

$$\frac{\partial U}{\partial t} + A\frac{\partial U}{\partial x} + B\frac{\partial U}{\partial y} + CU = 0 \qquad (2.10a)$$

where

$$A \equiv V\frac{x}{r},\ B \equiv V\frac{y}{r},\ C \equiv \frac{V}{2r}, \qquad (2.10b)$$

$$r = (x^2 + y^2)^{1/2}/\Delta x,\quad V = \frac{x}{r}M + \left(1 - \left(M\frac{y}{r}\right)^2\right)^{1/2} \qquad (2.10c)$$

and outflow boundary conditions for the downstream boundary,

$$\frac{\partial U'}{\partial t} + M\frac{\partial U'}{\partial x} = S \qquad (2.11a)$$

where

$$S = \left[\frac{\partial p}{\partial t} + M\frac{\partial p}{\partial x}, -\frac{\partial p}{\partial x}, -\frac{\partial p}{\partial y}\right]^T \qquad (2.11b)$$

were obtained. In Eq. (2.11), M denotes the Mach number and U' contains only the first three components of U in Eq. (2.1b). The pressure was obtained as in Eq. (2.10). The points in the boundary regions were calculated by discretizing these equations with the DRP approach: four-level time differencing and either a fully-backward or a fully-forward seven-point differences spatially.

The formal accuracy of the scheme was 4th-order in space and 2nd-order in time. The computational domain contained 200×200 equally-spaced grid points, surrounded by three rows of grid points to form each of the boundary regions.

3 Wave Propagation Simulation

The DRP scheme and its outflow and radiation boundary conditions were evaluated by considering three wave propagation cases: (i) a single acoustic pulse, (ii) three successive acoustic pulses, (iii) two simultaneous acoustic pulses. Each of these pulses were introduced into a uniform mean flow (left to right) with a Mach number of 0.5.

Each acoustic pulse was generated by setting $u = v = 0$ and imposing an initial Gaussian distribution for the pressure and density:

$$p = \rho = 0.01\ \exp\left[-\frac{\ln 2}{(3\Delta x)^2}(x^2 + y^2)\right] \qquad (3.1)$$

The computed pressure contours after 500 and 2000 time steps for the *single acoustic pulse* case are shown in Fig. 1. The results verified the expected propagation pattern: the radius of the acoustic wave expanded in time while its center was being entrained downstream with the mean flow. As shown in Fig. 1b, the waves exited from the downstream, top, and bottom boundaries without any numerical reflections. Presented in Fig. 2 is a comparison between the exact (Tam and Webb, 1993) and the numerical pressure wave forms at 500 and 2000 time steps. The numerical wave matches both the amplitude and the propagation speed of the exact wave.

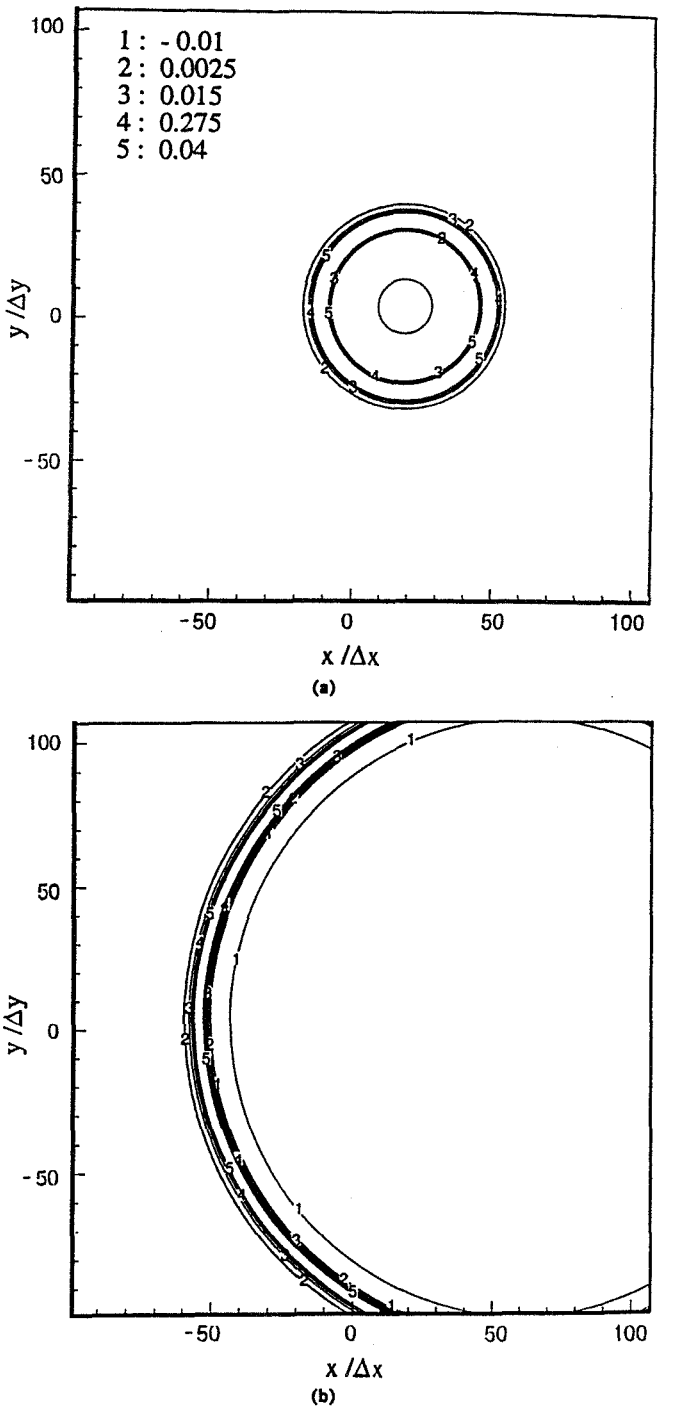

Fig. 1 Selected pressure contours of a single acoustic pulse after: (*a*) 500 and (*b*) 2000 time steps. Intensity relative to initial peak disturbance pressure.

To further test the effectiveness of the scheme and its boundary conditions, *three successive acoustic pulses* were generated in the center of the computational domain at $t = 0$, 600 Δt, and 1200 Δt. Displayed in Fig. 3 are the pressure contours at 1500 Δt. Again, the wave centers were being drifted in the direction of the mean flow while their radii expanded continuously in time. The computation was carried out for a longer period of time only to observe that all three pulses left the computational domain, in succession, without any noticeable reflections.

In the third wave propagation case, *two acoustic pulses* were generated *simultaneously:* one in the center of the computational domain and the other 50 Δx upstream of the outflow boundary

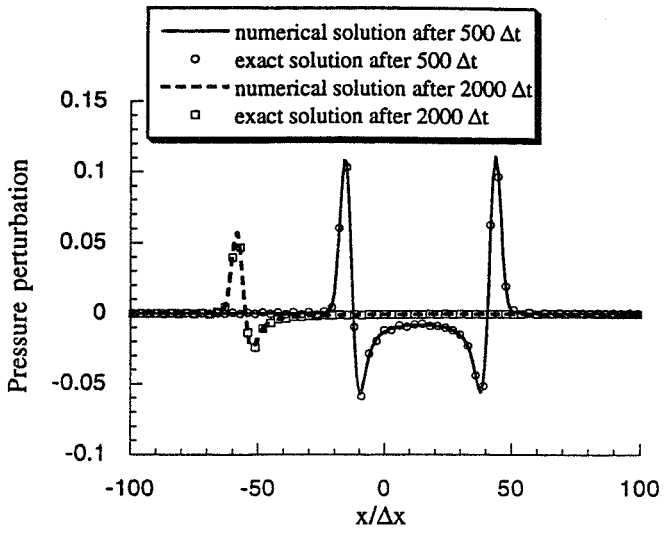

Fig. 2 Pressure wave form of a single acoustic pulse at the center.

(as compared to the pulses generated 100 Δx away in the prior cases). The pressure contours at instants 500 Δt and 2000 Δt are plotted in Fig. 4. It was observed that the two pulses intersected as they propagated radially and drifted downstream. The interaction of the waves was crisply simulated. Small reflections started appearing (Fig. 4*b*) when both wave systems were exiting the outflow boundary. The primary suspect was the implementation of the boundary conditions at the boundary corners. In fact, when the case was repeated on a four times larger domain (400 × 400 grid), now clear from the corners, the waves exited without any reflections (Fig. 5). Enlarging the domain, however, also placed the second source 150 Δx upstream of the outflow boundary. And, since the boundary conditions (Eqs. (2.10)–(2.11)) were developed from the asymptotic solutions, their degradation for sources close to a boundary might not be entirely unexpected.

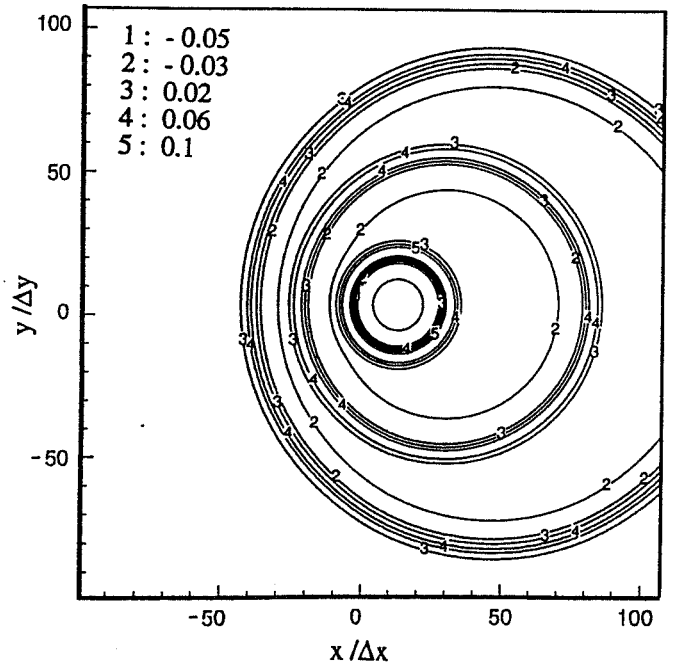

Fig. 3 Selected pressure contours of successive acoustic pulses after 1500 time steps. Intensity relative to initial peak disturbance pressure.

4 Spectral Analysis Methods

Two traditional methods for the spectral analysis of a stationary process are the *Blackman-Tukey* (BT) and the *periodogram* (PM) methods. In the BT method, first the autocorrelation of the record of N data values was computed:

$$\hat{R}(\tau) = \frac{1}{N-\tau} \sum_{n=0}^{N-\tau-1} x(n\Delta t)x((n+\tau)\Delta t), \qquad \tau = 0, \ldots, \tau_{\max} \quad (4.1)$$

where $\tau_{\max}$ was the maximum lag value obtained as the recipro-

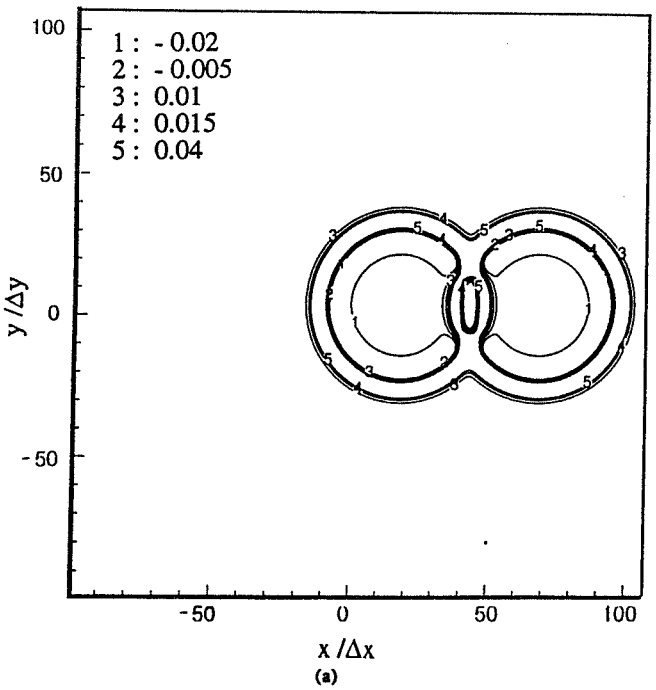

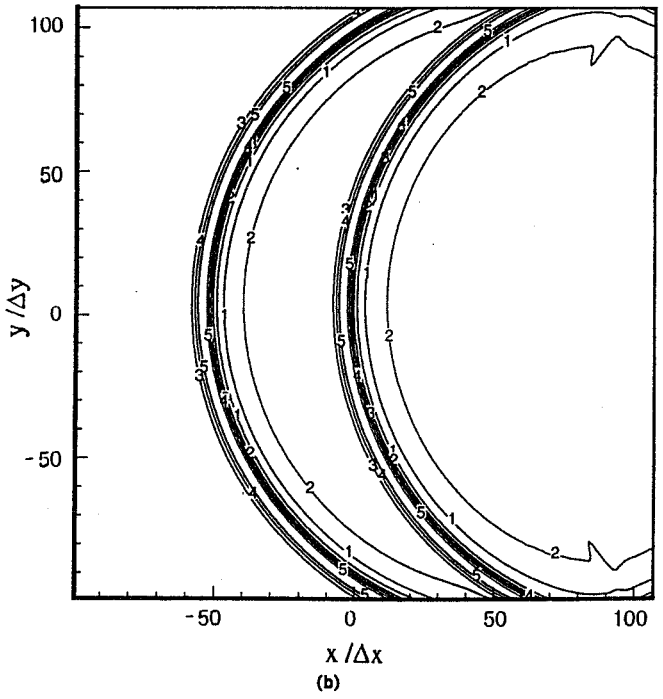

Fig. 4 Selected pressure contours of multiple acoustic pulses after: (*a*) 500 and (*b*) 2000 time steps. Intensity relative to initial peak disturbance pressure.

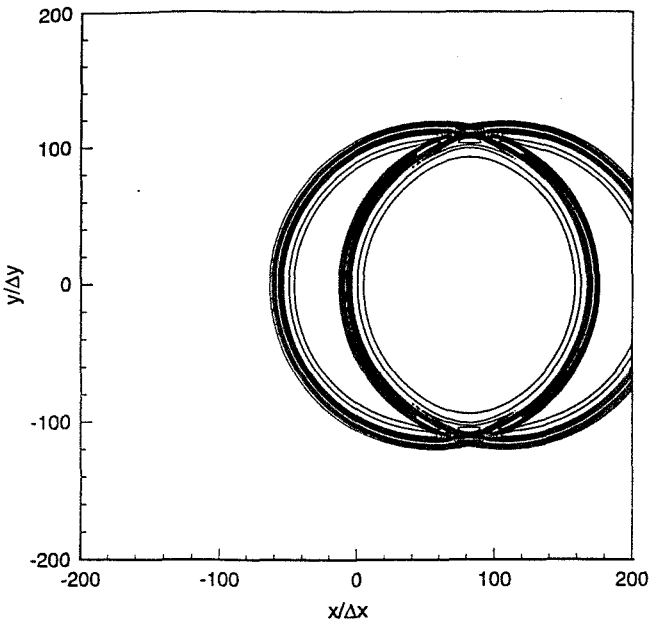

Fig. 5 Selected pressure contours of multiple acoustic pulses after 2000 time steps computed on an enlarged (400 × 400) domain. Intensity relative to initial peak disturbance pressure.

cal of twice the frequency resolution. Then, the power spectrum estimate was obtained by Fourier transforming Eq. (4.1):

$$\hat{P}(f_k) = \Delta t\{\hat{R}(0) + 2\sum_{\tau=1}^{\tau_{\max}-1}\hat{R}(\tau)\cos(\pi k\tau/\tau_{\max})\} \quad (4.2)$$

where

$$f_k = \frac{k}{N\Delta t} \quad \text{and} \quad k = 0, 1, \ldots, N/2 \quad (4.3)$$

In the PM method, however, the power spectrum was obtained by taking directly the Fourier transform of the time domain record to be analyzed. For a sampled data record $x(n\Delta t)$, where $n = 0, \ldots, N-1$, the power spectrum was

$$\hat{P}(f_k) = \frac{1}{N\Delta t}\left|\Delta t\sum_{n=0}^{N-1}x(n\Delta t)\exp\left(-j2\pi\frac{nk}{N}\right)\right|^2 \quad (4.4)$$

where $j = \sqrt{-1}$ and f_k was defined as in Eq. (4.3). The highest frequency that could be reproduced from the data sampled at equal intervals Δt was the Nyquist frequency, $f_{N/2}$.

Three main problems arising when employing these methods were taken into consideration: the *resolution,* the *leakage,* and the *statistical variability* of the spectral estimates. A key parameter in obtaining a reliable and accurate spectrum was the frequency resolution Δf: the smaller the Δf was (longer record length) the more accurate and detailed the spectrum estimate became. A good resolution implied that each peak of the spectrum estimate appeared sharply and distinctively. The leakage manifested itself by smearing the spectral estimate, i.e., energy in the main lobe of a spectral response *leaked* into the sidelobes, distorting other spectral responses that were present. This was due to the implicit windowing of the data that occurred when processing with the Fourier transform, as explained briefly below.

The finite Fourier transform of a finite data record $x(t)$ with length T may be viewed as the Fourier transform of an unlimited time record $v(t)$ multiplied by a *boxcar window* denoted by a function box (t):

$$x(t) = \text{box}(t)v(t) \quad (4.5)$$

where

$$\text{box}(t) = \begin{cases} 1, & \text{for} \quad 0 \le t \le T \\ 0, & \text{for} \quad t < 0 \quad \text{or} \quad t > T \end{cases} \quad (4.6)$$

Then, the Fourier transform of the boxcar window was a function of type $\sin x/x$, instead of a Dirac function, as it would be in the ideal case of having an infinite value of T. In order to reduce the side-lobe leakage, a window with small side lobes had to be used instead of the boxcar window. For this purpose, the *Hanning window* is commonly used:

$$h(t) = \begin{cases} 0.5\left(1 - \cos\dfrac{2\pi t}{T}\right), & 0 \le t \le T \\ 0, & t < 0 \quad \text{or} \quad t > T \end{cases} \quad (4.7)$$

Unfortunately, the side effect of side-lobe leakage reduction was always a broadening in the main lobe of the window transform. As a result, the main lobe of the Hanning window transform was twice as large as that of the boxcar window transform. This implied a reduction in the resolution quality by a factor of two.

When the data of a *chaotic process* were to be analyzed, the problem of *variability* in the spectrum estimates, due to the limited length of the data record, also needed to be taken into consideration. A source of statistical error had been the time history tapering operation occurring in the PM method. It essentially discarded the relevant information near the beginning and the end of each record. To alleviate this increase in variability, the *weighted-overlapped-segment-averaging* (WOSA) was employed. In this method, the data record $x(t)$ was broken into n_d blocks, each consisting of N data values (Baysal et al., 1994). The power spectrum was then obtained by first taking the Fourier transform of the data over each block,

$$X_i(f_k) = \Delta t\sum_{n=1}^{N}x_i(n)\exp\left(-j2\pi\frac{(n-1)(k-1)}{N}\right)$$

for

$$i = 1, \ldots, n_d;\ n = 1, \ldots, N;\ k = 1, \ldots, N/2 \quad (4.8)$$

then, averaging over the resulting spectra over all the blocks

$$\hat{P}(f_k) = \frac{1}{n_d N\Delta t}\sum_{i=1}^{n_d}|X_i(f_k)|^2$$

for

$$k = 1, 2, \ldots, N/2 \quad (4.9)$$

Then, the data in each block was tapered by the Hanning window to suppress the side-lobe leakage.

5 Spectral Analysis Results

The selected spectral methods for the present study were tested for their relative performance in analyzing periodic as well as chaotic processes. Since the waves considered in §.3 would have trivial spectra, the periodic data record was generated by a multiple-frequency cosine function:

$$F(t) = \cos(2\pi f_0 t) + \cos(2\pi f_1 t) + \cos(2\pi f_2 t) + 0.5\cos(2\pi f_3 t) + 0.1\cos(2\pi f_4 t) \quad (5.2)$$

where the f values in kHz were: $f_0 = 1, f_1 = 1.1, f_2 = 2, f_3 = 0.5, f_4 = 0.2$. The data were sampled at the frequency resolution of 10 kHz. Equation (5.2) was a good benchmark problem to illustrate the concepts of leakage and resolution, and to test the BT and PM methods in estimating such *steep-sloped* spectra.

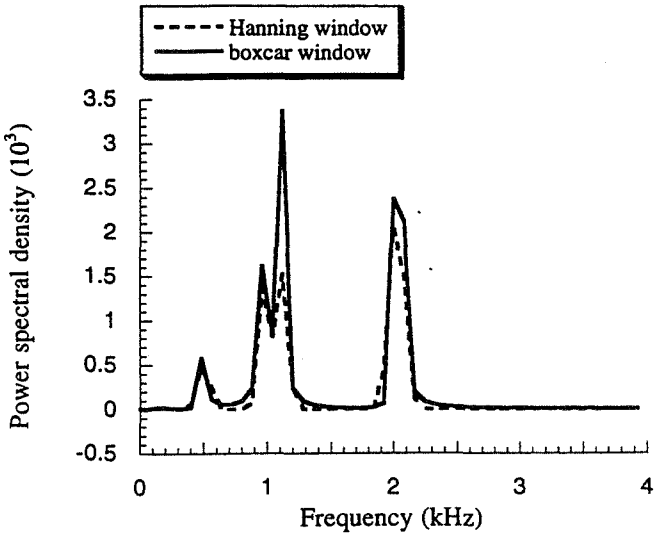

Fig. 6 Power spectral density for multiple-frequency cosine function as represented by the periodogram method and different windows with resolution Δf = 80 Hz.

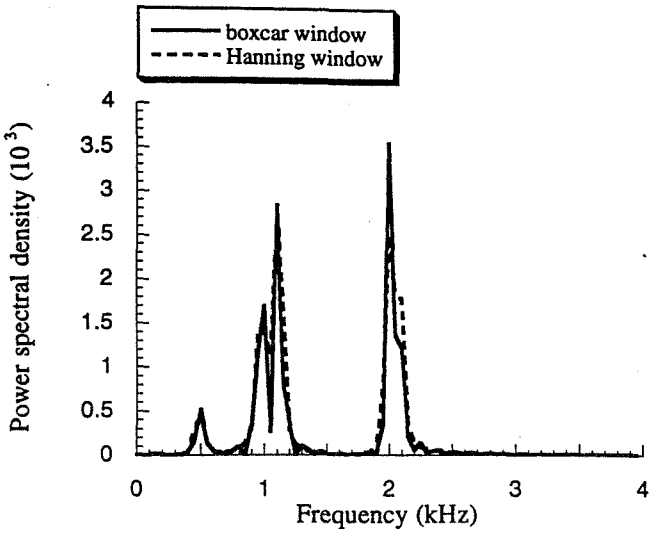

Fig. 8 Power spectral density for multiple-frequency cosine function as represented by the periodogram method and different windows with resolution Δf = 50 Hz.

For each method, the spectra were computed in four different ways by varying the resolution (Δf = 80 Hz and 50 Hz) and by varying the windowing (boxcar and Hanning).

In the PM results that are shown in Fig. 6, note the presence of leakage, i.e., non-zero values of the spectrum at frequencies off the peaks. These were reduced with the use of the Hanning window. Also, when the Hanning window was used, the off-peak SPL values were much lower (less leakage) than when the boxcar window was used. Figure 7 displays the power spectra obtained using the BT method. The distortion effect caused by the leakage appeared to be more prevalent as compared with the PM method. The large side lobes of the boxcar window were suppressed with the use of the Hanning window. However, the Hanning tapering yielded negative values and less side-lobe suppression in this case, as compared to its use with the PM method. From Figs. 6 and 7, it was also observed that the PM method produced four of the five peaks (f_0, f_1, f_2, f_3); whereas, the BT method could only produce three of them (f_0, f_2, f_3).

In an attempt to demonstrate the effect of the frequency resolution, the spectra, initially obtained with Δf = 80 Hz, were repeated with Δf = 50 Hz. Shown in Figs. 8 and 9 are the PM and BT spectra, respectively, and they should be contrasted with Figs. 6 and 7. Lower frequency resolution resulted in more accurate spectrum representation. The effect of window tapering on the spectrum resolution was observed in Figs. 8 and 9: the peaks at f_0 and f_1 were not as distinct when the Hanning window was used.

The next set of results were obtained for a *chaotic* process. The data record was obtained from Baysal et al. (1994): a computational simulation of a turbulent, transonic flow past a two-dimensional cavity with a length-to-depth ratio of 4.5. The instantaneous-pressure history was for a specific location inside the cavity. The SPL spectra were obtained using not only the WOSA (Figs. 10–13) but also the PM (Fig. 14) and the BT (Fig. 15) methods. An important parameter for the WOSA method is the amount of overlapping. This aspect was studied by comparing two different overlap cases with no overlapping (Figs. 11–13).

The spectra shown in Figs. 10 and 11 were obtained by partitioning the data into three blocks with 50% of overlapping

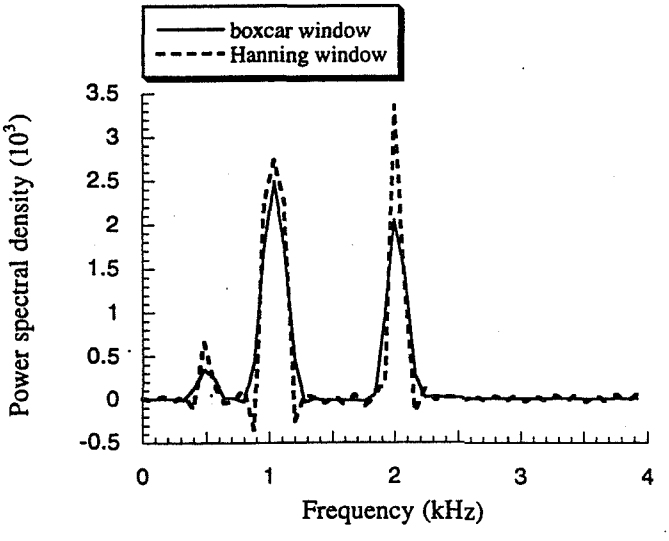

Fig. 7 Power spectral density for multiple-frequency cosine function as represented by Blackman-Tukey method and different windows with resolution Δf = 80 Hz.

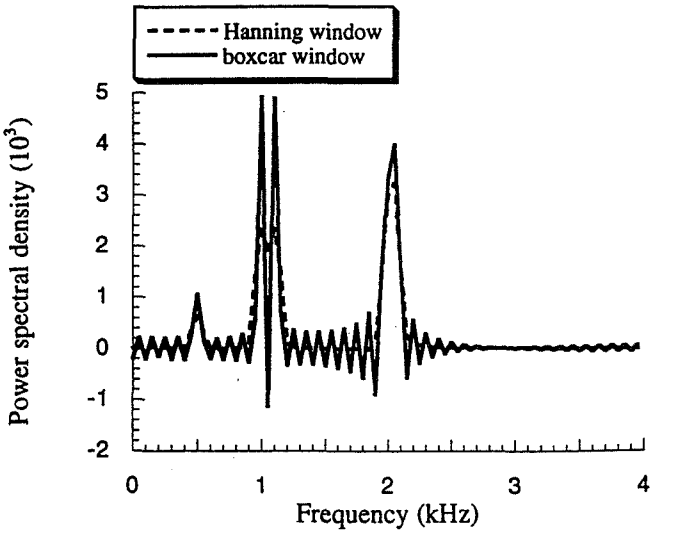

Fig. 9 Power spectral density for multiple-frequency cosine function as represented by Blackman-Tukey method and different windows with resolution Δf = 50 Hz.

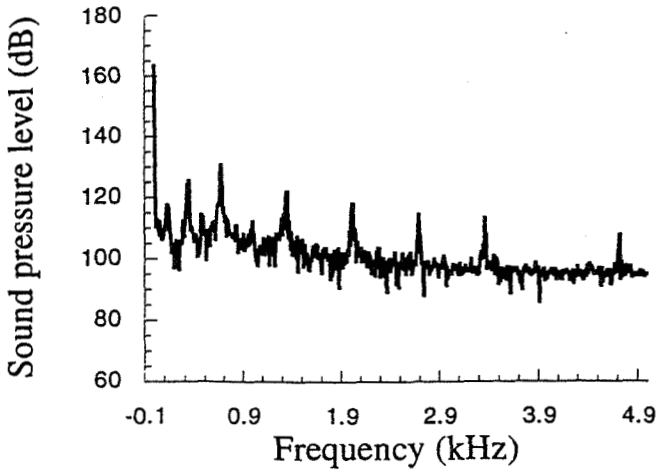

Fig. 10 Sound pressure levels in a cavity as represented by WOSA method and boxcar window with 50 percent overlapping.

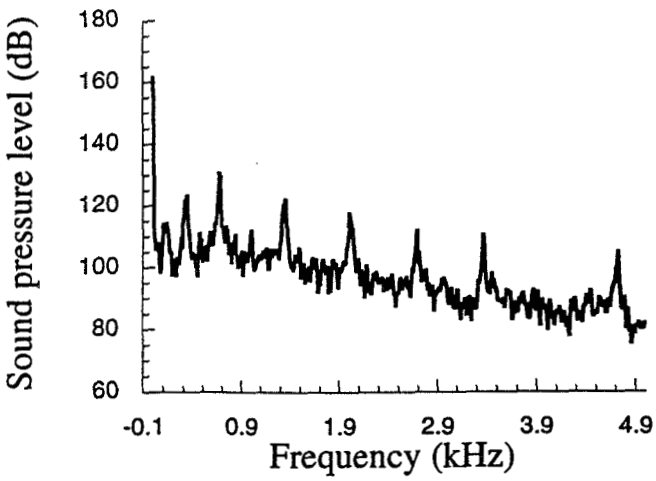

Fig. 11 Sound pressure levels in a cavity as represented by WOSA method and Hanning window with 50 percent overlapping.

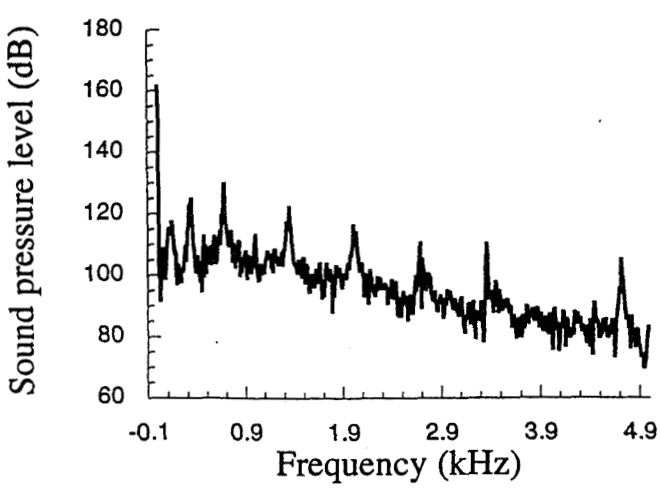

Fig. 12 Sound pressure levels in a cavity as represented by WOSA method and Hanning window with no overlapping.

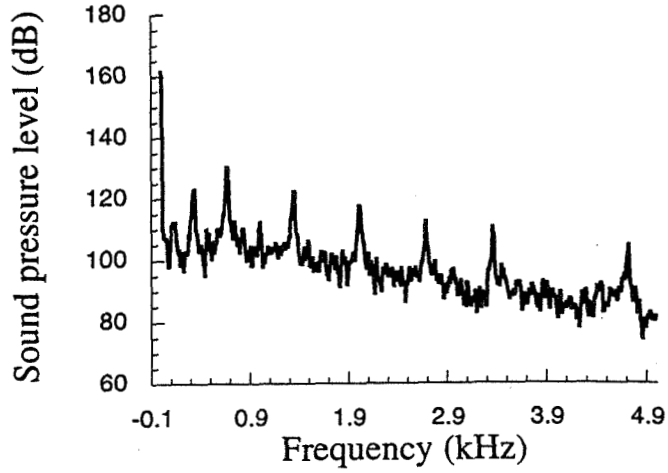

Fig. 13 Sound pressure levels in a cavity as represented by WOSA method and Hanning window with 75 percent overlapping.

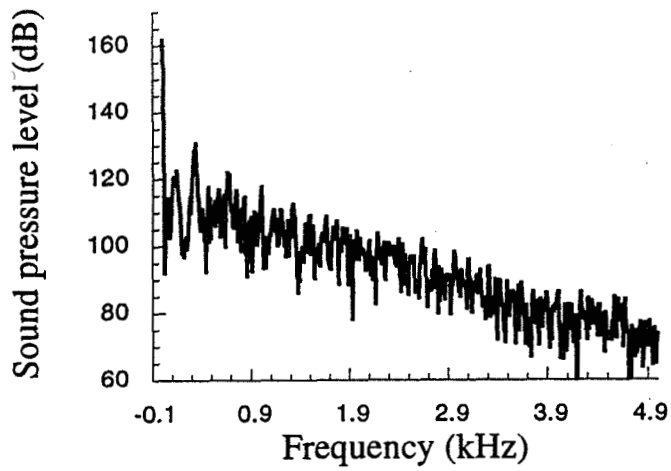

Fig. 14 Sound pressure levels in a cavity as represented by periodogram method and Hanning window.

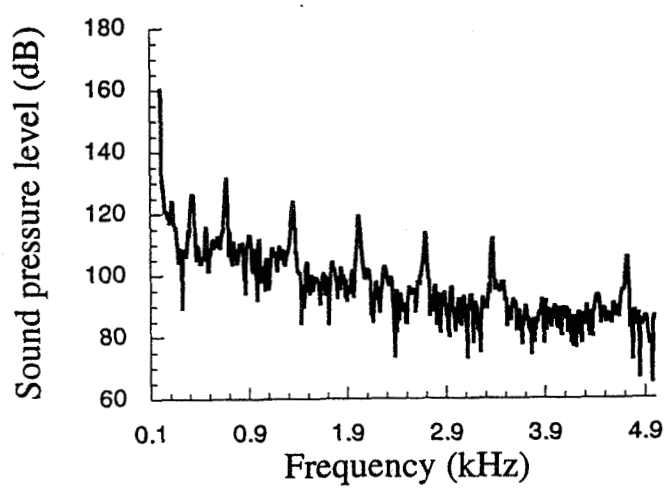

Fig. 15 Sound pressure levels in a cavity as represented by Blackman-Tukey method and Hanning window.

between them. The spectral peaks appeared more clearly (especially, for higher frequencies) when the Hanning window tapering was done. It was also noted, that the broadband SPL decreased in intensity with increasing frequency, whereas it remained roughly constant when a boxcar window was used. Comparing the spectra of 50% overlapping with no overlapping (Fig. 12), it was seen that the no-overlapping spectrum contained more local peaks. Also, since Fig. 11 displayed crisper

peaks and less variation, it was concluded that overlapping increased the stability. However, almost no distinguishable differences appeared between the spectrum with 50% overlapping and the one obtained with 75% overlapping (Fig. 13). Since the amount of overlapping increased the number of Fourier transform operations, using more than 50% overlapping did not appear to be feasible. This was in agreement with Otnes and Enochson (1972) that 50% overlapping retrieves about 90% of the stability lost due to the tapering operation, hence it has been more commonly used.

When the PM method with a Hanning window was used (Fig. 14), more local peaks were generated (as compared to Fig. 12), and only the ones located in the lower end of the spectrum were clearly distinguishable. However, the spectrum obtained by using the BT method with a Hanning window (Fig. 15) compared very well with the ones obtained using the WOSA method and 50% overlapping.

6 Conclusions

The present results showed that the DRP scheme was reliable to yield accurate simulations of isotropic waves with wavelengths as small as 4.5 Δx. The radiation and outflow boundary conditions were very effective unless a disturbance source was placed close to a boundary corner.

In order for the scheme to be of more practical interest, it was deemed necessary to investigate its extensions for: (i) nonuniform grids, (ii) multiblock grids, (iii) time integration requiring less computer storage, and (iv) for the nonlinear equations with a controllable amount of numerical dissipation. Also, both from the efficiency and the accuracy points of view, replacing the present finite-difference (local) boundary conditions with integral (global) boundary conditions should prove to be profitable.

For the spectral analysis of the time-domain data obtained from a periodic process with a steep-sloped spectrum, the PM method produced better estimates than the BT method on the basis of minimum leakage. The Hanning window, when used with the BT method, was found to yield less leakage suppression than when it was used with the PM method.

For a chaotic process, on the other hand, the WOSA and BT methods were shown to yield stable results of comparable quality. In the WOSA method, the extra computational cost of overlapping more than 50% could not be justified. Although the methods were not methodically studied for their relative computational efficiencies, merely based on the operation count, it was estimated that the WOSA method would be more economical than the BT method.

Finally, it was demonstrated that the very same time-dependent data, whether it be periodic or chaotic, could easily be interpreted discrepantly as for its quality and the underlying physical message, depending on the spectral analysis method employed.

Acknowledgment

This work was supported by NASA Langley Research Center under Grant NAG-1-1499. Technical monitors were J. L. Thomas, J. M. Luckring and D. S. Miller. Help by D. K. Kaushik was appreciated.

7 References

Atassi, H. M., Subramanian, S., and Scott, J. R., 1990, "Acoustic Radiation from Lifting Airfoils in Compressible Subsonic Flow," AIAA Paper 90-3911, 13th Aeroacoustics Conference, Tallahassee, FL.

Bartlett, M. S., 1950, "Periodogram Analysis and Continuous Spectra," *Biometrika*, Vol. 37, pp. 1–16.

Baysal, O., Yen, G. W., and Fouladi, K., 1994, "Navier-Stokes Computations of Cavity Aeroacoustics With Suppression Devices," ASME JOURNAL OF VIBRATION AND ACOUSTICS, Vol. 116, pp. 105–112.

Blackman, R. B., and Tukey, J. W., 1959, *The Measurement of Power Spectra From the Point of View of Communications Engineering*, Dover Publishers, New York, NY.

Farassat, F., and Brentner, K. S., 1988, "The Uses and Abuses of the Acoustic Analogy in Helicopter Rotor Prediction," *Journal of the American Helicopter Society*, Vol. 33, No. 1, pp. 29–36.

Hardin, J. C., 1986, *Introduction to Time Series Analysis*, NASA Reference Publication No. 1145.

Hardin, J. C., 1993, "Recent Insights into Computational Aeroacoustics," *Computational Aero- and Hydro-acoustics*, R. R. Mankbadi, A. S. Lyrintzis, O. Baysal, L. A. Povinelli, M. Y. Hussaini, eds., FED-Vol. 147, p. 1, ASME, New York, NY.

Hariharan, S. I., and Bayliss, A., 1985, "Radiation of Sound from Unflanged Cylindrical Ducts," *SIAM Journal on Scientific and Statistical Computing*, Vol. 7, No. 2.

Lighthill, J., 1992, "Report on the Final Panel Discussion on Computational Aeroacoustics," ICASE Report No. 92-53, NASA Langley Research Center, Hampton, VA.

Lyrintzis, A. S., 1994, "Review: The Use of Kirchoff's Method in Computational Aeroacoustics," ASME *Journal of Fluids Engineering*, Vol. 116, No. 4, pp. 665–676.

Meadows, K. R., Caughey, D. A., and Casper, J., 1993, "Computing Unsteady Shock Waves for Aeroacoustic Applications," AIAA Paper 93-4329, 15th Aeroacoustics Conference, Long Beach, CA.

Otnes, R. K., and Enochson, L., 1972, *Digital Time Series Analysis*, Wiley-Interscience, New York, NY.

Ridder, J. P., and Beddini, R. A., 1992, "Temporal and Acoustic Accuracy of an Implicit Upwind Method for Ducted Flows," *AIAA Journal*, Vol. 29, No. 11, pp. 1860–1867.

Tam, K. W., and Webb, J. C., 1993, "Dispersion-Relation-Preserving Finite Difference Schemes for Computational Acoustics," *Journal of Computational Physics*, Vol. 107, pp. 262–283.

Tam, C. K. W., and Shen, H., 1993, "Direct Computation of Nonlinear Acoustic Pulses using Higher-Order Finite Difference Schemes," AIAA Paper 93-4325, 15th Aeroacoustics Conference, Long Beach, CA.

Vanel, F. O., 1994, "Investigation of Computational and Spectral Analysis Methods for Aeroacoustic Wave Propagation," Master's Thesis, Old Dominion University, Norfolk, VA.

Welch, P. D., 1967, "The Use of FFT for the Estimation of Power Spectra: A method based on time averaging over short modified periodograms," *IEEE Transactions on Audio Electroacoustics*, Vol. AU-15, No. 2, pp. 70–73.

ALGORITHMIC EXTENSIONS OF LOW-DISPERSION SCHEME AND MODELING EFFECTS FOR ACOUSTIC WAVE SIMULATION

Dinesh K. Kaushik and Oktay Baysal

Aerospace Engineering Department
Old Dominion University
Norfolk, Virginia 23529-0247 USA

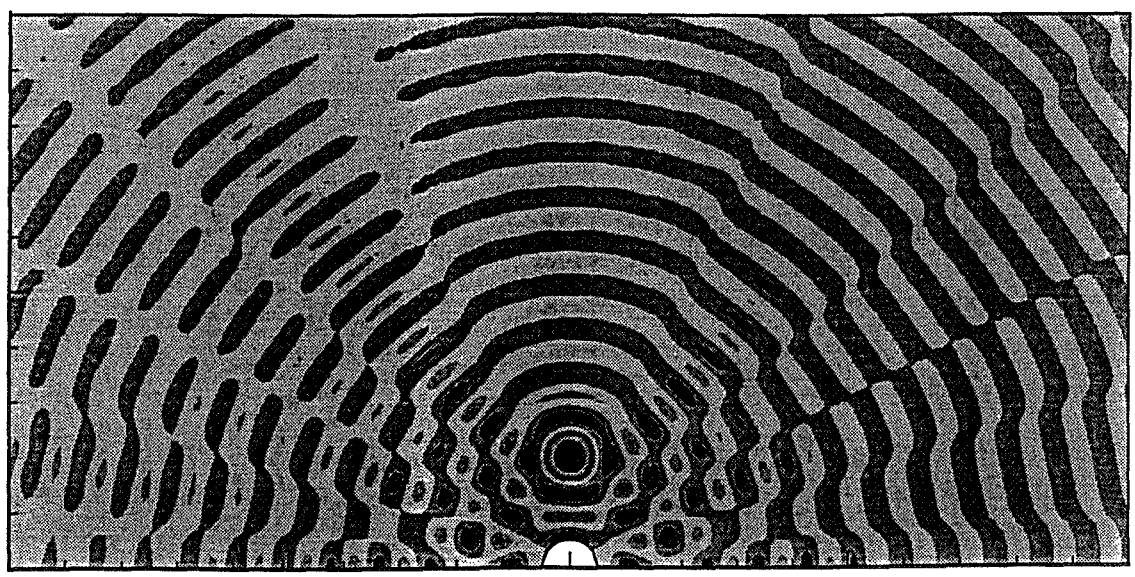

Preprint from

Computational Aeroacoustics 1996
(Editors: A. Lyrintzis and O. Baysal)
Fluids Engineering Conference
July 7-11, 1996 / San Diego, California
The American Society of Mechanical Engineers

Proc. ASME Fluids Engineering Division Summer Meeting, 1996
FED-Vol. 238, pp. 503-510.
(Revised)

ALGORITHMIC EXTENSIONS OF LOW-DISPERSION SCHEME AND MODELING EFFECTS FOR ACOUSTIC WAVE SIMULATION

Dinesh K. Kaushik and Oktay Baysal

Aerospace Engineering Department
Old Dominion University
Norfolk, Virginia 23529

Abstract

Accurate computation of acoustic wave propagation may be more efficiently performed when their dispersion relations are considered. Consequently, computational algorithms which attempt to preserve these relations have been gaining popularity in recent years. In the present paper, the extensions to one such scheme are discussed. By solving the linearized, 2-D Euler and Navier-Stokes equations with such a method for the acoustic wave propagation, several issues were investigated. Among them were higher-order accuracy, choice of boundary conditions and differencing stencils, effects of viscosity, low-storage time integration, generalized curvilinear coordinates, periodic sources, their reflections and interference patterns from a flat wall and scattering from a circular cylinder. The results were found to be promising en route to the aeroacoustic simulations of realistic engineering problems..

Introduction

Computational aeroacoustics (CAA) may be defined as the application of numerical techniques for the direct calculation of aerodynamic sound generation and propagation starting from the first principles. Most computational fluid dynamics (CFD) schemes, however, are not adequately accurate for solving the aeroacoustics problems (Lighthill, 1992). Their amplitudes are often orders of magnitude smaller, and yet the frequencies are orders of magnitude larger than the flow field variations generating the sound. Further, high-fidelity is paramount for the resolution of acoustic problems; but a consistent, stable, and convergent, high-order scheme is not necessarily dispersion-relation preserving and thus does not necessarily guarantee a good quality numerical wave solution for an acoustic problem. Hence, among the requirements that should be placed on a CAA algorithm are the minimal dispersion and dissipation features (Tam and Webb, 1993).

The direct simulations of acoustic wave propagation have been tried by solving the full Navier-Stokes equations. For example, Baysal et al. (1994) investigated two devices to suppress the high tones generated by a high-speed cavity flow, using an unsteady computational fluid dynamics (CFD) method. The comparisons with experimental data were acceptable for engineering purposes. However, it was realized that the dissipative and dispersive characteristics of a typical second-order CFD method would preclude a long-term wave propagation simulation. Also, various studies (e.g. Mankbadi et al., 1993, Lyrintzis et al., 1995, and Hardin et al., 1995) have suggested that the direct simulations of the flow equations for the acoustic wave propagation using the higher-order CFD schemes could become prohibitively expensive, since the number of grid points per wavelength would be excessively high (ideally should not exceed ten).

Therefore, a fourth-order accurate dispersion-relation-preserving (DRP) method was previously investigated for a variety of wave propagation problems (Vanel and Baysal, 1995). A number of observations and recommendations were made for future investigations to extend the scheme to solve some application problems. The present investigation started precisely with this impetus. A selection of the issues explored, all for linear cases, are reported herein. These include higher-order accuracy (up to sixth-order), choice of boundary conditions and differencing stencils, effects of viscosity, low-storage time integration, generalized curvilinear coordinates, periodic sources, their reflections and interference patterns from a flat wall and scattering from a circular cylinder. The extensions for the nonlinear acoustics are deferred to another paper for brevity.

Governing Equations

The two-dimensional, compressible Navier-Stokes and Euler equations were considered in generalized curvilinear coordinates. In the absence of curved or irregularly shaped boundaries, their Cartesian expressions were preferred. By superimposing small perturbations on a mean flow field, then by neglecting the higher order terms in perturbed quantities, these equations were *linearized* to simulate the propagation of waves in a uniform mean flow.in x-direction.

$$\frac{\partial \hat{U}}{\partial t} = -R(\hat{U}) + S \text{ , where } R(\hat{U}) = \frac{\partial \hat{E}}{\partial \xi} + \frac{\partial \hat{F}}{\partial \eta} \qquad (1.a)$$

The flux vectors ($\hat{E},\hat{F}$) were obtained through transformations,

$$\hat{E}=[\xi_x(E-E_v)+\xi_y(F-F_v)]/J,$$
$$\hat{F}=[\eta_x(E-E_v)+\eta_y(F-F_v)]/J \qquad (1.b)$$

where the vector of unknowns ($\hat{U}$) and the physical fluxes were

$$\hat{U}=\frac{1}{J}\begin{bmatrix}\rho\\ u\\ v\\ p\end{bmatrix},\quad E=\begin{bmatrix}\rho_0 u+\rho u_0\\ u_0u+p/\rho_0\\ u_0v\\ u_0p+\gamma p_0u\end{bmatrix},\quad F=\begin{bmatrix}\rho_0 v\\ 0\\ p/\rho_0\\ \gamma p_0 v\end{bmatrix} \qquad (1.c)$$

$$E_v=\frac{1}{\rho_0}\begin{bmatrix}0\\ \tau_{xx}\\ \tau_{yx}\\ 0\end{bmatrix},\quad F_v=\frac{1}{\rho_0}\begin{bmatrix}0\\ \tau_{xy}\\ \tau_{yy}\\ 0\end{bmatrix} \qquad (1.d)$$

The diffusion terms in the energy equation were omitted due to their perceived secondary influence on most of the acoustic wave propagation phenomena. Also, the second coefficient of viscosity was neglected, effectively negating the rotational effect of a fluid element but leaving its deformation-rate in the shear stresses.

$$\tau_{x_ix_j}=\frac{\mu_0}{\rho_0 a_0\Delta x}\left(\frac{\partial u_i}{\partial x_j}+\frac{\partial u_j}{\partial x_i}\right) \qquad (1.e)$$

The density (ρ), pressure (p), and velocity (u,v) of the perturbed quantities are denoted without a subscript, but those of the mean flow are demarcated using the subscript 0. These variables were then normalized using the following scales for length, velocity, time, density, and pressure, respectively: Δx (mesh step size), a_0 (speed of sound), $\Delta x/a_0$ ρ_0, and $\rho_0 a_0^2$. Finally, S in eq. (1) denotes a possible acoustic source.

Computational Method

Equation (1) supports the acoustic, the entropy as well as the vorticity waves. The propagation characteristics of these waves (dispersion, dissipation, group and phase velocities, and isotropy or anisotropy) are formulated in their dispersion relations, which relate the angular frequency of the waves (ω) to the wave numbers of the space variables (α). Therefore, in order to capture the correct wave propagation characteristics, the dispersion relation of the finite-difference scheme should match as closely as possible the dispersion relation of the partial differential equations (PDE). This is equivalent to requiring that the effective wave number ($\bar{\alpha}$) and effective angular frequency ($\bar{\omega}$) of the numerical scheme must be close approximations to those of the PDE system for a large range of resolution. Such a scheme, therefore, is called a *dispersion-relation preserving* (DRP) scheme. The way in which the *baseline* DRP scheme of Tam and Webb (1993) and Tam and Shen (1993) was accomplished for the present development is given by Vanel and Baysal (1995).

In discretizing the spatial derivatives, the DRP was achieved by determining the coefficients (a_j) from the Taylor series expansion as a one-parameter family; then the remaining coefficient was determined from the minimization of the discrepancy between the numerical (effective) wave number $\bar{\alpha}$ and the exact wave number α, by integrating the square of their difference for a desired range $(-\varepsilon,\varepsilon)$, where $|\alpha\Delta x|\prec\varepsilon$. Note that, $\bar{\alpha}\Delta x$ is a periodic function of $\alpha\Delta x$ with a 2π period, and if $Real(\bar{\alpha}\,\Delta x)=(\alpha\,\Delta x)$, the scheme is nondissipative, and if $Imaginary(\bar{\alpha}\,\Delta x)=0$, the scheme is nondispersive. The integration limit ε is determined depending on the shortest wavelength desired to be simulated. For example, in the 4-th order version of the present schemes, two choices of ε were tried: $\pi/2$ and 1.1, which corresponded to the minimum wavelengths of 4.5 Δx and 7 Δx, respectively. This is a remarkable improvement over a standard sixth-order scheme which can only resolve wave lengths longer than 10 Δx.

The time integration of eq. (1) was performed in two different ways. In the first approach, a four-point finite difference, which in a standard sense could be up to third-order accurate, was derived from the Taylor series as a one-parameter family. The remaining coefficient (b_j) was determined, as in the spatial coefficients, by minimizing the discrepancy between the effective and the exact dispersion relations. After discretizing all the terms in eq. (1), the resulting $\vartheta(\Delta t^2,\Delta x^{N+M-2})$-accurate DRP scheme was as follows:

$$\hat{U}^{n+1}_{\ell,m}=\hat{U}^{n}_{\ell,m}+\Delta t\sum_{j=0}^{3}b_j\,R^{n-j}_{\ell,m} \qquad (2.a)$$

where $$R^{n}_{\ell,m}=-\frac{1}{\Delta\xi}\sum_{j=-N}^{M}a_j\hat{E}^{n}_{\ell+j,m}-\frac{1}{\Delta\eta}\sum_{j=-N}^{M}a_j\hat{F}^{n}_{\ell,m+j} \qquad (2.b)$$

ℓ and m are the spatial indices and n indicates the time level. For N=M, difference eq. (2.) is central, for N=0, it is fully forward, and for M=0, it is fully backward. All the interior cells were computed using central differences. However, since these high-order stencils require multiple layers of boundary cells, all combinations between a central and a fully-one-sided difference need also be derived. Only then, it would be possible to always utilize the information from the nearest possible points for better accuracy. In the present computations a fourth-order scheme and a sixth-order scheme were derived, requiring 7-point stencil (*N takes values from 6 to 0, M takes values from 0 to 6, and N+M=6*) and 9-point stencil (*N takes values from 8 to 0, M takes values from 0 to 8, and N+M=8*) , respectively.

The numerically stable maximum time step Δt was calculated from the Courant-Friedrichs-Lewy relation. For example, for the fourth-order scheme in Cartesian coordinates, the stable CFL number was found to be 0.4. However, after analyzing the numerical damping of the time integration scheme, the CFL value was set to the more stringent value of 0.19.

Since the above time integration scheme required the storage of four time levels, a relatively lower storage alternative, such as the Runge-Kutta scheme, was considered. The classical Runge-Kutta schemes, however, are intrinsically dissipative and dispersive. Recently, a class of low-dissipation and low-dispersion Runge-Kutta schemes have been developed by Hu et

al. (1994). Its development was similar to that of eq. (2), such that the dissipation and dispersion errors were minimized for all the frequencies resolvable by the numerical discretization. Most importantly, these schemes can be implemented with low-storage requirements. The resulting scheme had the spatial integration identical to eq. (2b), but the time integration was replaced by the following:

$$\hat{U}^{(0)} = \hat{U}^n \tag{3a}$$

$$\hat{U}^{(i)} = \hat{U}^{(0)} - \beta_i \Delta t R^{(i-1)}, \quad i = 1,2,...,p \tag{3b}$$

$$\hat{U}^{n+1} = \hat{U}^{(p)} \tag{3c}$$

The indices n, p and i indicate the time level, and the order and the stage of the Runge-Kutta method, respectively. As for the coefficients, β_1=0 and the other coefficients β_i were determined from

$$c_i = \prod_{k=2}^{i} \beta_{p-k+2}, \qquad i = 2,...,p \tag{4}$$

The coefficients c_i were computed by considering the amplification factor of the Runge-Kutta scheme, then minimizing the dispersion-relation error. The time steps to be used were determined from the stability as well as the accuracy limits. In the present study, a five-stage Runge-Kutta (p=5) was used, which required two levels of storage and it was at least second-order accurate. When it was used with 7-point spatial stencil, the CFL limit from the stability was found to be 3.05, but it was only 1.16 from the accuracy limit. Since, however, this still was larger than the CFL limit of the DRP time integration (0.19), this method was also more efficient in processing time.

Boundary Conditions

The boundaries should be transparent to the acoustic disturbances reaching them to avoid any degradation of the numerical solution. For a right-moving uniform mean flow as represented by the linearized equations, and when all the disturbances (acoustic, entropy and vorticity) are generated in the interior of the domain, only acoustic waves reach the upper, lower and upstream boundaries; but, in addition to the acoustic waves, entropy and vorticity waves can reach the downstream boundary. Therefore, following Tam and Webb (1993) and from the asymptotic solutions of the finite difference form of eq. (1), a set of *radiation* boundary conditions,

$$\frac{\partial \hat{U}}{\partial t} + A\frac{\partial \hat{U}}{\partial \xi} + B\frac{\partial \hat{U}}{\partial \eta} + C\hat{U} = 0 \tag{5a}$$

where

$$A \equiv V\frac{x\xi_x + y\xi_y}{r}, \quad B \equiv V\frac{x\eta_x + y\eta_y}{r}, \quad C \equiv \frac{V}{2r}, \tag{5b}$$

$$r = \frac{1}{\Delta x}\sqrt{x^2 + y^2}, \quad V = \frac{x}{r}M + \sqrt{1 - (M\frac{y}{r})^2}, \tag{5c}$$

and *outflow* boundary conditions for the downstream boundary,

$$\frac{\partial U'}{\partial t} + \hat{M}(U') = Q, \tag{6a}$$

where the Mach-number-related operator and the source term were,

$$\hat{M} = (u_0\xi_x + v_0\xi_y)\frac{\partial}{\partial \xi} + (u_0\eta_x + v_0\eta_y)\frac{\partial}{\partial \eta} \tag{6b}$$

$$Q = \left[\frac{\partial p}{\partial t} + \hat{M}(p), \quad -(\xi_x\frac{\partial p}{\partial \xi} + \eta_x\frac{\partial p}{\partial \eta}), \quad -(\xi_y\frac{\partial p}{\partial \xi} + \eta_y\frac{\partial p}{\partial \eta})\right]^T \tag{6c}$$

were obtained. In eq. (6), U' contains only the first three components of $\hat{U}$ in Eq. (1c). The pressure was obtained as in eq. (5).

For the inviscid calculations on a *solid wall*, the impermeability condition requires that the normal contravariant velocity be zero; and for the viscous computations, the no-slip condition requires that the tangential contravariant velocity also be set to zero.

$$\hat{v} = \eta_x u + \eta_y v = 0., \quad \hat{u} = \xi_x u + \xi_y v = 0 \tag{7}$$

When above equations were used in the η-momentum and ξ-momentum equations, the wall values of pressure and shear stress were obtained, respectively. The DRP scheme coefficients for all the boundary conditions (Tam and Dong, 1994) were derived by an analogous method to that of the boundary region cells.

Results

The present schemes and their boundary conditions were evaluated by considering five wave propagation cases: (i) Single acoustic pulse; (ii) Two simultaneous acoustic pulses; (iii) Acoustic pulse near a flat wall; (iv) Acoustic pulse near a circular cylinder; (v) Periodic source near a flat wall; (vi) Periodic source near a flat wall with a circular bump.

Each of the acoustic pulses, introduced into a uniform mean flow (left to right) with a Mach number of 0.5, was generated by setting u=v=0, and imposing an initial Gaussian distribution for the pressure and density:

$$p = \hat{p}\exp\{-\ln 2\,[\frac{(x-x_s)^2 + (y-y_s)^2}{b^2}]\} \tag{8}$$

For the cases (i)-(iv), $\hat{p} = 0.01, b = 3\Delta x$, x_s=y_s=0. The pressure contours at 1500 Δt for the *single acoustic pulse* case, computed by the fourth order inviscid DRP scheme (eq. 2), are shown in Fig. 1a. The results verified the expected propagation pattern and matched the exact solution (Vanel and Baysal, 1995): the radius of the acoustic wave expanded in time while its center was being entrained downstream with the mean flow. The waves exited from boundaries without any numerical reflections. Presented in Fig. 1b is the same case computed using the optimized Runge-Kutta time integration (eq. 3) after only 150 time steps. The numerical waves matched in both the amplitude and the propagation speed. However, the latter required about *one-half* the storage memory and *one-sixth* the processing time of the former.

In the second case, *two acoustic pulses* were generated *simultaneously:* one at half-span and the other at three-quarter span of the computational domain. Presented in Fig. 2a are the pressure contours computed by the fourth-order DRP scheme

with $\varepsilon=\pi/2$ and without a mean flow (M=0). It was observed that the two pulses intersected as they propagated radially. The interaction of the waves was crisply simulated. Then, the case was repeated with a mean flow of M=0.5 and ε=1.1 (Fig. 2b). With the mean flow, the waves started to drift downstream. Then, the case was repeated using the sixth-order scheme (Figs. 2c, 2d). In all of the above cases minor reflections from the corners were observed. This was cured when the simulation was repeated on a four times larger domain (Figs. 2e, 2f).

To test the wall boundary condition, the lower boundary was replaced by a solid flat wall. The reflection of the pulse off the wall and its interference with the incident pulse were computed once by solving the Euler equations (Fig. 3), then by solving the Navier-Stokes equations (Fig. 4). As expected, the wave strength was attenuated faster in the latter due to the physical diffusion process.

Then, the case of circular cylinder, with the pulse at (4, 0) with $\hat{p}=1.0, b=0.2$, was simulated on a relatively coarse but conforming grid (251x101). The motivation was the physical problem of the sound field generated by a propeller scattered off by the fuselage of an aircraft. The pressure loading on the fuselage was an input to the interior noise problem. Here, the fuselage was idealized as a circular cylinder and the noise source as a line source, hence a 2-D problem. Four instants from the animation of the acoustic scattering are presented in Fig. 5.

In the *periodic acoustic source* cases, the source was generated with the fourth term in the source vector of eq. (1),

$$S_4 = \hat{s}\exp\{-\ln 2\,[\frac{(x(\xi,\eta)-x_s)^2+(y(\xi,\eta)-y_s)^2}{b^2}]\}\sin(\omega t) \quad (9)$$

where b=3, and $(x_s,y_s,)=(0,20)$. The medium was inviscid air at M=0. The interference pattern, shown in Fig. 6 is for the source with $\hat{s}=0.001$ near the flat wall, and after the computations reached the limiting cycle. Then, the periodic source with $\hat{s}=0.01$ was placed above a circular bump on a flat plate at (0, 20). The interference pattern is presented in Fig. 7.

By and large, the reflections and scattering computations were successful. By employing the body-fitted coordinates, solid wall boundary conditions were imposed properly, hence the wall region was properly computed. On the other hand, grid cells not being perfectly orthogonal, and the existence of the transformation metrics in the equations, caused minor degradation, as compared to the Cartesian cases.

Conclusions

Computational schemes which preserve the dispersion relation of the fundamental equations were investigated. In developing such schemes, ultimately for realistic and complex aeroacoustics problems, several necessary steps have been taken. The linearized Euler and Navier-Stokes equations were solved. Solid wall boundary conditions and differences utilizing the nearest-point information in the boundary regions were demonstrated. The spatial scheme was extended to the sixtth order accuracy, and with the optimized Runge-Kutta time-integration, the efficiency of the method was improved. For the curved wall boundary conditions, the scheme was extended for the generalized curvilinear coordinates. The schemes were successfully demonstrated for several acoustic pulse cases and several acoustic scattering cases.

In order for the scheme to be of more practical interest, it was deemed necessary to investigate its further extensions for the nonlinear equations, with a controllable amount of numerical dissipation, and multiblock nonuniform grids. Also, both from the efficiency and the accuracy points of view, replacing the present finite-difference (local) boundary conditions with integral (global) boundary conditions should prove to be profitable.

References

Baysal, O., Yen, G.W., and Fouladi, K., 1992, "Navier-Stokes Computations of Cavity Aeroacoustics With Suppression Devices," *Proceedings of DGLR/AIAA 14th Aeroacoustics Conference*, Vol. 2, pp. 940-948, Aachen, Germany. Also, *Journal of Vibration and Acoustics*, Vol. 116, No. 1, pp. 105-112.

Hardin, J.C., Ristorcelli, J.R., Tam, C.K.W., (Editors), 1995, ICASE/LaRC Workshop on Benchmark Problems in Computational Aeroacoustics, NASA Conference Publication 3300.

Hu, F.Q., Hussaini, M.Y., and Manthey, J., 1994, "Low-dissipation and Low-dispersion Runge-Kutta Schemes for Computational Acoustics," ICASE Report 94-102, Hampton, VA. Also to appear in *Journal of Computational Physics*, March 1996.

Lighthill, J., (1992), "Report on the Final Panel Discussion on Computational Aeroacoustics," ICASE Report No. 92-53, NASA Langley Research Center, Hampton, VA.

Lyrintzis, A. S., Mankbadi, R.R., Baysal, O., Ikegawa, M., (Editors), 1995, Computational Aeroacoustics, FED-Vol. 219, ASME, New-York, NY.

Mankbadi, R.R., Lyrintzis, A. S., Baysal, O., Povinelli, L. A., Hussaini, M. Y., (Editors), 1993, Computational Aero- and Hydro-acoustics, FED-Vol. 147, ASME, New-York, NY.

Tam, K. W., and Webb, J. C., 1993, "Dispersion-Relation-Preserving Finite Difference Schemes for Computational Acoustics," *Journal of Computational Physics*, Vol. 107, pp. 262-283.

Tam, C.K.W., and Shen, H., 1993, "Direct Computation of Nonlinear Acoustic Pulses using Higher-Order Finite Difference Schemes," AIAA Paper 93-4325, 15th Aeroacoustics Conference, Long Beach, CA.

Tam, C.K.W., and Dong, Z., 1994 "Wall Boundary Conditions for High-Order Finite Difference Schemes in Computational Aeroacoustics," AIAA Paper 94-0457, 32nd Aerospace Sciences Meeting, Reno, NV.

Vanel, F. O., and Baysal, O., 1995, "Investigation of Dispersion-Relation-Preserving Scheme and Spectral Analysis Methods for Acoustic Waves," Paper no. 95-093, Proceedings of First CEAS/AIAA Aeroacoustics Conference, Munich, Germany, pp. 675-682. Also, to appear in [ASME] *Journal of Vibration and Acoustics*,

Acknowledgment

This work was supported by NASA Langley Research Center Grant NAG-1-1653. The technical monitor was Dr. J.L. Thomas.

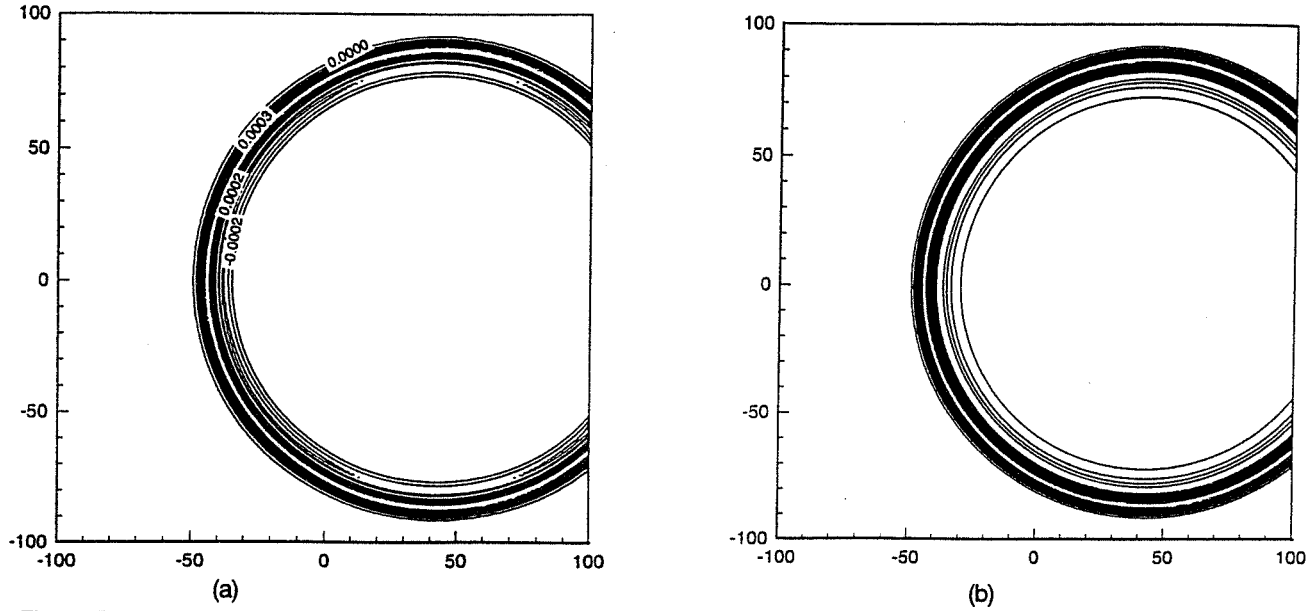

Fig. 1 Pressure contours of an acoustic pulse (eq. 8) after 1500 Δt computed with: (a) four-level DRP time integration, (b) optimized five-stage Runge-Kutta.

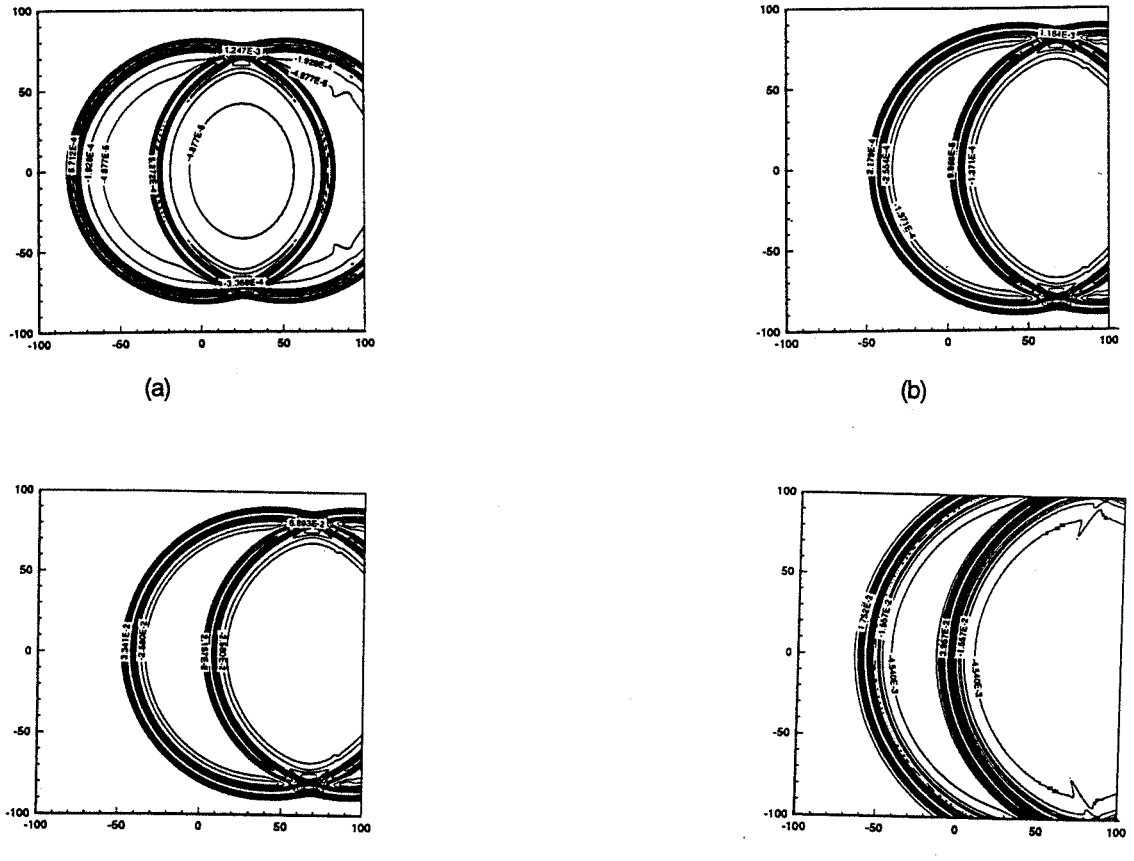

Fig. 2 Pressure contours of multiple acoustic pulses (eq. 8 at two locations). (a) M=0 case at 1000 Δt;(b) ε=1.1 case at 1500 Δt; Sixth-order scheme at (c) 1500 Δt and (d) 2000 Δt; On 400x400 domain at (e) 1000 Δt and (f) 2000 Δt.

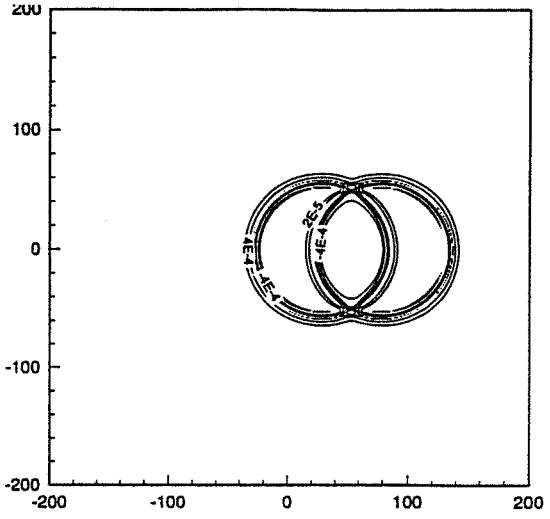

(e)

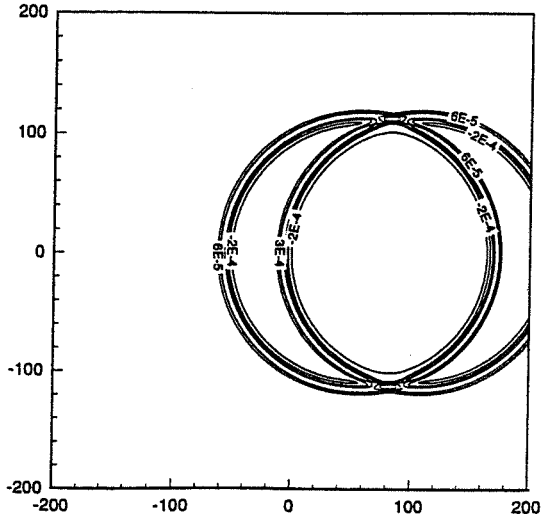

(f)

Fig. 2 (Concluded)

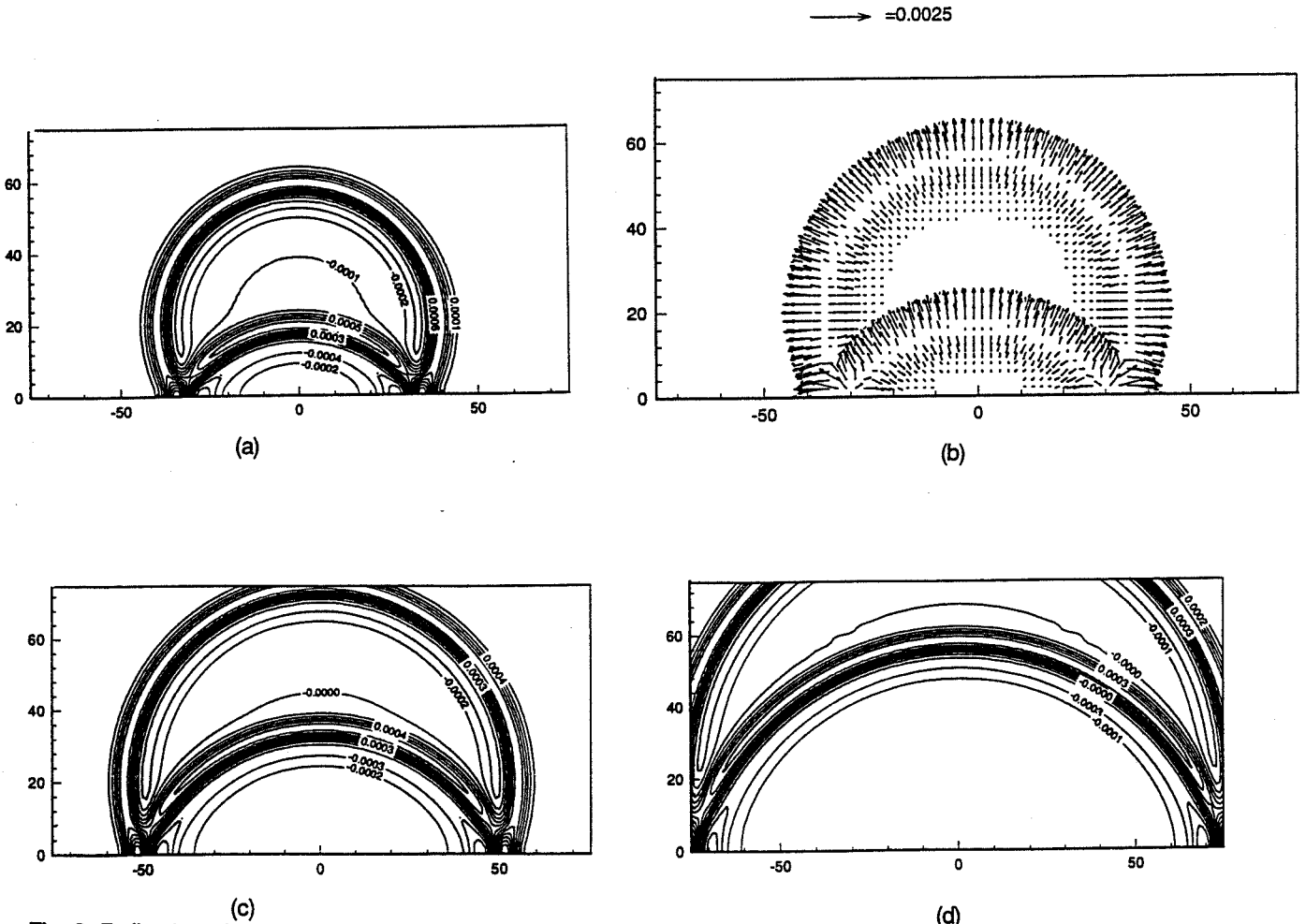

Fig. 3 Reflection of an acoustic pulse (eq. 8) from a flat wall by solving Euler equations. Pressure contours at: (a) 500 Δt, (c) 700 Δt, (d) 1000 Δt. (b) Velocity vectors at 500 Δt.

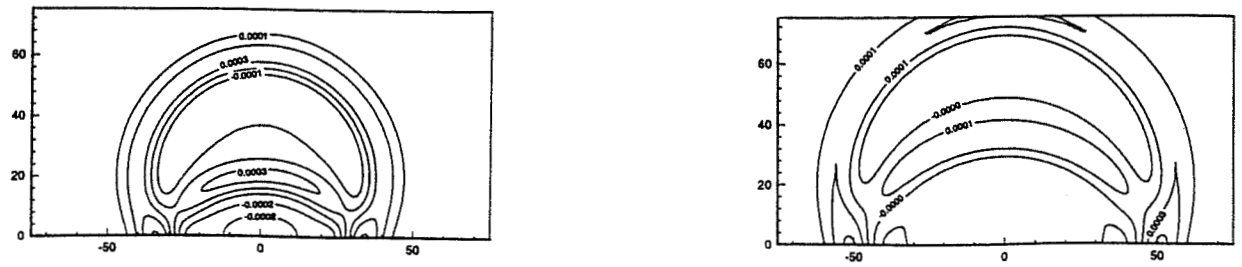

(a) (b)

Fig. 4 Reflection of an acoustic pulse (eq. 8) from a flat wall by solving Navier-Stokes equations.
Pressure contours at: (a) 500 Δt, (b) 700 Δt.

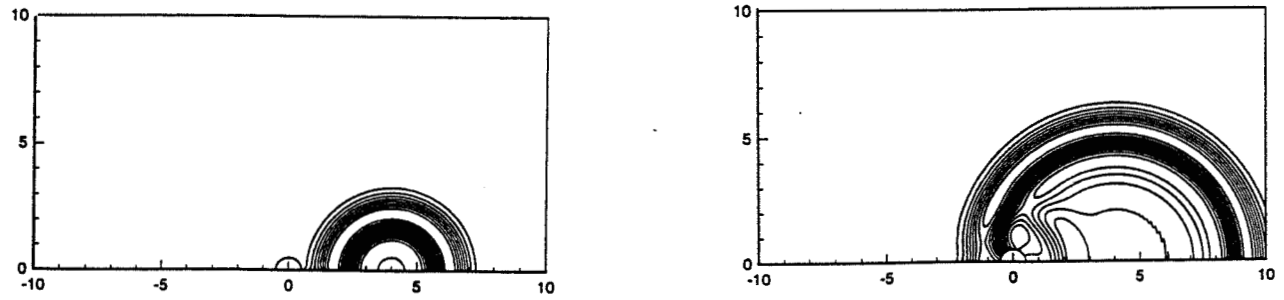

(a) (b)

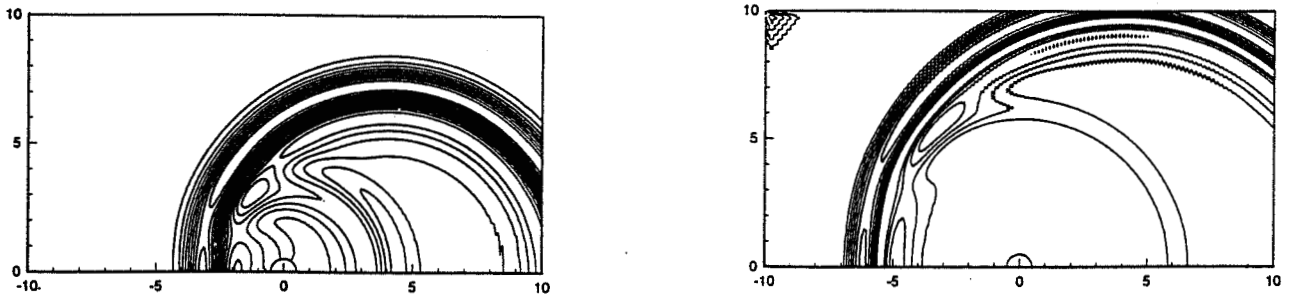

(c) (d)

Fig. 5 Scattering of an acoustic pulse (eq. 8 with source at (4,0)) from a circular cylinder.
Pressure contours at: (a) t=2., (b) t=5., (c)t=7., (d) t=10. Δt=1.0E-2.

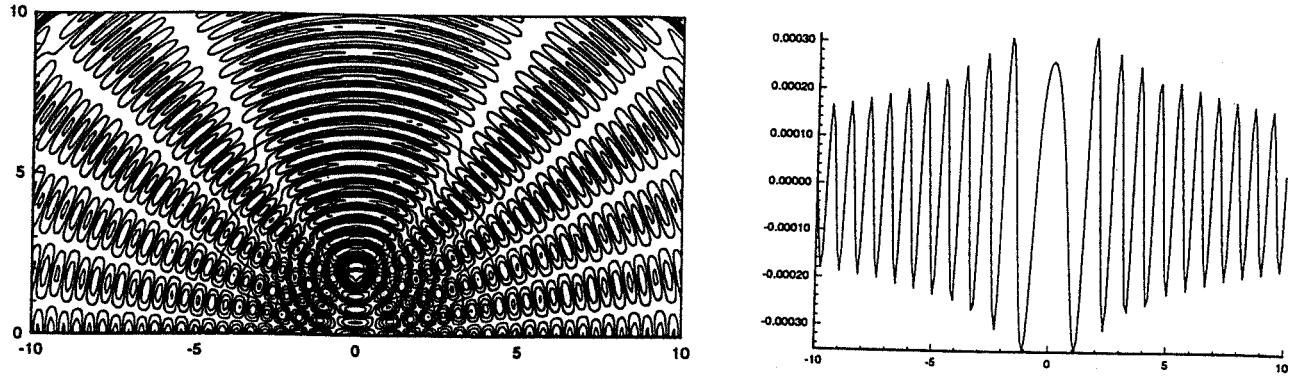

(a) (b)

Fig. 6 Interference pattern of a periodic acoustic source (eq. 9) reflected from a flat wall: (a) pressure contours, (b) wall pressure values.

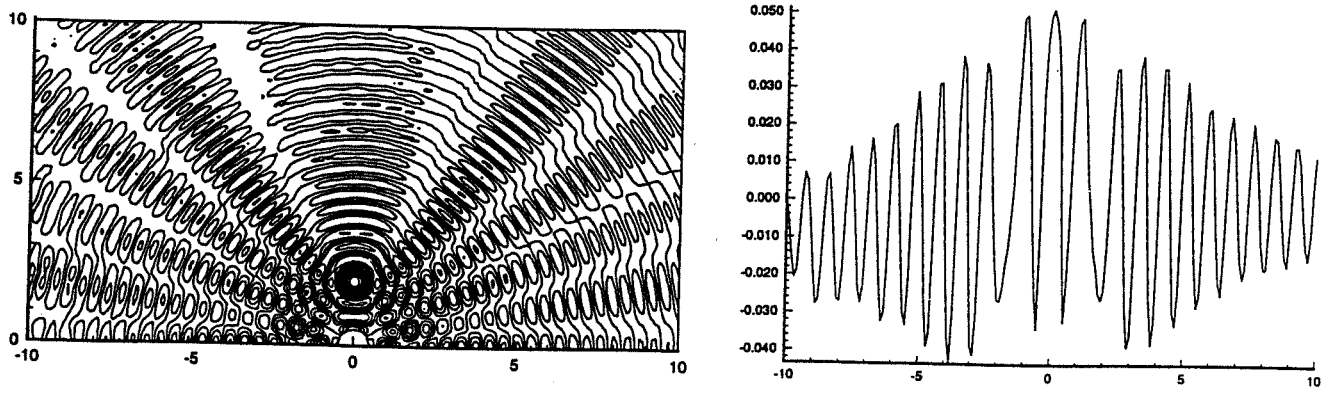

(a) (b)

Fig. 7 Interference pattern of a periodic acoustic source (eq. 10) from a bump on a flat wall: (a) pressure contours, (b) wall pressure values.

AIAA-97-2107

The Accuracy of Shock Capturing In Two Spatial Dimensions

Mark H. Carpenter

NASA Langley Research Center
Hampton, VA

Jay H. Casper

Old Dominion University
Norfolk, VA

13th Computational Fluid Dynamics Conference

June 29--July 2, 1997 / Snowmass, CO

THE ACCURACY OF SHOCK CAPTURING IN TWO SPATIAL DIMENSIONS

Mark H. Carpenter *, Jay H. Casper †

Abstract

An assessment of the accuracy of shock capturing schemes is made for two-dimensional steady flow around a cylindrical projectile. Both a linear fourth-order method and a nonlinear third-order method are used in this study. It is shown, contrary to conventional wisdom, that captured two-dimensional shocks are asymptotically first-order, regardless of the design accuracy of the numerical method. The practical implications of this finding are discussed in the context of the efficacy of high-order numerical methods for discontinuous flows.

Introduction

High-order schemes (schemes of second-order accuracy or higher) have been used effectively to capture shocks for at least thirty years [1]. There is little doubt of their virtues when compared with first-order schemes. For this reason, second- and higher-order schemes have almost universally replaced first-order schemes throughout computational fluid dynamics. Only recently, however, has a critical analysis of the actual error of higher-order schemes been undertaken. In a previous work by Casper and Carpenter [2] it is shown that time dependent shocks can only be captured with first-order accuracy, regardless of the design order of the numerical method. Figure 1 shows the pointwise error from a sound-shock interaction problem, using a fourth-order nonlinear ENO algorithm to solve the time-dependent Euler equations. Figure 2 shows the same problem resolved using a sixth-order linear finite difference algorithm. Both algorithms converge at a first-order rate, downstream of the shock. This degradation in accuracy is caused by the inability of conventional numerical methods to pass information through a discontinuity.

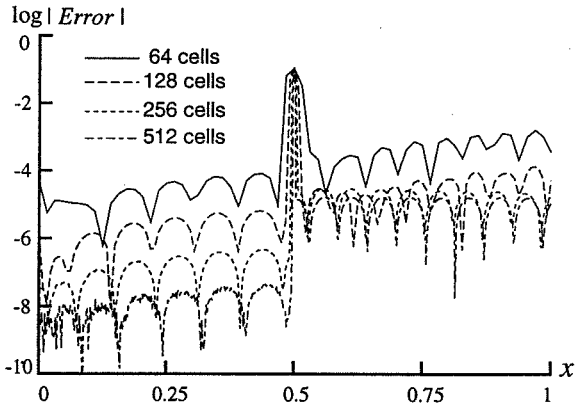

Figure 1. *Pointwise error for the 1-D sound-shock interaction problem as obtained using the nonlinear ENO-4-3 numerical scheme.*

In a companion work [3], these results are reaffirmed and quantified for a broader class of problems. Specifically, a sixth-order-accurate compact implicit finite difference scheme and a fourth-order accurate ENO scheme are used to investigate various discontinuous flows. The design order of accuracy is achieved in the smooth regions of a steady-state, quasi-one-dimensional Euler test case, as well as in the time-dependent Burgers' equation. However, in an unsteady Euler sound-shock interaction problem, first-order results are obtained downstream of the shock. A discontinuous linear model problem identifies the cause of the first-order results, and quantifies the error as being predominantly a numerical phase shift resulting from information passing through the discontinuity. Post-processing the first-order data, increases the solution accuracy downstream of the discontinuity to second-order, although high-order is still not attainable.

One can readily extend the negative results found in 1-D to multiple spatial dimensions. Specifically, that time-dependent shocks are inherently first-order accurate in any number of spatial dimensions. The 1-D **steady** Euler equations exhibit design accuracy away from discontinuities. There is, therefore, the possibility that the steady-state discontinuous Euler equations will admit higher-order solutions in multiple dimensions. In this work we

*Aerospace Engineer, Aerodynamic and Acoustic Methods Branch, NASA Langley Research Center, Hampton, VA 23681.

†Old Dominion University, Norfolk, Virginia

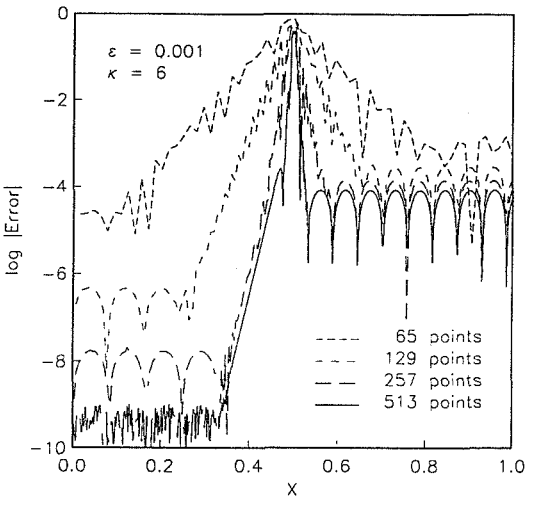

Figure 2. *Pointwise error for the 1-D sound-shock interaction problem as obtained using linear LIN-6-4 numerical scheme.*

quantify the solution accuracy for the steady-state 2-D Euler equations. We show that, unlike the 1-D case, the 2-D Euler equations are first-order accurate downstream of a shock at steady-state, **regardless** of the design accuracy of the numerical method.

In section 2, we present the Euler Equations in two spatial dimensions. The equations are used to solve for the inviscid flow around a supersonic blunt body. In section 3, we describe the numerical methods used on the test problems. Three different numerical methods are used to solve for the flow around a supersonic blunt-body. A Chebyshev bow-shock fitting algorithm is used to obtain an "exact solution" to the problem. A linear fourth-order finite difference algorithm, and a nonlinear third-order ENO numerical algorithm are used to capture the solution around the blunt-body. In section 4, we present a comparative study between the three methods. We show that all captured solutions are first-order on sufficiently fine meshes, regardless of the design accuracy of the spatial operator. In Section 5, we study the influence of Mach number, and the effects of design accuracy on the first-order results. Section 6 concludes the work.

Governing Equations

We focus in this work on the two dimensional Euler equations. In the physical coordinates the equations are:

$$\frac{\partial \mathbf{U}}{\partial t} + \frac{\partial \mathbf{F}}{\partial x} + \frac{\partial \mathbf{G}}{\partial y} = 0 \qquad (1)$$

where

$$\mathbf{U} = \begin{bmatrix} \rho \\ \rho u \\ \rho v \\ \rho E \end{bmatrix}, \quad \mathbf{F} = \begin{bmatrix} \rho u \\ \rho u^2 + P \\ \rho uv \\ (\rho E + P)u \end{bmatrix}, \quad \mathbf{G} = \begin{bmatrix} \rho v \\ \rho vu \\ \rho v^2 + P \\ (\rho E + P)v \end{bmatrix}$$

The variables ρ, u, v, P, E, are the density, x-velocity, y-velocity, pressure, and total specific energy, respectively. The equation of state is

$$P = (\gamma - 1)\,\rho\,[E - \frac{1}{2}(u^2 + v^2)]$$

where γ is the ratio of specific heats, which is assumed to have a constant value of 1.4.

Numerical Methods

We use three different numerical methods to study the 2-D blunt body problem. A Chebyshev shock fitting algorithm is used to generate an "exact" solution around a supersonic cylindrical projectile. Both a linear fourth-order and a nonlinear third-order ENO shock capturing algorithm are then used to capture the solution around the cylindrical body. Accuracies are assessed by comparing the captured solutions with the exact solution. All three of these algorithms are fairly routine, and have been documented extensively in the literature. We include only a brief description of each algorithm, noting the specific details necessary to maintain robustness on the blunt body problem.

When dealing with negative results, one must be wary of the generality of the test problems, and of the numerical algorithms. The two capturing algorithms represent extremes from the spectrum of higher-order formulations presently in use. It is hoped that this diversity adds credibility to the negative results obtained in this study.

Chebyshev Shock Fitting

A Chebyshev bow-shock fitting algorithm is used to determine a very accurate numerical solution to the blunt body problem. Figure 3 shows a numerical grid wrapping around the forebody of a two-dimensional circular cylinder. A Chebyshev spatial operator is used in both the radial and the circumferential directions to resolve the inviscid flow around the cylinder. Note that the grid line furthest from the body coincides exactly with the curved bow-shock.

The fitted solution is obtained by first mapping the Euler equations in space and time into the computational space. A linear mapping from (r,θ,t) $\rightarrow$ (ξ, η, τ) is used:

$$\xi = \frac{r - r_b(\theta)}{r_s(\theta, t) - r_b(\theta)}$$

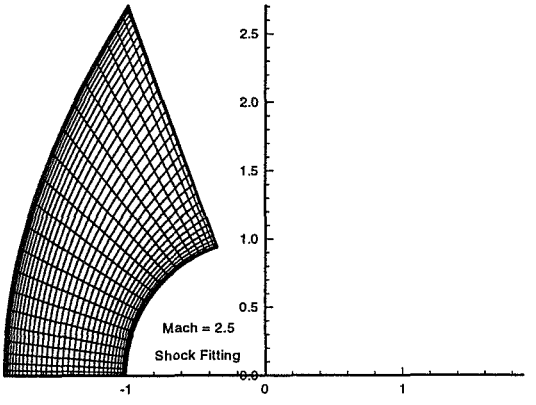

Figure 3. *Shock-fit Chebyshev spectral grid for the Mach = 2.5 blunt-body flow.*

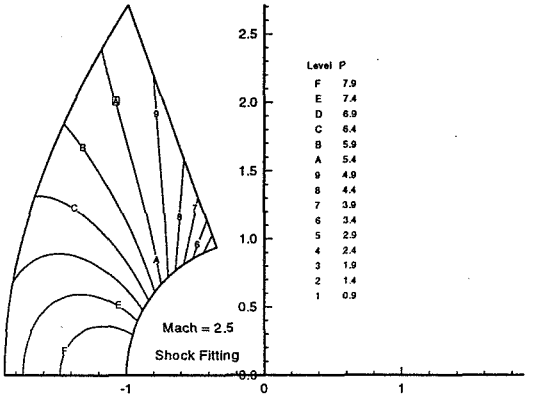

Figure 4. *Pressure profiles of the "exact" solution obtained with the Chebyshev shock fitting algorithm.*

$$\eta = \frac{\theta - \theta_{min}}{\theta_{max} - \theta_{min}} \qquad (2)$$
$$\tau = t$$

where r_b, r_s, θ_{min}, and θ_{max} , are the radius of the body, and shock, and the minimum and maximum values of θ, respectively. The shock position always coincides with the line $\xi = 1$, and the physical domain changes continuously as the bow-shock moves to its steady state position. Because of symmetry along the body centerline, only half of the problem is solved. The Chebyshev collocation technique is used in the computational domain to discretize the resulting set of equations. The equations are then marched in time until a steady state solution is reached.

A crucial element of the procedure is the treatment of the boundary conditions, and in particular the movement of the shock. To move the shock, a shock velocity equation is derived by differentiating the Rankine-Hugoniot relations at the shock. The resulting differential equations for the position and velocity of the shock are then advanced in time with a five stage Runge-Kutta scheme along with the rest of the discrete equations. Symmetry conditions are imposed along the center line, and inviscid wall conditions are imposed at the body. At the outflow, the flow is supersonic normal to the boundary and no physical boundary conditions are imposed. Further details on the boundary treatments can be found elsewhere [4, 6].

The grid used in the Mach = 2.5 case (see Figure 3), contains 36 radial and 24 circumferential collocation points. This grid density is sufficient to predict a stagnation pressure on the centerline exact to twelve significant digits. The solutions accuracy throughout the domain is monitored using the spectral decay of polynomial coefficients. The worst portion of the flow is resolved to eight orders of magnitude. This solution (referred to from now on as the "exact" solution) is spectrally interpolated to a sequence of uniformly spaced grids for use as error indicators in the finite difference algorithm. Figures 4, 5 and 6 show the pressure, density and velocity vector profiles of the blunt-body flow. Note the smooth, well resolved contour lines.

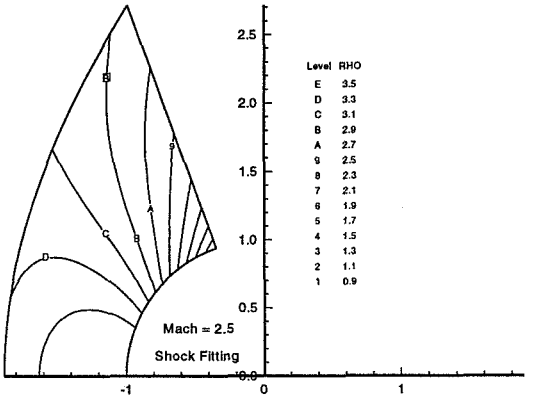

Figure 5. *Density profiles of the "exact" solution obtained with the Chebyshev shock fitting algorithm.*

Fourth-Order Linear Scheme

Conventional high-order central difference discretizations lack the robustness necessary to efficiently converge this problem to steady-state. A

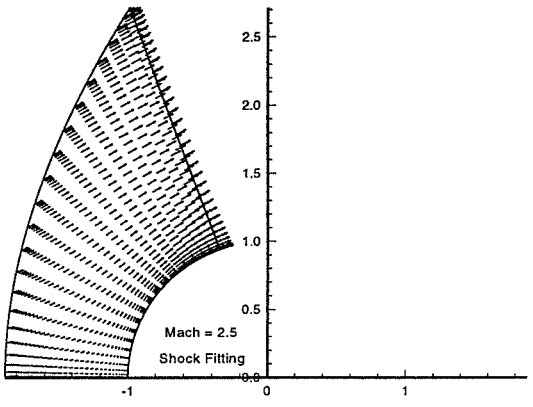

Figure 6. *Velocity vectors from the "exact" solution obtained with the Chebyshev shock fitting algorithm.*

fourth-order upwind biased algorithm, however, proves robust and efficient over the Mach number range consider in this study. The upwinding uses a Lax-Friedrichs splitting of the flux vector. Specifically, the derivative of the contravariant flux $\hat{F}$ is calculated as:

$$D\hat{F} = \frac{1}{2}(D^+\hat{F}^+ + D^-\hat{F}^-)$$

where $\hat{F}^{\pm} = \hat{F} \pm \lambda_{max}\hat{U}$, and $D^+ = (3,3,3-4-3)$, $D^- = (3-4-3,3,3)$. (The nomenclature for derivative closure D^+ denotes that the left three points are treated third-order, the interior is fourth-order and the right point is third-order. Details of the nomenclature can be found elsewhere [5].) The fourth-order D^+ operator is the upwind biased stencil:

$$U(x_i) = \sum_{j=i-3}^{i+1} a_{i,j}\, U(x_j) \quad + O\,(\delta x)^4$$

where row i of the matrix $\mathbf{a_{i,j}}$ is defined as $\mathbf{a_{i,j}} = \frac{\mathbf{1}}{\mathbf{12\delta x}}[\mathbf{-1,6,-18,10,3}]$. The third-order stencils used at all boundary points are the optimal stencils derived from nearest neighbor information, biased where possible in an upwind direction. The scaling parameter λ_{max} is the maximum over the entire domain of the contravariant eigenvalue $\hat{u}+\hat{c}$. A similar expression is used for the $\hat{G}$ vector.

Historically, finite-difference formulations that locate a discrete point at the stagnation point are susceptible to numerical instability. Careful implementation of the boundary conditions eliminates this problem. The present formulation is as robust as the staggered formulations typically adopted by finite-difference algorithms near stagnation points. On the inflow plane all variables are prescribed, consistent with supersonic inflow. On the outflow, the solution is simply calculated using one-sided high-order information, and no boundary conditions are imposed. On the symmetry plane, the v component of the velocity is set to zero. On the inviscid wall, the no penetration boundary condition is treated weakly through the flux. Specifically, the contravariant flux on the wall is calculated consistent with the no-penetration condition. (The normal velocity is flipped in sign, to create a reflecting state. The two states are then rectified with a Riemann solver to obtain a state with no normal velocity). The physical velocity at the wall is not required to satisfy the no penetration condition. Thus, at steady state, the normal velocity at the wall is nonzero, but converges to zero with an order property consistent with the overall formulation.

A three stage Runge-Kutta is used to drive the solution to steady-state. The calculations are suspended when the solution error based on the exact solution converges to four significant places.

Third-Order Nonlinear Scheme

The third numerical scheme employed in this work is a third-order accurate ENO algorithm. Spatial accuracy is achieved by solving the two-dimensional, time-dependent Euler equations in control-volume form. Complete details of the algorithm are presented elsewhere [7]. The adaptive stencils employed in the high-order spatial operator are biased in smooth regions toward those that are linearly stable (See, e.g. [8]). All required mesh quantities (cell areas, grid metrics, etc.) are calculated to consistent accuracy [7]. The solution is advanced in time, towards a steady state, via a three-stage Runge-Kutta scheme [9]. Implicit residual smoothing is employed in order to accelerate the time integration.

Fluxes at cell interfaces are approximated in two distinct ways. The most accurate treatment is by Roe's approximate Riemann solver, as presented in Reference 10. Full machine-zero convergence to steady state is not possible with this formulation. High-order accuracy is nonetheless attained on the grid aligned test case. The robustness and generality of the formulation is somewhat questionable, making it necessary to use a second formulation. To drive residuals to machine zero, it is necessary to augment the Roe solver with an entropy fix [11], and to more heavily bias the stencils. These modifications give rise to an oscillation near the shock, and cause the solution error to revert to first-order accuracy. We use the straight Roe solver as a means of verifying the accuracy of the algorithm, and the

second formulation as the general solver used in the comparative studies.

Grids

The grids used for all calculations originate from the Chebyshev spectral solution. A uniform discretization in both the radial and circumferential directions is used. To accomplish shock capturing, the grid is extended in the radial direction until exactly one quarter of the points are in the supersonic portion of the flow. The following sequence of grids is used to perform a grid refinement study: 33x33, 65x65, 129x129, 257x257, 513x513. The exact solution is projected onto these grids (using spectral interpolation) for use as the initial condition, and to calculate solution accuracies.

Results

First-Order motivation

We begin by presenting a heuristic argument explaining why the 2-D steady-state Euler equations admit first-order solutions downstream of two-dimensional discontinuities. We saw in previous works [2], [3] that time dependent information passing though a discontinuity is corrupted to first-order by a discontinuity. This statement was quantified using the model problem $u_t + [a(x)u]_x = 0$ with a(x) discontinuous. It was concluded that first-order corruption occurs in hyperbolic equations when $a(x)$ is discontinuous and information passes through the discontinuity.

We now show that at least part of the steady-state 2-D Euler equations are mathematically equivalent to the model hyperbolic problem, with the wave speed $a(x)$ being discontinuous at the captured shock. (Here the second spatial dimension takes the place of time, resulting in a hyperbolic equation in [x,y]). Therefore, based on the 1-D time-dependent results, the discontinuous 2-D Euler equations will exhibit first-order error downstream of an arbitrary captured discontinuity.

The equations governing the steady-state Euler equations in 2-D are

$$\frac{\partial \mathbf{F}}{\partial x} + \frac{\partial \mathbf{G}}{\partial y} = \mathbf{A}\frac{\partial \mathbf{U}}{\partial \mathbf{x}} + \mathbf{B}\frac{\partial \mathbf{U}}{\partial \mathbf{y}} = \mathbf{0} \qquad (3)$$

where $\mathbf{A} = \frac{\partial \mathbf{F}}{\partial \mathbf{U}}$ and $\mathbf{B} = \frac{\partial \mathbf{G}}{\partial \mathbf{U}}$. The mathematical charactor of equation (3) is governed by the eigenvalues of the matrix $\mathbf{M} = \mathbf{A^{-1}}\,\mathbf{B}$. The eigenvalues of the matrix M are $\lambda_{1,2} = \frac{v}{u}$, $\lambda_{3,4} = \frac{uv \pm a\sqrt{u^2+v^2-a^2}}{u^2-a^2}$. For supersonic flow the eigenvalues are real and distinct, and the equation set is strictly hyperbolic. For subsonic flow, two of the eigenvalues are real and two are imaginary and the equation set is mixed elliptic-hyperbolic. The two eigenvalues that are real independent of the Mach number are $\lambda_{1,2} = \frac{v}{u}$, and correspond to the advection of information along the streamlines $\frac{v}{u}$. The mathematical character of the hyperbolic portion of the equation is identical to that exhibited in the unsteady 1-D equation $u_t + [a(x)u]_x = 0$ with a(x) discontinuous. Thus, the steady 2-D Euler equations will be first-order downstream of any captured discontinuity.

We digress here and note that the multidimensional accuracy at steady state is different from that found in the 1-D case. The 1-D steady state solution is design order away from any discontinuities, while the 2-D case is first-order behind general discontinuities. We provide no mathematical explanation for this anomaly other than to say that two "dimensions" are necessary to exhibit the first-order behavior.

The Smooth "Near-Body" Problem

A model problem is needed to test the accuracy of the shock capturing algorithms. Different formulations of the exact solution are used to test the linear and non-linear algorithms. We begin by describing the testing of the linear algorithm.

By solving for the flow between the bow-shock and the cylinder (the near-body), we test the centerline, wall and outflow boundary conditions, as well as the design accuracy of the method. Since there are no discontinuities in this subproblem, the linear formulation should recover design accuracy. Eliminating the gridpoints outside the bow-shock, a subsequence of grids is formed having 25x33, 49x65, 97x129, 193x257, and 385x513 points respectively. The boundary conditions for the centerline, wall and outflow planes are identical to those described previously. The subsonic inflow boundary condition at the bow-shock is implemented by solving the Riemann problem between the numerical state at the point and the exact post-shock conditions from the spectral algorithm.

Table Ia. shows the results of a grid refinement study using the linear fourth-order scheme for a Mach number of $M = 2.5$. Reported are the L_2 error in density, and the L_2 error in the normal velocity component at the inviscid wall, both as a function of grid. The L_2 error is defined as $L_2 = \sqrt{\frac{\sum_i^N (\psi_i - \psi_i^{ex})^2}{N}}$, where ψ_i and ψ_i^{ex} are the numerical and exact values of the respective functions at point i, and N is the number of points in the norm. The norm of density is formed over the

entire domain. (The norm of wall-normal velocity is formed over all body points).

	Density	4^{th}	Wall BC	4^{th}
Grid	$\log L_2$	Rate	$\log L_2$	Rate
25x33	-3.275		-3.119	
49x65	-4.230	3.17	-4.003	2.94
97x129	-5.256	3.41	-4.980	3.25
193x257	-6.330	3.57	-6.041	3.52
385x513	-7.419	3.62	-7.163	3.73

Table Ia: *Smooth test case of near wall region showing design accuracy of the linear shock capturing scheme.*

The convergence rate is asymptoting to the theoretical value of 4. (The third-order closure near the boundaries dominates the solution accuracy on coarse grids). The normal component of the velocity at the wall is going to zero in accordance with the weak imposition of the tangency condition. Similar convergence behavior is observed for the pressure and for other other norms.

Several specific features of the blunt body, and the ENO formulation, allows for a convincing test of the non-linear formulation. The full grid is constructed with the shock coinciding exactly with an interface in the finite volume formulation. If smooth interpolants are used on either side of the cell interface, and a Riemann solver which satisfies the Rankine-Hugoniot shock jump relations is used, then for this special case, the shock is "fit" at the cell interface. All these constraints are met by the ENO formulation using a Roe flux at the interfaces. As noted earlier, the temporal residual for this test problem would not converge more than four orders of magnitude. In spite of this, design accuracy was achieved on the original sequence of four grid.

Table Ib. shows the results of a grid refinement study using the third-order ENO scheme for a Mach number of $M = 2.5$. Reported is the L_2 error in density, using the same definitions of error reported in the linear case.

	Density	3^{rd}
Grid	$\log L_2$	Rate
33x33	-3.162	
65x65	-4.042	2.92
129x129	-5.007	3.21
257x257	-6.045	3.45

Table Ib: *Special "fitted" test case showing design accuracy of ENO formulation using the straight Roe flux at interfaces.*

The convergence rate is asymptoting to a value greater than the theoretical accuracy of 3. Note in an absolute sense, that the errors from the third-order ENO formulation are comparable with those obtained from the fourth-order linear algorithm. Two dimensional plots of the pressure and density obtained from the ENO algorithm are nearly indistinguishable from the "exact" solutions shown in Figures 4 and 5. Figure 7 shows the pressure profiles obtained with the nonlinear ENO algorithm for this test case. Note the monotone one point bow-shock.

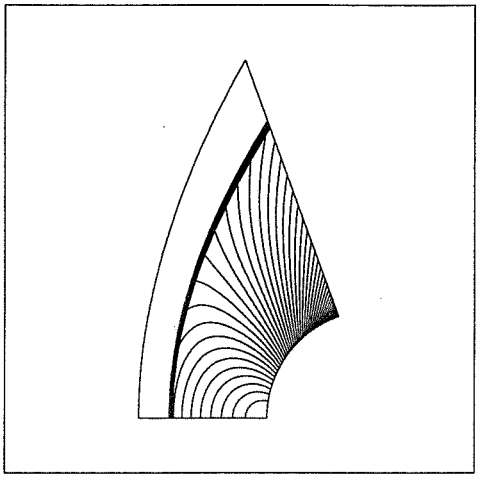

Figure 7. *Density profiles of the captured solution obtained with the third-order ENO method, using only the Roe flux at the interfaces. The solution is third-order accurate.*

Several points can be deduced from these studies. First, the shock capturing algorithms exhibit design accuracy on the near-body subproblem. This indicates that the symmetry, wall and outflow boundaries are correct. Secondly, the agreement to seven significant digits between the capturing algorithm and the Chebyshev spectral solution indicates that the "exact" answer is correct to at least 7 digits.

The Shock-Captured "Blunt-Body" Problem

We now use the validated linear fourth-order and the nonlinear third-order algorithms to capture the bow-shock around a Mach 2.5 circular cylinder. The only modifications necessary to capture the blunt-body shock are, 1) in the linear formulation, the original grids are used, and supersonic free-stream conditions are imposed at the inflow. 2) For the nonlinear ENO formulation the Roe solver at the interfaces is modified with an entropy fix, and the stencil biasing parameters were tuned. These modifications allow a steady-state residual to be driven

to machine precision, but eliminate the possibility of "fitting" the shock at the interface.

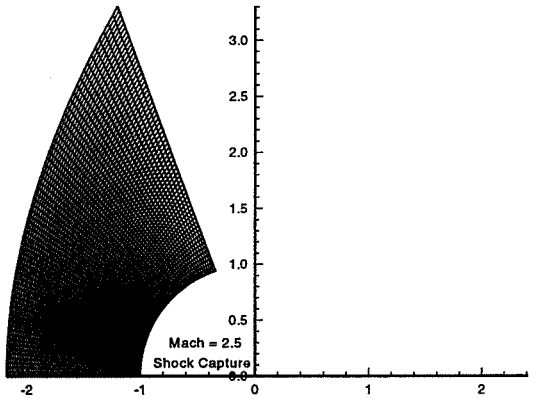

Figure 8. *Finite difference grid employing 65x65 evenly spaced points, used to capture the Mach = 2.5 blunt-body flow.*

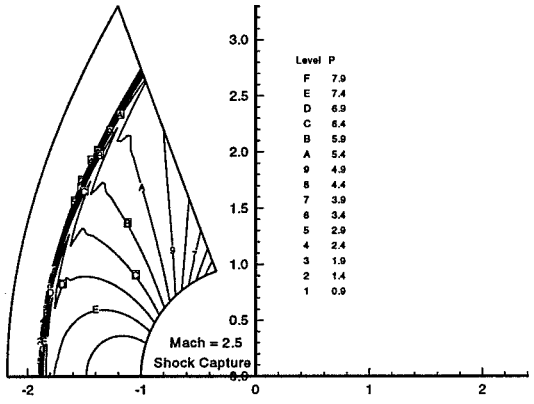

Figure 9. *Pressure profiles of the captured solution obtained with the fourth-order finite difference algorithm.*

Figure 8 shows the 65x65 grid used in both formulations. Figures 9 and 10 show the two-dimensional pressure and density profiles obtained with the linear method. Figure 11 shows the pressure profiles obtained with the nonlinear method. All are obtained on the 65x65 grid. The solution from the linear algorithm has huge oscillations at the captured shock, whereas the nonlinear formulation is nearly monotone.

Refinement studies using the original sequence of grids are presented in Tables IIa and IIb. In table

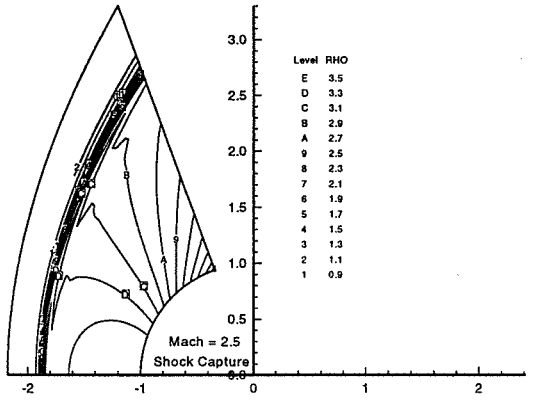

Figure 10. *Density profiles of the captured solution obtained with the fourth-order finite difference algorithm.*

IIa, the L_2 norm of the density and pressure errors are presented, as obtained with the fourth-order linear algorithm. The density and pressure norms are formed using only the half of the domain closest to the body, in order to exclude any points close to the captured shock region.

	Density	4^{th}	Pressure	4^{th}
Grid	$\log L_2$	Rate	$\log L_2$	Rate
33x33	-1.756		-1.651	
65x65	-3.404	5.47	-3.370	5.74
129x129	-3.708	1.01	-3.778	1.32
257x257	-4.014	1.02	-4.117	1.13
513x513	-4.317	1.01	-4.437	1.06

Table IIa: *Captured Mach 2.5 bow-shock around circular cylinder using linear shock capturing scheme.*

In marked contrast to the accuracy of the near-body problem, the 2-D captured shock accuracy is asymptotically **first – order** in space. On coarse grids the scheme converges near the design accuracy, but is dominated by the first-order shock error on finer grids. Note that the density and pressure exhibit nearly identical behavior. We note, but do not show that the wall penetration error is asymptoting to design accuracy, as it did in the near-wall test problem.

In table IIb, the the L_2 norm of the density errors are presented, as obtained with the third-order ENO algorithm. The same error norms are used as in the linear algorithm. The 2-D captured shock accuracy is asymptotically **first – order** in space. The nonlinear formulation yields increased accuracy on coarse grids, but surprisingly is less accurate asymptotically than the fourth-order linear algorithm. Not

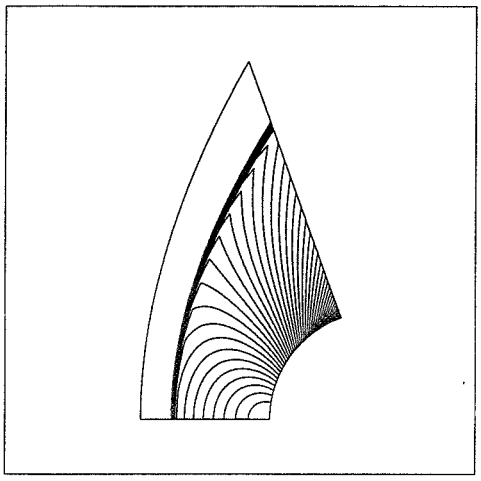

Figure 11. *Density profiles of the captured solution obtained with the third-order ENO algorithm, using the Roe flux with an entropy fix at the interfaces. The solution is first-order accurate.*

surprisingly, there is no component of high-order convergence on this problem, as there is with the linear scheme. Work continues with the nonlinear scheme to try to recover better asymptotic error behavior at steady state. Based on previous experience with the nonlinear formulation, the asymptotic error level can be reduced by further optimization of the biasing parameters and the entropy fix.

	Density	3^{rd} ENO
Grid	$\log L_2$	Rate
33x33	-2.275	
65x65	-2.572	0.99
129x129	-2.871	0.99
257x257	-3.170	0.99

Table IIb: *Captured Mach 2.5 bow-shock around circular cylinder using third-order ENO shock capturing scheme.*

Comparing the "near-body" and "blunt-body" solution errors, we have established that capturing the discontinuity in the blunt-body case causes a degradation in accuracy. The resulting convergence rate is first-order for both the linear and nonlinear formulations. We claim that this result is general for any multi-dimensional shock, and any high-order numerical method. A heuristic explanation for this phenomena is related to the ambiguous shock position within the cell. Capturing the shock provides (through conservation and the Rankine-Hugoniot relation) the post shock conditions for the smooth near-body problem. Because the exact position of the shock is ambiguous to order δx these "numerical" conditions are incorrect to first-order. This first-order error is relatively small on coarse grids, but at some level of refinement becomes the dominant error term.

Possible exceptions to the first-order conclusion include the case where a multi-dimensional shock can be "one-dimensionalized" by a suitable rotation. For example, if the numerical grid is aligned with the shock throughout the domain, and the Roe solver is used to rectify the interface states then design accuracy is possible at steady-state. This is roughly equivalent to shock fitting, and is a formidable task in general situations.

First-Order Implications

We have demonstrated that captured shocks in 2-D are first-order, regardless of the design accuracy of the capturing scheme. At some point of spatial resolution the solution is dominated by the first-order component of the error. This raises the obvious question, "If solution error is bounded at first-order, to what extent should high-order formulations be considered for capturing discontinuous flows"? Specifically, for what class of problems does the first-order error component dominate the solution error, making additional high-order work counter-productive? We first present a parametric study of design accuracy, to quantify the nature of the first-order error component. We then begin to address the specific role of high-order algorithms in the context of shock capturing.

Dependance of Error on Design Accuracy

Tables IIIa-IIIc contain a comparison of different design accuracies on the Mach 2.5 blunt body problem. The study is performed using the linear algorithm. Work continues with the nonlinear algorithm to quantify the generality of the conclusions drawn in this study. We include spatial operators of first- second- and fourth-order accuracy. The fourth-order pressure and density results shown previously are compared with those obtained with the second- and first-order algorithms. We see that all methods are asymptotically first-order. The results from the first-order (design accuracy) scheme are very poor, and only a partial listing is included. Note that the asymptotic level of error in the second- and fourth-order schemes is the same. It appears that the first-order component of the captured error is almost independent of the design order of accuracy of the method. The fourth-order scheme quickly approaches the asymptotic limit, while the

second-order scheme asymptotes more slowly. The first-order (design accuracy) scheme will never be dominated by shock error.

	Density	4^{th}	Pressure	4^{th}
Grid	$\log L_2$	Rate	$\log L_2$	Rate
33x33	-1.756		-1.651	
65x65	-3.404	5.47	-3.370	5.74
129x129	-3.708	1.01	-3.778	1.32
257x257	-4.014	1.02	-4.117	1.13
513x513	-4.317	1.01	-4.437	1.06

Table IIIa: *Fourth-order linear algorithm.*

	Density	2^{nd}	Pressure	2^{nd}
Grid	$\log L_2$	Rate	$\log L_2$	Rate
33x33	-2.327		-2.087	
65x65	-2.776	1.49	-2.933	2.81
129x129	-3.242	1.55	-3.664	2.43
257x257	-3.660	1.39	-4.321	2.18
513x513	-4.034	1.24	-4.452	0.44

Table IIIb: *Second-order linear algorithm.*

	Density	1^{st}	Pressure	1^{st}
Grid	$\log L_2$	Rate	$\log L_2$	Rate
33x33	-0.891		-0.745	
65x65	-1.335	1.47	-1.049	1.01
129x129	-1.683	1.16	-1.348	0.99
257x257	-2.040	1.19	-1.652	1.01

Tables IIIc: *First-order linear algorithm used to capture the Mach 2.5 bow-shock around a supersonic circular cylinder.*

A heuristic model expressing the nature of the solution error exhibited by the linear schemes, must include a first-order and a design-order component. A model approximately consistent with the solution errors presented in Tables IIIa-c is:

$$\epsilon = c_1(\delta x)^1 + c_2(\delta x)^r \qquad (4)$$

where ϵ is the solution error, r is the design order of the numerical algorithm, and c_1 and c_2 are problem dependent constants. For $r > 1$, and any finite values c_1 and c_2, the solution error will asymptotically be dominated by the first-order error component. If $c_1 << c_2$, the solution will exhibit high-order convergence on coarse grids.

The Role of High-Order Shock Capturing

Practitioners, are interested in absolute error, not the order of the spatial approximation. Order of accuracy and absolute error are closely related in the asymptotic limit of high accuracy. Most engineering problems, however, require error levels far removed from this asymptotic limit. Thus, a second-order algorithm could converge at its design rate, for many target accuracies. This would explain why no one has quantified the first-order convergence of captured shocks over the past thirty years.

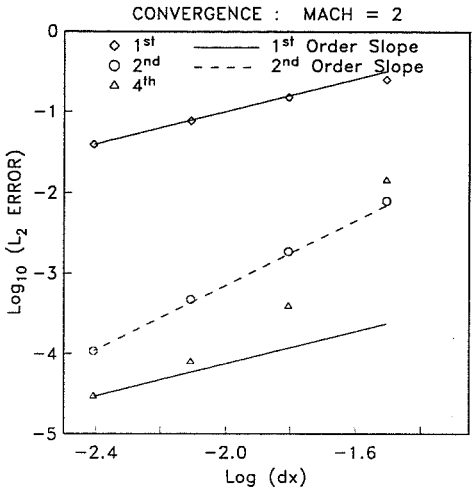

Figure 12. *Grid refinement study at Mach = 2.0, showing dependence of solution error on the design accuracy of the numerical scheme.*

Practitioners are beginning to demand more accuracy from their calculations. It is now common in aero-acoustics and electro-magnetics to demand resolution of scales which differ by several orders of magnitude. In configuration aerodynamics a commonly used metric of solution accuracy for viscous airfoils is one drag count, which corresponds to solution accuracies of at least four significant digits. As the design accuracy requirements increase, it is much more likely that the solution error will be dominated by the first-order component downstream of a discontinuity. When this occurs, global refinement of the solution is no longer a viable procedure; local refinement of the shock region must be performed to obtain an accurate solution.

We now show a parametric study in Mach number, using the linear algorithms of fourth-, second- and first-order accuracy. The objective of the study is to show that the efficacy of high-order methods is dependent on the problem as well as the target accuracy level. Figure 13 shows a plot of the pressure data presented in Table IIIa. Lines of unit slope are included to compare the asymptotic convergence rates of the methods. On this plot one can more easily identify which method is the most efficient for a

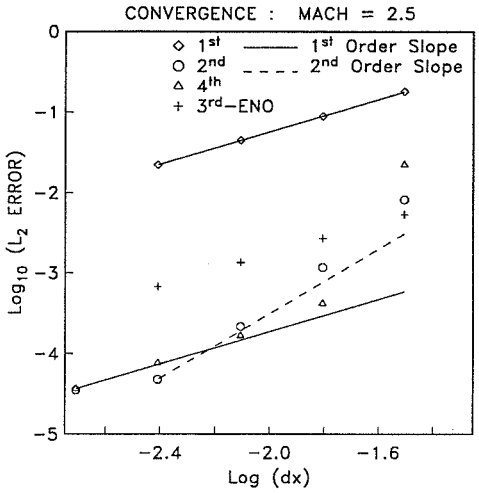

Figure 13. *Grid refinement study at Mach = 2.5, showing dependence of solution error on the design accuracy of the numerical scheme.*

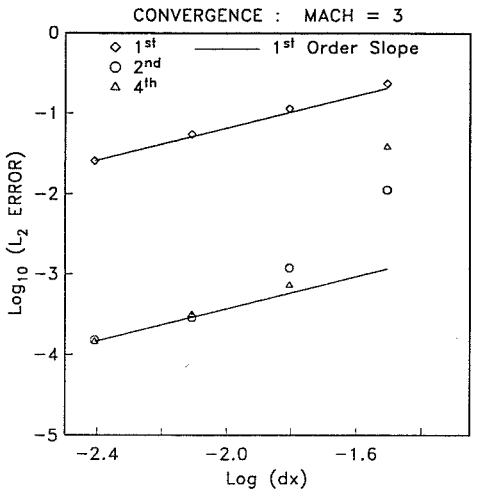

Figure 14. *Grid refinement study at Mach = 3.0, showing dependence of solution error on the design accuracy of the numerical scheme.*

given target accuracy. At a target accuracy of 10^{-2} the second order scheme is most desirable. (On the coarsest grid the second-order scheme is more accurate than the fourth-order scheme.) At a target of 10^{-3} the fourth-order scheme is most desirable. At one drag count, or four significant digits (10^{-4}), both methods are in the first-order asymptotic limit. Neither method is computationally efficient, and refinement of the grid in the bow-shock region would be the best use of computer resources.

The results in figure 13 are consistent with the observation that in many circumstances the first-order shock component of the solution error is negligibly small. Note that the second-order scheme is profoundly more accurate than the first-order scheme, and only begins showing its first-order character on extremely fine grids. Seldom have accuracy levels comparable to those reported here been obtained by CFD practitioners because of the costs involved. It is not surprising that the first-order nature of the captured solution has not been uniformly recognized till now.

Mach	Density	Pressure
2.0	2.667:1	4.500:1
2.5	3.333:1	7.125:1
3.0	3.857:1	10.333:1

Table IV: *Centerline, bow-shock, density and pressure ratios, as a function Mach number.*

Figures 12 and 14 show results for Mach numbers 2 and 3, respectively. The three numerical schemes used in the Mach = 2.5 case are used in these studies. Table IV shows the shock strengths as a function of Mach number for the range $2 \leq M \leq 3$. The conclusions drawn in the Mach = 2.5 case appear to be reasonably general for this range of Mach numbers. Specifically, the first-order (design accuracy) results are not competitive with either the second- or fourth-order results. Both higher-order methods exhibit design accuracy on coarse grids, but asymptote to first-order on fine grids. The asymptotic level of the higher-order schemes is nearly independent of the design accuracy. At low target accuracies, the second-order scheme is most desirable, and at moderate target accuracies, the fourth-order scheme is most desirable. At high target accuracies, the high-order schemes are first-order because of the shock, and regridding the shock is necessary to effectively decrease the overall accuracy of the calculation.

The convergence rates at all Mach numbers are consistent with the heuristic model proposed in equation 4. In addition, we see a slight dependence of the asymptotic first-order shock error on the shock strength, that increases with Mach number. Work continues to quantify this effect, and to be able to predict the shock capturing error levels at the shock. It is hoped that this quantification will provide some general guidance for capturing shocks of different strengths, and for when refinement of the shock is necessary to ensure satisfactory results near the body.

Conclusions

An assessment of the accuracy of shock capturing schemes is made for two-dimensional steady flows.

A linear fourth-order method and a nonlinear third-order method are used in this study. It is shown, contrary to conventional wisdom, that captured two-dimensional shocks are asymptotically first-order, regardless of the design accuracy of the numerical method used to obtain them.

The solution error of the captured discontinuity can be characterized by a first-order component $c_1(\delta x)^1$, and a high order component $c_2(\delta x)^r$ (r is the design order of the method). With sufficient resolution, the error is dominated by the first-order terms. In a practical sense, however, frequently the solution error is dominated by the high-order component, giving the appearance of a high-order convergence rate.

Finally, we acknowledge that demonstrating a first-order convergence rate with two numerical methods, does not prove that captured shocks are destined to be first-order accurate. Rather, it demonstrates that we do not presently know how to achieve high order convergence in a general context when discontinuities are present. Work continues towards the goal of design accuracy for captured discontinuities.

References

1. MacCormack, R., W., "The Effects of Viscosity in Hypervelocity Impact Cratering", AIAA Paper 69-354, 1969.

2. Casper, J., and Carpenter, M. H., "Computational Considerations for the Simulation of Shock-Induced Sound," NASA TM 110222, Dec., 1995, to appear *SIAM J. of Sci. Comput.*, Vol. 19, No. 1, January, 1998.

3. Carpenter, M. H., and Casper, J., "Computational Considerations for the Simulation of Discontinuous Flows," *Barriers and Challenges in Computational Fluid Dynamics*, V. Venkatakrishnan, ed., Kluwer Academic Publishing, 1997.

4. Kopriva, David A., "Spectral Methods for the Euler Equations-The Blunt Body Problem Revisited," *AIAA Journal*, Vol. 29, Sept. 1991, pp. 1458-1462.

5. Carpenter, M. H., Gottlieb, D., and Abarbanel, S., "The Stability of Numerical Boundary Treatments for Compact High-Order Finite-Difference Schemes," *Journal of Computation Physics*, Vol. 108, No. 2, October, 1993.

6. Carpenter, M. H., Atkins, H. L. and Singh, D.J.,
"Characteristic and Finite-Wave Shock-Fitting Boundary Conditions for Chebyshev Methods," *Transition, Turbulence, and Combustion*, Vol. II, M. Y. Hussaini, T. B. Gatski, and T. L. Jackson, eds., Kluwer Academic Publishers, 1994.

7. Casper, J. and Atkins, H. "A Finite-Volume High-Order ENO Scheme for Two-Dimensional Hyperbolic Systems," *Journal of Computational Physics*, Vol. 106, pp. 62-76, May, 1993.

8. Casper, J., Shu, C., and Atkins, H. "A Comparison of Two Formulations for High-Order Accurate Essentially Non-Oscillatory Schemes," *AIAA Journal*, Vol. 32, No. 10, Oct., 1994., pp. 1970-1977.

9. Shu, C. and Osher, S., "Efficient Implementation of Essentially Non-Oscillatory Shock-Capturing Schemes," *Journal of Computational Physics*, Vol. 77, No. 2, 1988, pp. 439-471.

10. P. L. Roe, "Approximate Riemann Solvers, Parameter Vectors, and Difference Schemes," *Journal of Computational Physics*, Vol. 43, 1981, pp. 357-372.

11. Harten, A., Lax, P., and Van Leer, B. "On Upstream Differencing and Godunov-Type Schemes for Hyperbolic Conservation Laws," *SIAM Review*, Vol 25, 1983, pp. 35-61.

COMPUTATIONAL CONSIDERATIONS FOR THE SIMULATION OF SHOCK-INDUCED SOUND

Jay Casper
Old Dominion University
Norfolk, Virginia

Mark H. Carpenter
NASA Langley Research Center
Hampton, Virginia

Accepted for Publication in
SIAM Journal on Scientific Computing
to appear January, 1998

COMPUTATIONAL CONSIDERATIONS FOR THE SIMULATION OF SHOCK-INDUCED SOUND

Jay Casper*
Old Dominion University
Norfolk, Virginia

Mark H. Carpenter†
NASA Langley Research Center
Hampton, Virginia

ABSTRACT

The numerical study of aeroacoustic problems places stringent demands on the choice of a computational algorithm, because it requires the ability to propagate disturbances of small amplitude and short wavelength. The demands are particularly high when shock waves are involved, because the chosen algorithm must also resolve discontinuities in the solution. The extent to which a high-order-accurate shock-capturing method can be relied upon for aeroacoustics applications that involve the interaction of shocks with other waves has not been previously quantified. Such a study is initiated in this work. A fourth-order-accurate essentially nonoscillatory (ENO) method is used to investigate the solutions of inviscid, compressible flows with shocks. The design order of accuracy is achieved in the smooth regions of a steady-state, quasi-one-dimensional test case. However, in an unsteady test case, only first-order results are obtained downstream of a sound-shock interaction. The difficulty in obtaining a globally high-order-accurate solution in such a case with a shock-capturing method is demonstrated through the study of a simplified, linear model problem. Some of the difficult issues and ramifications for aeroacoustic simulations of flows with shocks that are raised by these results are discussed.

*Research Assistant Professor, Department of Aerospace Engineering, Old Dominion University, Norfolk, VA 23529; supported by U.S. Government grant NAG1-1653.

†Research Engineer, Fluid Mechanics and Acoustics Division, NASA Langley Research Center, Hampton, VA 23681.

INTRODUCTION

This work is motivated by the desire to develop numerical methods that will be useful in the study of aeroacoustic phenomena that occur in flows with shocks. For example, shocks in jet flows, on wings, and in supersonic combustion inlets contribute significantly to sound generation. Problems such as these represent some of the more challenging aspects of ongoing research in the developing area of computational aeroacoustics (CAA).

One of the purposes of this work is to open a discussion on the relative merits of the numerical methods which can simulate sound sources that are generated in flows with shocks. For a computational algorithm, obtaining acoustic information from a numerical solution that involves shock waves is a demanding proposition. In general, high-order accuracy is required for the propagation of high-frequency low-amplitude waves. In addition, the shock must be adequately captured. A significant body of work has been devoted to the development of numerical schemes that possess both properties.

The contribution of a shock wave to the generation of sound is attributed to the motion of the shock wave and its interaction with other disturbances in the flow. These disturbances can be large, such as changes in the mean flow, or small, such as acoustic or vortical disturbances. The extent to which such interactions must be accurately predicted in order to propagate reliable information to an observer will be investigated.

In the following section, some of the currently available methods that vary in their approach to high-order accuracy and shock capturing are surveyed. Next, a fourth-order-accurate essentially nonoscillatory (ENO) method is applied to the steady solution of a nozzle flow with a shock, and fourth-order-accurate results are obtained. However, in the application of the same numerical scheme to a time-dependent problem, that of a sound-shock interaction, accuracy suffers. The disappointing results in regard to the accuracy of this solution are explained through the study of a simpler linear model problem. The numerical scheme is modified with a subcell resolution technique in order to obtain a globally high-order-accurate solution for time-dependent simulations. The original sound-shock interaction problem is again solved with the modified scheme, and

a fourth-order-accurate solution is achieved. Some of the difficult issues and ramifications for current methods that are raised by these results are discussed in the final section.

HIGH-ORDER ACCURATE SHOCK-CAPTURING METHODS

The high-order-accurate spatial operator that is desired in a shock-capturing method for CAA problems requires that information be taken from a large number of discrete locations within the solution. Such an operator will cause large oscillations in a discontinuous solution unless special precautions are taken. Many methods are available in the literature that attempt to balance the properties of high-order accuracy and shock capturing. However, they can be classified into two categories *i.e.*, linear and nonlinear.

Within the linear class of numerical shock-capturing schemes, the interpolation set for the approximation of the solution or its derivatives is fixed as a function of grid location. Linear methods admit oscillations in regions in which physical gradients are inadequately resolved. Central-differencing operators and spectral methods are particularly prone to these numerical oscillations. For nonlinear problems, limiters or filters are usually required to keep oscillations from growing without bound. The general features of these ideas are demonstrated in the work of Don,[1] in which pseudospectral methods are used for compressible flow problems with shocks by locally applying a simple filter to keep the solution bounded during the computation. The final solution is post-processed in order to remove the oscillatory information that developed in time. Nothing in this approach mandates the use of pseudospectral techniques; other higher-order schemes (*e.g.*, central-difference or compact schemes[2]) could also be used. For example, Harten and Chakravarthy[3] suggest a polynomial interpolation procedure in which the coefficients of the polynomial are limited by a switch that makes a coefficient very small if the corresponding solution derivative is discontinuous.

In the nonlinear class of schemes, the strategy with respect to discontinuities is to employ some sort of adaptive interpolation. The goal is to achieve formal high-order accuracy in smooth regions and high shock resolution without oscillations. The class of ENO schemes[4,5] has been designed to

have such properties. As originally presented, the local polynomial approximation operator adapts its interpolation set to the smoothest available part of the solution. This adaptive interpolation strategy has also been employed in the development of psuedospectral hybrid schemes.[6–8]

Although discontinuous solutions generated by a linear strategy are usually not as pictorially pleasing as solutions in which shock profiles are monotone, linear schemes are more computationally efficient than nonlinear schemes. The efficiency of a numerical algorithm is extremely important for aeroacoustic simulations because such problems are time dependent and require a fine computational mesh for the resolution of high-frequency disturbances. Because nonlinear methods are designed to avoid the production of spurious oscillations, the stability of a calculation of a flow with shocks is more readily obtained. However, their adaptive interpolation operator significantly hampers their efficiency relative to linear schemes.

In the literature to date, the design accuracy of a numerical method, whether linear or nonlinear, has been demonstrated with solutions to smooth problems. Problems with discontinuous solutions are most commonly used only to illustrate the ability of the scheme to obtain a stable solution to such problems. In the following two sections, the ability of a fourth-order accurate ENO method to achieve high-order accuracy in the smooth regions of a flow with a shock is investigated. The method is applied to obtain the solutions of a steady problem and a time-dependent sound-shock interaction. The accuracies of these solutions are then analyzed through the study of a simpler linear model problem.

STEADY SHOCK IN A NOZZLE

A steady-state flow with a shock in a quasi-one-dimensional converging-diverging nozzle is numerically investigated. The governing equations are the quasi-one-dimensional Euler equations:

$$\frac{\partial}{\partial t}(AU) + \frac{\partial}{\partial x}(AF) = G \tag{1a}$$

where

$$U = \begin{bmatrix} \rho \\ \rho u \\ \rho E \end{bmatrix}, \quad F = \begin{bmatrix} \rho u \\ \rho u^2 + P \\ (\rho E + P)u \end{bmatrix}, \quad G = \begin{bmatrix} 0 \\ P\frac{dA}{dx} \\ 0 \end{bmatrix} \tag{1b}$$

The variables ρ, u, P, E, and A are the density, velocity, pressure, total specific energy, and nozzle area, respectively. The equation of state is

$$P = (\gamma - 1)\rho(E - \frac{1}{2}u^2)$$

where γ is the ratio of specific heats, which is assumed to have a constant value of 1.4.

The spatial domain of the nozzle is $0 \leq x \leq 1$, and the flow is oriented from left to right. The nozzle shape is determined exactly through the requirement of a linear distribution of Mach number from $M = 0.8$ at the inlet to $M = 1.8$ at the exit, assuming the flow is isentropic and fully expanded. The resulting area distribution $A(x)$ is illustrated in Fig. 1a. The flow variables are normalized with respect to upstream stagnation conditions and the area with respect to the value at the throat, $x = 0.2$.

Given the prescribed area distribution, the Mach 0.8 inflow state is retained at $x = 0$, and the outflow condition at $x = 1$ is determined such that a shock forms at $x_s = 0.5$, which corresponds to a preshock Mach number of $M = 1.3$. A steady-state solution is obtained by implementing a fourth-order-accurate ENO method until residuals are driven to machine zero. Spatial accuracy is achieved by solving the equations in control-volume form as presented in Ref. 4. The equations are integrated in time via a third-order-accurate Runge-Kutta scheme.[5] This numerical method will be referred to as "ENO-4-3." As has been established in previous research,[9–12] the adaptive stencils employed in the spatial operator are biased in smooth regions toward those that are linearly stable. Fig. 1b depicts the solution, with respect to Mach number, on a uniform mesh of 128 cells.

One of the simpler methods of determining the error of this solution relies on the fact that the value of the entropy-like quantity P/ρ^γ is piecewise constant:

$$S \equiv \frac{P}{\rho^\gamma} = \begin{cases} S_{-\infty}, & x < x_s \\ S_\infty, & x > x_s \end{cases}$$

The subscripts of S denote the pre-shock and post-shock stagnation values, respectively. This quantity is plotted in Fig. 1c. The pointwise entropy error for this solution on four successively refined meshes is illustrated in Fig. 2. Clearly, the accuracy is fourth order on either side of the shock, as demonstrated by the error data in Table I. The variable N_c is the number of cells. The

errors $||e||$ are computed in the L_1 and L_∞ norms. The number r_c is the computational order of accuracy and is determined by the slope of these tabulated values on a log-log plot:

$$r_c = \frac{\ln\left(e_{h_k}/e_{h_{k+1}}\right)}{\ln\left(h_k/h_{k+1}\right)}$$

where e_{h_k} is the error measured on a mesh of uniform spacing h_k with $h_k > h_{k+1}$ for $k = 1, 2, 3$.

Although these results are encouraging, the time independence of the solution makes this a convenient example for the demonstration of high-order accuracy in the presence of a shock. As will be shown in the study of an unsteady problem in the following section, a moving shock presents a greater challenge in regard to high-order-accurate shock capturing.

SOUND-SHOCK INTERACTION

The interaction of a sound wave with a shock in a one-dimensional flow is numerically investigated. The effects of shocks on sound waves, and *vice versa*, are important to the acoustics and performance of aircraft design. Therefore, the ability to obtain an accurate solution to such a model initial-boundary-value problem (IBVP) is important in the development of shock-capturing methods for CAA research. Similar one-dimensional problems have been the subject of other studies.[13,14]

The governing equations are the one-dimensional Euler equations:

$$\frac{\partial}{\partial t}U + \frac{\partial}{\partial x}F(U) = 0 \tag{2a}$$

where the components of U and $F(U)$ are identical to those given in Eq. 1b. The equation of state is also the same as in the previous example.

The spatial domain is $0 \leq x \leq 1$. The piecewise constant initial conditions, U_L and U_R, are those of a steady shock located at $x_s = 0.5$. The flow is from left to right, and the state U_L is a Mach 2 flow upstream of the shock. The flow variables are normalized with respect to this upstream flow. At $t = 0$, an acoustic disturbance is introduced at $x = 0$:

$$
\begin{aligned}
P(0,t) &= P_L\,(\,1+\epsilon\,\sin\,\omega t\,) \\
\rho(0,t) &= \rho_L\left[\frac{P(0,t)}{P_L}\right]^{1/\gamma} \\
u(0,t) &= u_L+\frac{2}{\gamma-1}[\,c(0,t)-c_L\,]
\end{aligned}
\tag{2b}
$$

where ω is the circular frequency, ϵ is the amplitude, and $c=\sqrt{\gamma P/\rho}$ is the local sound speed.

The numerical solution of this problem is obtained through the implementation of the ENO-4-3 algorithm. This algorithm will be fourth-order accurate even for a time-dependent problem when the time step is suitably restricted. The exact solution is obtained by a two-domain Chebyshev spectral technique.[15] Shock fitting is used to divide the domain into two computational regions. A Chebyshev collocation method is used in each region for the spatial discretization. A fourth-order Runge-Kutta scheme is used to discretize time. Sufficient spatial and temporal resolution are used to guarantee machine precision of the solution.

Fig. 3 depicts the pressure perturbation $\delta P(t) = P(x,t) - P(x,0)$ at $t = 30\,T_\lambda$, where $T_\lambda = 2\pi/\omega$ is one period of the incoming acoustic wave. The acoustic wave amplitude is $\epsilon = 0.001$, and $\omega = 2\pi k(u_L + c_L)$ is determined by requiring a wave number $k = 6$ with respect to unit length and a mean wave speed $u_L + c_L$. The calculation, represented by circles, was performed on a uniform mesh of 256 cells with a Courant number of 0.5. The exact solution is represented by a continuous line. In this pictorial measure, the numerical algorithm performs well with respect to its prediction of the amplified sound wave at higher frequency downstream of the shock. The missing circle values near the shock are off the plot and are due to the use of the stencil-biasing parameters near a moving discontinuity.[16]

Even more instructive, however, is the pointwise error made by this calculation with respect to the mesh width. Fig. 4 illustrates this error on four successively refined meshes. The solution is clearly fourth-order accurate upstream of the shock, but only first-order downstream of the shock, as shown by the L_∞ error data in Table II. The errors are computed on two spatial subdomains: $0 \le x \le 0.45$ and $0.55 \le x \le 1$. In this manner, the first-order error that is generated in the

vicinity of the shock is avoided. This disappointing result is more easily explained through the study of a simpler model problem, which is examined in the following section.

A LINEAR MODEL PROBLEM

The lower-order accurate results of the previous section can be analyzed through the study of a linear scalar model problem. The solution of the following IBVP is instructive because it isolates the important phenomenon of propagation of information through a discontinuity. This trait will be common to almost any aeroacoustic problem that involves shock waves. Consider the scalar equation:

$$\frac{\partial u}{\partial t} + a(x)\frac{\partial u}{\partial x} = 0 \tag{3a}$$

where the piecewise constant wave speed $a(x)$ is

$$a(x) = \begin{cases} 2\,, & x \le x_s \\ 1\,, & x > x_s \end{cases} \tag{3b}$$

The initial conditions are chosen as

$$u(x,0) = \begin{cases} \frac{1}{2}\,, & x \le x_s \\ 1\,, & x > x_s \end{cases} \tag{3c}$$

The spatial domain is $0 \le x \le 1$, and the discontinuity location is $x_s = 0.5$. The inflow boundary condition is

$$u(0,t) = \frac{1}{2}\left(1 + \epsilon \sin \omega t\right) \tag{3d}$$

with $\epsilon = 0.001$ and ω determined by requiring a wave number $k = 2$ with respect to unit length and the upstream wave speed $a = 2$.

For the purpose of the subsequent discussion, it is necessary to briefly describe the numerical scheme. The semi-discrete, finite-volume formulation is obtained by integrating Eq. 3a on an interval $[x_{i-1/2}, x_{i+1/2}]$ with center x_i and "volume" Δx_i :

$$\frac{\partial}{\partial t}\bar{u}_i(t) = \frac{-1}{\Delta x_i}\left[\hat{f}_{i+1/2}(t) - \hat{f}_{i-1/2}(t)\right] \tag{4a}$$

where

$$\bar{u}_i(t) = \frac{1}{\Delta x_i} \int_{x_{i-1/2}}^{x_{i+1/2}} u(x,t)\, dx \tag{4b}$$

is the cell average of u on the ith interval at time t, and the flux $\hat{f}_{i+1/2}(t)$ is

$$\hat{f}_{i+1/2}(t) = a(x_{i+1/2})\, u(x_{i+1/2}, t) \tag{4c}$$

Temporal integration is achieved by a Runge-Kutta method.[5] A numerical approximation to the flux in Eq. 4c is determined in two steps. First, given the cell averages, the solution is approximated pointwise within each cell.

$$\mathcal{P}_i(x) \approx u(x,t)\,, \quad x_{i-1/2} \le x \le x_{i+1/2} \tag{4d}$$

In this particular application, $\mathcal{P}_i(x)$ is a cubic polynomial. The process by which $\mathcal{P}_i(x)$ is obtained will be referred to as "reconstruction." This reconstruction operator contains the adaptive stencil algorithm, which avoids interpolation across steep gradients. (See Ref. 4 for details.) Then, at a cell interface $x_{i+1/2}$, two solution values can exist, as shown in Fig. 5. Correspondingly, two flux values can also exist. The second step, then, is simply to choose the upwind value which, for the present problem, yields the following numerical flux approximations:

$$\begin{array}{rcl} \hat{f}_{i-1/2}(t) & \approx & a(x_{i-1/2})\, \mathcal{P}_{i-1}(x_{i-1/2}) \\ \hat{f}_{i+1/2}(t) & \approx & a(x_{i+1/2})\, \mathcal{P}_i(x_{i+1/2}) \end{array} \tag{4e}$$

Fig. 6 depicts the perturbation $\delta u(t) = u(x,t) - u(x,0)$ at $t = 10\,T_\lambda$, with the ENO-4-3 algorithm. Note the similarity of the features of this solution to those of the sound-shock interaction in regard to the changes in amplitude and frequency across the discontinuity. The calculation, represented by circles, was performed on a uniform mesh of 64 cells with a Courant number of 0.5. The exact solution is

$$u(x,t) = \begin{cases} \frac{1}{2}\left[\,1 + \epsilon \sin \omega(t - x/2)\,\right]\,, & 0 \le x \le x_s \\ 1 + \epsilon \sin \omega(t - x + x_s)\,, & x_s < x \le 1 \end{cases} \tag{5}$$

for $t \ge 3/4$, after the perturbation first reaches $x = 1$.

Because of the linearity of this problem, the discontinuity location x_s remains fixed for all time, unlike the sound-shock interaction problem. Therefore, x_s can be conveniently placed with

respect to a given mesh. For instance, if the computational mesh is composed of an even number of uniform cells, then $x_s = 0.5$ will lie on a grid point (*i.e.*, a cell face). Fig. 7a depicts the pointwise computational error for this problem on four successively refined meshes for which x_s lies on a grid point. The numerical solution is fourth-order accurate throughout the domain, as shown by the error data in Table III. However, for an odd number of uniform cells, x_s is interior to a cell, and the solution is first-order accurate downstream of the discontinuity, as shown in Fig. 7b and Table IV.

The strikingly different results in Figs. 7a and 7b yield insight into the disappointing results for the sound-shock interaction problem of the previous section. Even if the initial steady shock were located on a cell face, it would move into the interior of a cell upon interaction with the upstream acoustic wave. Therefore, the following explanation for the lower-order accurate results focuses on the location of the discontinuity with respect to the boundary or interior of a cell.

The difference in the results in Figs. 7a and 7b can be explained in terms of the interpolation operator and its direct influence upon the numerical flux. First, consider the case in which the discontinuity is on a grid point, for example, the left-hand endpoint of the ith cell, as shown in Fig. 8a. Because of the adaptive interpolation, the polynomial approximation within the adjoining cells is of pointwise, high-order accuracy. The large jump at the left-hand interface of the ith cell is immaterial because the flux is determined by the value $\mathcal{P}_{i-1}(x_{i-1/2})$ and the upstream wave speed $a = 2$, as given by Eq. 4e. Now, consider the case in which x_s is in the interior of the ith cell, as in Fig. 8b. Unlike Fig. 8a, the polynomial approximation in the ith cell now contains a pointwise error that is $O(1)$. This still does not affect the flux into the ith cell, because the inbound flux is determined only by information in the $(i-1)$th cell. However, the outbound flux is influenced by the value $\mathcal{P}_i(x_{i+1/2})$, which is ultimately responsible for the large errors downstream of the discontinuity.

The loss in accuracy in numerical solutions of linear problems with discontinuous initial data has been the subject of previous research by other authors.[17–20] All of these previous studies involved solutions of coupled linear systems. It is, therefore, instructive to note that the solution of

IBVP 3 is analogous to that of a coupled system in the following way. Let u_1 denote the solution of Eqs. 3a-d on $0 \leq x \leq x_s$, and u_2 denote the solution on $x_s < x \leq 1$. Now consider, for $\delta > 0$, the solution u_2 on $x_s < x < x_s + \delta$. The downstream solution u_2 is coupled to u_1 by the requirement of flux conservation:

$$\lim_{\delta \to 0} a(x_s + \delta)\, u_2(x_s + \delta, t) = a(x_s)\, u_1(x_s, t)$$

As in the present study, the work of Majda and Osher[17] was concerned with the inherent degradation in accuracy in a region in which information must be numerically propagated across a discontinuity. Majda and Osher suggested that this difficulty could be circumvented by smoothing the initial data. (See Ref. 17 for details.) However, because the goal of the present work is the application of numerical methods to solutions of nonlinear problems, the approach suggested by Donat and Osher[20] is more appropriate to use here. These authors propose to maintain accuracy across discontinuities by using Harten's ideas on subcell resolution.[21]

In an attempt to achieve a globally high-order-accurate solution, a subcell resolution technique is considered. In particular, a modification of the procedure presented in Ref. 21 is detailed. The goal is to obtain a better pointwise approximation of the outbound flux in the ith cell in Fig. 8b. If the ith cell is decomposed into two subcells whose adjacent face is x_s, then the polynomial approximation $\mathcal{P}_i(x)$ would be replaced with the piecewise polynomial approximation

$$\tilde{\mathcal{P}}_i(x) = \begin{cases} \mathcal{P}_L(x)\,, & x_{i-1/2} \leq x < x_s \\ \mathcal{P}_R(x)\,, & x_s < x \leq x_{i+1/2} \end{cases} \tag{6}$$

where $\mathcal{P}_L(x)$ and $\mathcal{P}_R(x)$ approximate $u(x,t)$ in the ith cell to high-order pointwise accuracy on either side of the discontinuity. Because the inbound flux is accurately approximated with the polynomial in the $(i-1)$th cell, $\mathcal{P}_L(x)$ can be determined by simple extrapolation of $\mathcal{P}_{i-1}(x)$, as shown in Fig. 9. With this reasoning, for the present piecewise cubic polynomial reconstruction, clearly

$$\bar{u}_i(t) = \frac{1}{\Delta x_i}\left[\int_{x_{i-1/2}}^{x_s} \mathcal{P}_{i-1}(x)\, dx + \int_{x_s}^{x_{i+1/2}} \mathcal{P}_R(x)\, dx\right] + O(\Delta x^4) \tag{7}$$

Finally, $\mathcal{P}_R(x)$ must be accurately determined, which enables an accurate outbound flux calculation given by $\mathcal{P}_R(x_{i+1/2})$. Let $\bar{u}_R$ denote the subcell average of $\mathcal{P}_R(x)$ on $[x_s, x_{i+1/2}]$. Then,

clearly, from Eq. 7,

$$\bar{u}_R = \frac{1}{x_{i+1/2} - x_s} \left[\Delta x_i \, \bar{u}_i(t) - \int_{x_{i-1/2}}^{x_s} \mathcal{P}_{i-1}(x) \, dx \right] + O(\Delta x^4) \tag{8}$$

The desired cubic polynomial $\mathcal{P}_R(x)$ is then determined by applying the reconstruction operator to the set $\{\bar{u}_R, \bar{u}_{i+1}(t), \bar{u}_{i+2}(t), \bar{u}_{i+3}(t)\}$, which contains only smooth solution information.

Note that, for the solution of the present problem, the outbound flux cannot be determined by the leftward extrapolation of $\mathcal{P}_{i+1}(x)$, as in Ref. 21. This method would be appropriate only if the initial conditions contained the propagating wave profile. In the current problem, at $t = 0$, the solution is constant downstream of x_s. Therefore, the extrapolation of $\mathcal{P}_{i+1}(x)$ into the ith cell would never allow the wave to propagate into the $(i + 1)$th cell.

The subcell resolution method described above was incorporated into the ENO algorithm, and the linear model problem was again solved with the discontinuity located in the interior of a cell. This modified scheme will be referred to as "ENO-4-3-SR." The globally high-order-accurate results are shown by the pointwise error plot in Fig. 10 and the data in Table V.

SOUND-SHOCK INTERACTION: REVISITED

The sound-shock interaction problem is again solved; this time the subcell resolution methodology from the previous section is incorporated. However, the subcell technique applied in the linear problem above does not immediately carry over to this nonlinear case. The method in Eqs. 6-8 is dependent upon the discontinuity location x_s. For the nonlinear case, at a given time t, the shock location is not known *a priori* and, therefore, must be determined before the subcell technique in Eqs. 6-8 can be applied. This step can be accomplished by solving $H(x_s) = 0$ for x_s in the interval $(x_{i-1/2}, x_{i+1/2})$ where the function $H(x_s)$ is given by

$$H(x_s) = \frac{1}{\Delta x_i} \left[\int_{x_{i-1/2}}^{x_s} \mathcal{P}_{i-1}(x) \, dx + \int_{x_s}^{x_{i+1/2}} \mathcal{P}_{i+1}(x) \, dx \right] - \bar{u}_i(t) \tag{9}$$

Clearly, this function is derived from the relationship in Eq. 7.

For the current ENO-4-3-SR algorithm, $H(x_s)$ is a quartic polynomial. For a sufficiently small Δx_i, a unique real root of $H(x_s)$ exists in the interval $(x_{i-1/2}, x_{i+1/2})$. The root of $H(x_s)$ in the

i-th cell is determined numerically by interval halving; the interval midpoint is taken as the initial guess. After the shock location x_s is known, the subcell resolution discussed in the previous section is applied to the Euler equations in a component-by-component manner. Figure 11 illustrates the pointwise solution error determined by the modified ENO algorithm on four successively refined grids. An odd number of cells has been used for this grid-refinement study in order to facilitate the subcell resolution process. The shock movement is thereby contained within one cell. (A more general approach would require a search algorithm that finds the cell that harbors a shock before applying the subcell resolution technique.) Figure 11 shows that the solution converges at the same rate downstream of the shock as it does upstream, as shown by the L_∞ errors in Table VI.

DISCUSSION

The foregoing results raise several issues in regard to the development and application of high-order-accurate shock-capturing methods. Although the results presented here were obtained with a high-order ENO method, they are consistent with those obtained with linear high-order schemes. These issues indicate the need for further investigation into the relative merits of high-order-accurate shock-capturing schemes.

The observation that is, perhaps, the most discouraging is the apparent complexity in achieving high-order accuracy in the presence of moving shocks. There are at least two significant drawbacks to the inclusion of subcell resolution in a numerical algorithm. The first is the added cost. Although the additional expense for the subcell resolution was relatively minor for the sound-shock interaction problem, this modification does not suffice for the more general case. For example, the existence and location of a single shock was assumed to be known *a priori*. This assumption was valid because of the assuredness that the shock would not move outside the initial cell location, within the required sound-wave amplitude range and mesh-refinement parameterization. However, in the more general case, every cell must be tested for the harboring of a discontinuity before the subcell resolution can be applied. (Such a test is proposed in Ref. 21.) The second and more significant drawback to this approach is that its extension to multiple dimensions is not straight

forward. A shock is a curve in two-dimensional space, and a surface in three dimensions. The multiple parameterization required to extend Eq. 9 to two- and three-dimensional problems would be cumbersome, to say the least, and would still not guarantee a unique solution for the shock location and shape.

These observations raise considerable concern in regard to the use of high-order-accurate methods in the study of unsteady flows with shocks. If high-order methods only yield first-order results, why use them? Before this question can be fully answered, it must first be determined whether the first-order error from a high-order method is significantly smaller than that of a lower order method. Figure 12 depicts the error of the sound-shock interaction problem with a first-order upwind method (no subcell resolution). Upon comparison with the Figure 4, it is clear that the solution downstream of the shock is more accurate when using the higher-order method. This result is by no means conclusive, as there are many other considerations. For instance, what about second- or third-order methods? What about the cost of using a given method with respect to its accuracy? These and other concerns are topics for future research.

The ENO methods applied in the present work are designed to capture shocks narrowly without oscillations. However, this property alone was found insufficient to produce globally high-order results in the solution of an unsteady problem, which suggests that the nonoscillatory properties that guarantee the convergence (in the sense of weak solutions) of a nonlinear scheme do not also guarantee the rate of that convergence. If this is the case, why not use a linear method? How important is the control of a solution's total variation from the viewpoint of requiring an answer to a given problem? Is it sufficient to simply keep a given computation stable in order to extract the desired information from a solution? Further research is necessary in regard to the relative merits of linear and nonlinear schemes as they are applied to unsteady flows with shocks. Such research should include experiments that compare the solution errors of linear and nonlinear schemes with respect to their shock resolution, design accuracy, and computational efficiency.

REFERENCES

1. Don, W.S., "Numerical Study of Pseudospectral Methods in Shock Wave Applications," *Journal of Computational Physics*, Vol. 110, No. 1, January, 1994, pp. 103-111.

2. Lele, S.K., "Compact Finite Different Schemes with Spectral-Like Resolution," *Journal of Computational Physics*, Vol. 103, 1992, pp. 16-42.

3. Harten, A. and Chakravarthy, S., "Multi-Dimensional ENO Schemes for General Geometries," NASA Contractor Report 187637, ICASE Report No. 91-76, September, 1991.

4. Harten, A., Engquist, B., Osher, S., and Chakravarthy, S., "Uniformly High Order Accurate Essentially Non-Oscillatory Schemes III," *Journal of Computational Physics*, Vol. 71, No. 2, 1987, pp. 231-323.

5. Shu, C. and Osher, S., "Efficient Implementation of Essentially Non-Oscillatory Shock-Capturing Schemes," *Journal of Computational Physics*, Vol. 77, No. 2, 1988, pp. 439-471.

6. Cai, W.C., Gottlieb, D., Shu, C.W., "Essentially Non-Oscillatory Spectral Fourier Methods for Shock Wave Calculations," Math. Comp., Vol. 52, No. 186, 1989, pp. 389-410.

7. Cai, W.C., Shu, C.W., "Uniform High-Order Spectral Methods for One and Two-Dimensional Euler Equations," *Journal of Computational Physics*, Vol. 104, February, 1993, pp. 427-443.

8. Suresh, A., "An Assessment of Spectral Non-Oscillatory Schemes," *Journal of Computational Physics*, Vol. 114, 1994, pp. 339-349.

9. Rogerson, A. and Meiberg, E. "A Numerical Study of the Convergence Properties of ENO Schemes," *Journal of Scientific Computing*, Vol. 5, No. 2, 1990, pp. 151-167.

10. Shu, C., "Numerical Experiments on the Accuracy of ENO and Modified ENO Schemes," *Journal of Scientific Computing*, Vol. 5, No. 2, 1990, pp. 127-150.

11. Atkins, H., "High-Order ENO Methods for the Unsteady Navier-Stokes Equations," AIAA 91-1557, June, 1991.

12. Casper, J., Shu, C. W., and Atkins, H., "A Comparison of Two Formulations for High-Order Accurate Essentially Non-Oscillatory Schemes," *AIAA Journal*, Vol. 32, No. 10, pp. 1970-1977, October, 1994.

13. Meadows, K., Caughey, D., and Casper, J., "Computing Unsteady Shock Waves for Aeroacoustic Applications," *AIAA Journal*, Volume 32, No. 7, pp. 1360-1366, July, 1994.

14. Casper, J. and Meadows, K.R., "Using High-Order Accurate Essentially Non-Oscillatory Schemes for Aeroacoustic Applications ," AIAA 95-0163, January, 1995.

15. Carpenter, M. H., Atkins, H. L. and Singh, D. J., "Characteristic and Finite-Wave Shock-Fitting Boundary Conditions for Chebyshev Methods," *Transition, Turbulence, and Combustion*, Vol. II, M. Y. Hussaini, T. B. Gatski, and T. L. Jackson, eds., Kluwer Academic Publishers, 1994.

16. Casper, J., "Stability Considerations for High-Order Accurate Essentially Non-Oscillatory Schemes," in preparation.

17. Majda, A. and Osher, S., "Propagation of Error in Regions of Smoothness for Accurate Difference Approximations to Hyperbolic Equations," *Comm. Pure and Applied Math*, Vol. 30, 1977, pp. 671-705.

18. Mock, M. S. and Lax, P. D., "The Computation of Discontinuous Solutions of Linear Hyperbolic Equations," *Comm. Pure and Applied Math*, Vol. 31, 1978, pp. 423-430.

19. Shu, C. W., "Numerical Solutions of Conservation Laws," Ph. D. Dissertation, UCLA, 1986.

20. Donat, R. and Osher, S., "Propagation of Error in Regions of Smoothness for Nonlinear Approximations to Hyperbolic Equations," *Computer Methods in Applied Mechanics and Engineering*, Vol. 80, 1990, pp. 59-64.

21. Harten, A., "ENO Schemes with Subcell Resolution," *Journal of Computational Physics*, Vol. 83, 1989, pp. 148-184.

Table I. Steady-State Entropy Errors

ENO-4-3				
N_c	$\|\|e\|\|_1$	r_c	$\|\|e\|\|_\infty$	r_c
32	2.736 E-07		4.154 E-06	
64	1.800 E-08	3.93	4.370 E-07	3.25
128	1.085 E-09	4.05	3.671 E-08	3.57
256	6.372 E-11	4.09	2.697 E-09	3.77

Table II. L_∞ Pressure Errors for IBVP 2

ENO-4-3				
N_c	$x \leq 0.45$	r_c	$x \geq 0.55$	r_c
64	8.358 E-05		1.677 E-03	
128	6.540 E-06	3.68	1.392 E-04	3.59
256	4.758 E-07	3.78	3.087 E-05	2.17
512	4.511 E-08	3.40	1.689 E-05	0.87

Table III. Solution Errors for IBVP 3

ENO-4-3				
N_c	$\|\|e\|\|_1$	r_c	$\|\|e\|\|_\infty$	r_c
64	2.464 E-06		1.460 E-05	
128	1.665 E-07	3.89	9.783 E-07	3.90
256	1.038 E-08	4.00	6.108 E-08	4.00
512	6.383 E-10	4.02	3.759 E-09	4.02

Table IV. Solution Errors for IBVP 3

ENO-4-3				
N_c	$\|\|e\|\|_1$	r_c	$\|\|e\|\|_\infty$	r_c
65	2.924 E-05		9.217 E-05	
129	1.555 E-05	0.92	4.825 E-05	0.94
257	7.821 E-06	1.00	2.440 E-05	0.99
513	3.910 E-06	1.00	1.224 E-05	1.00

Table V. Solution Errors for IBVP 3

ENO-4-3-SR				
N_c	$\|\|e\|\|_1$	r_c	$\|\|e\|\|_\infty$	r_c
65	2.599 E-06		1.153 E-05	
129	1.552 E-07	4.11	8.644 E-07	3.78
257	9.772 E-09	4.01	5.703 E-08	3.94
513	6.132 E-10	4.01	3.628 E-08	3.99

Table VI. L_∞ Pressure Errors for IBVP 2

ENO-4-3-SR				
N_c	$x \leq 0.45$	r_c	$x \geq 0.55$	r_c
65	7.407 E-05		1.853 E-03	
129	5.665 E-06	3.71	1.831 E-04	3.34
257	3.623 E-07	3.97	1.288 E-05	3.83
513	2.667 E-08	3.76	8.266 E-07	3.96

FIGURES

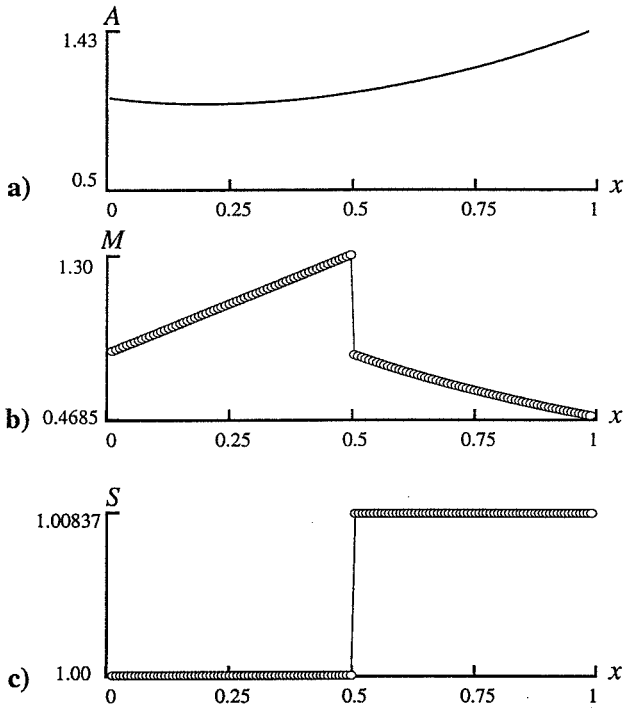

Figure 1: a) Nozzle area. b) Mach number, ENO-4-3.
c) $S = P/\rho^{\gamma}$, ENO-4-3.

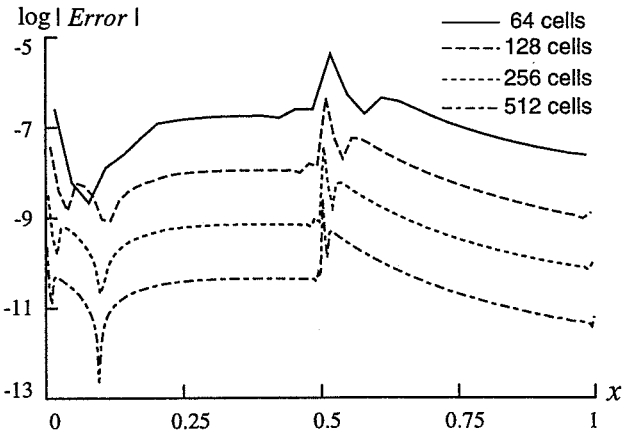

Figure 2: Quasi-1D Nozzle: Entropy error, ENO-4-3.

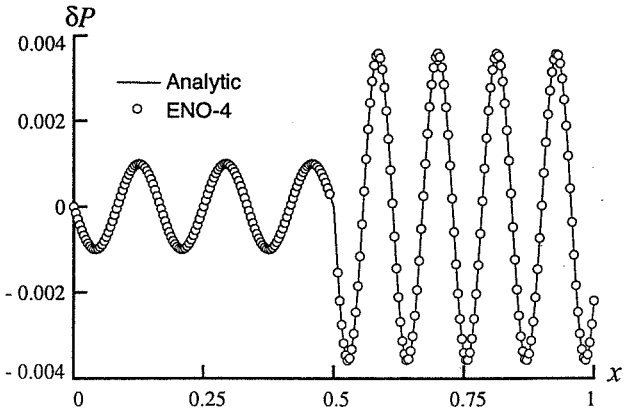

Figure 3: Solution of the sound-shock interaction problem at $t = 30\,T_{\lambda}$, ENO-4-3.

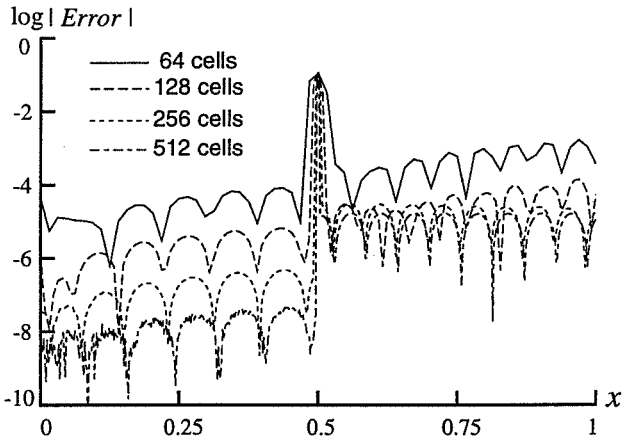

Figure 4: Pointwise error for the sound-shock interaction problem, ENO-4-3.

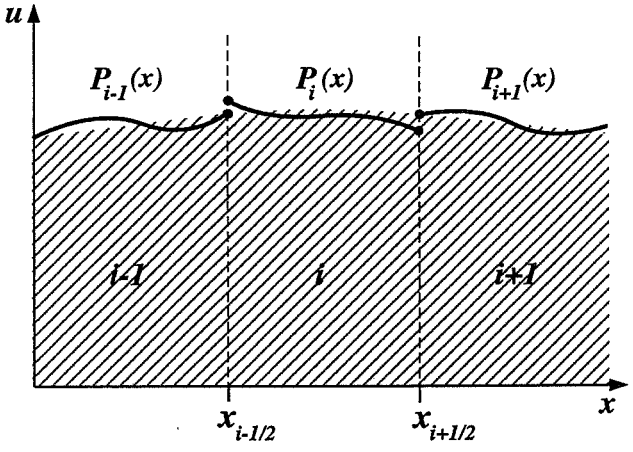

Figure 5: Piecewise polynomial reconstruction. Fluxes are determined by point values at cell faces.

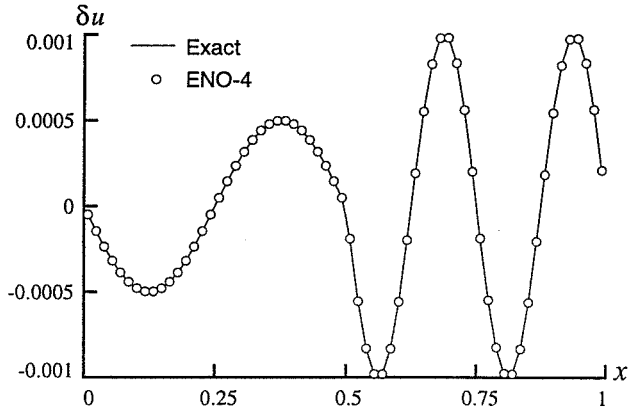

Figure 6: Solution of the IBVP 3 at $t = 10\,T_\lambda$, ENO-4-3.

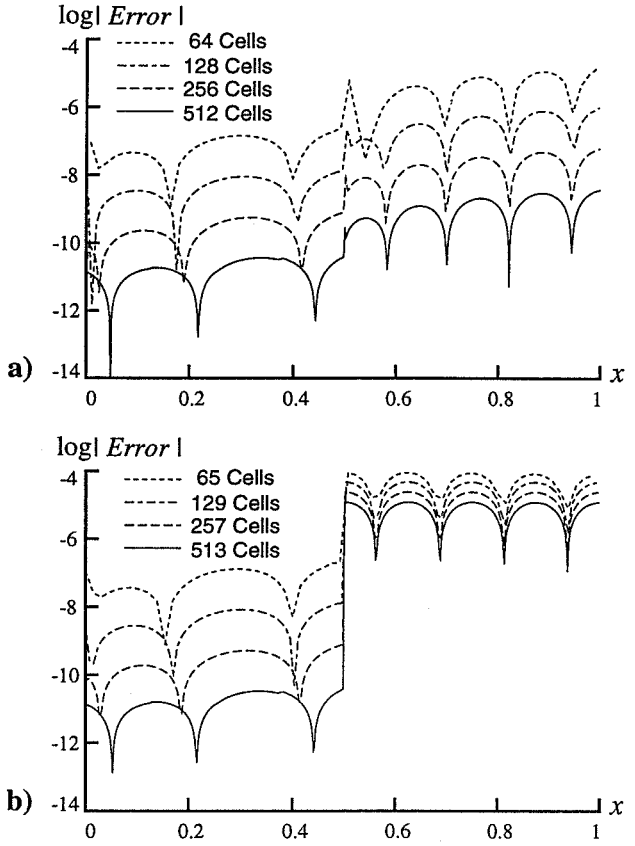

Figure 7: Pointwise error for the IBVP 3, ENO-4-3. a) Discontinuity on a grid point. b) Discontinuity within a cell.

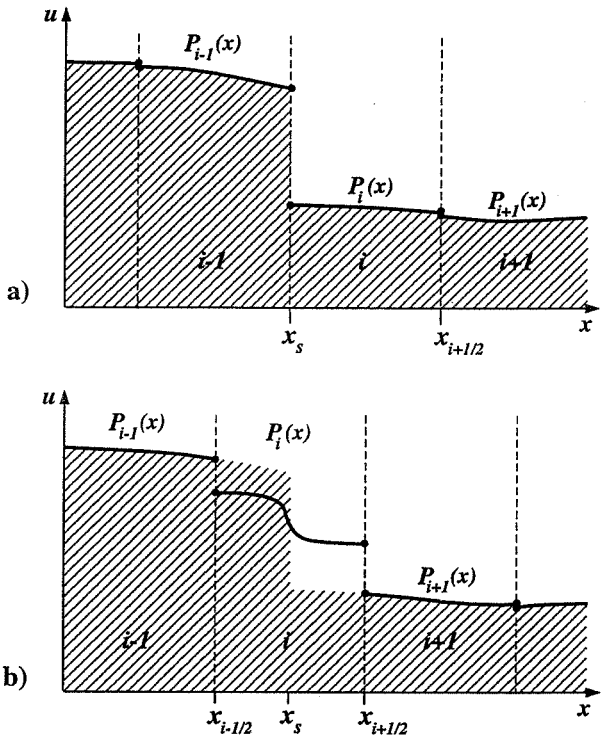

Figure 8: Piecewise polynomial reconstruction for the solution of IBVP 3. a) Discontinuity on a grid point. b) Discontinuity within a cell.

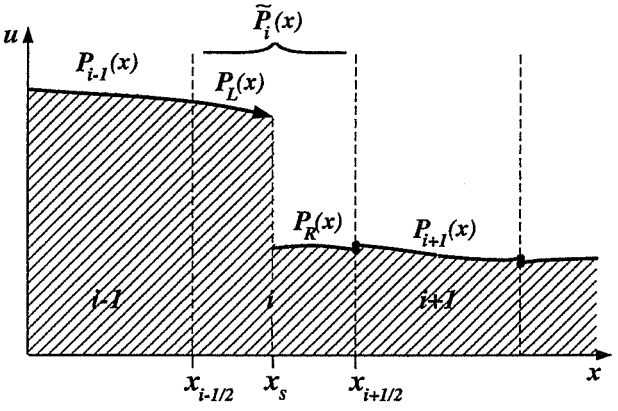

Figure 9: Piecewise polynomial reconstruction for Figure 8b, modified with subcell resolution.

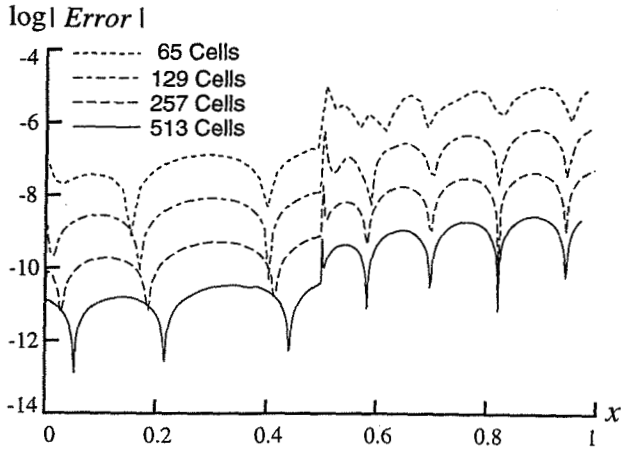

Figure 10: Pointwise error for the IBVP 3 with the discontinuity within a cell, using ENO-4-3-SR.

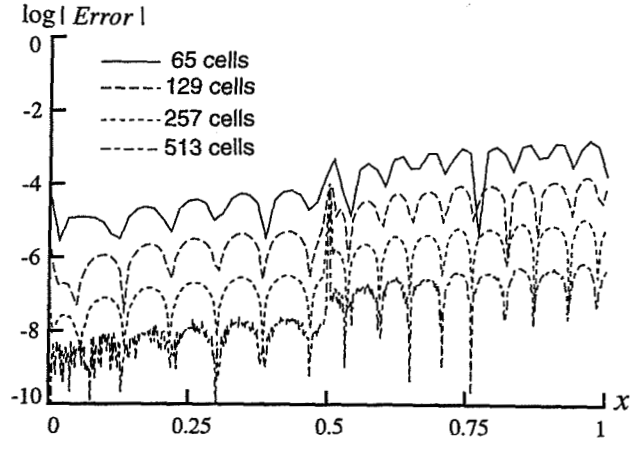

Figure 11: Pointwise error for the sound-shock interaction problem, using ENO-4-3-SR.

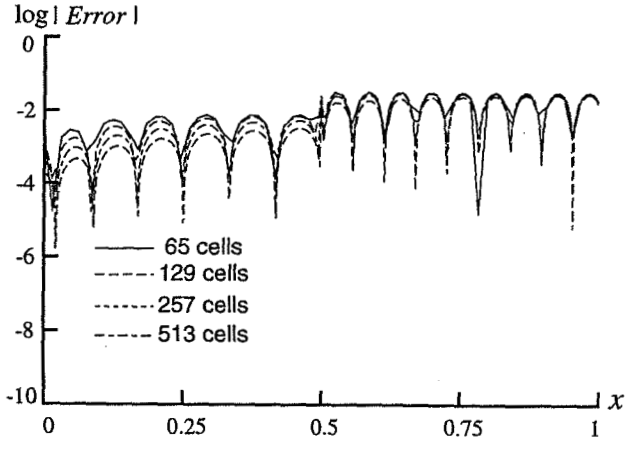

Figure 12: Pointwise error for the sound-shock interaction problem, using a first-order upwind method.

USING HIGH-ORDER METHODS ON LOWER-ORDER GEOMETRIES

Jay Casper
Aerospace Engineering Department
Old Dominion University
Norfolk, Virginia

ABSTRACT

The desire to obtain acoustic information from the numerical solution of a nonlinear system of equations is a demanding proposition for a computational algorithm. High-order accuracy is required for the propagation of high-frequency, low-amplitude waves. The accuracy of an algorithm can be compromised by low-order errors that naturally occur in the solution of a particular problem. Such errors arise from two sources: the presence of discontinuities in the flow field or because the geometry on which the problem is defined is not everywhere smooth to the order of the scheme. The performance of high-order accurate essentially non-oscillatory (ENO) schemes on piecewise smooth solutions is well documented. Herein, the performance of these methods on smooth solutions defined on piecewise smooth geometries is investigated. The propagation of sound in a quasi-one-dimensional nozzle is considered as a test case. Some of the issues involved in the extension to two spatial dimensions are discussed.

NUMERICAL METHOD

For the sake of brevity, the necessary details of the ENO schemes to be used in this work are presented within the context of a one-dimensional scalar equation,

$$\frac{\partial}{\partial t}u + \frac{\partial}{\partial x}f(u) = 0 \tag{1}$$

A control-volume formulation is obtained by integrating Eq. 1 on an interval $[x_{i-1/2}, x_{i+1/2}]$ with center x_i and "volume" Δx_i. The one-dimensional scalar conservation law can then be written

$$\frac{\partial}{\partial t}\bar{u}_i(t) = \frac{-1}{\Delta x_i}\Big[f(\,u(x_{i+1/2},t)\,) - f(\,u(x_{i-1/2},t)\,)\Big] \tag{2}$$

where

$$\bar{u}_i(t) = \frac{1}{\Delta x_i}\int_{x_{i-1/2}}^{x_{i+1/2}} u(x,t)\,dx \tag{3}$$

is the cell average of u on the i-th interval at time t. Temporal integration of Eq. 2 is accomplished by one of the Runge-Kutta methods of Shu and Osher (1988). The right-hand side of Eq. 2 is approximated in a manner similar to that introduced by Harten et al. (1987). A brief description follows.

To approximate the right-hand side of Eq. 2 to high-order accuracy, the spatial operator must include a high-order pointwise approximation to $u(x,t)$. However, at a given time t, only the cell averages in Eq. 3 are available. Therefore, a pointwise "reconstruction" of the solution from its cell averages is required. To this end, let R be an operator which reconstructs the cell averages and yields a piecewise polynomial $R(x\,;\bar{u}(t))$ of degree $r-1$ which approximates $u(x,t)$ to high order, wherever $u(x,t)$ is sufficiently smooth. This operator R acts in a piecewise manner in that the solution is locally reconstructed within each cell. Let $\mathcal{P}_i$ denote the polynomial of degree $r-1$ which approximates $u(x,t)$ in the i-th cell, at time t, i.e.

$$\begin{aligned}\mathcal{P}_i(x) &\equiv R(x;\bar{u}(t))\,, \quad x_{i-1/2} \le x \le x_{i+1/2} \\ &= u(x,t) + O(h^r)\end{aligned} \tag{4}$$

where $h = \max_i\{\Delta x_i\}$. The specific method used in this work is the "reconstruction by primitive" proposed by Harten et al. (1987) and is not detailed here.

This piecewise reconstruction can cause jumps in the approximate solution at the cell interfaces that are $O(h^r)$ in smooth regions and $O(1)$ near discontinuities. The fluxes in Eq. 2 are approximated by solving the local Riemann problems at the cell interfaces. Thus,

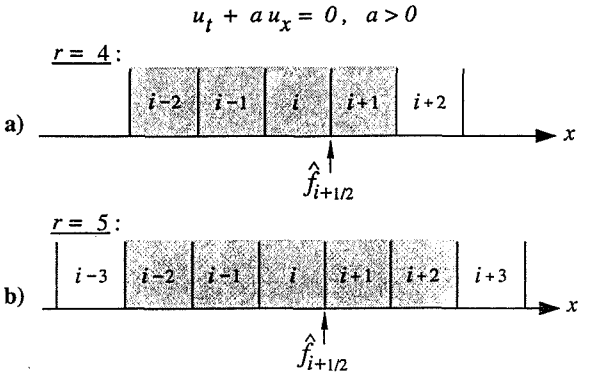

Figure 1: Preferred reconstruction stencils that result in fluxes that are a) one cell upwind and b) one-half cell upwind.

the right-hand side of Eq. 2 is replaced by its high-order approximation, which yields

$$\frac{\partial}{\partial t}\bar{u}_i(t) = \frac{-1}{\Delta x_i}\left[\hat{f}_{i+1/2}(t) - \hat{f}_{i-1/2}(t)\right] \qquad (5a)$$

where

$$\hat{f}_{i+1/2}(t) = f^{\mathrm{Rm}}(\,\mathcal{P}_i(x_{i+1/2})\,,\,\mathcal{P}_{i+1}(x_{i+1/2})\,) \qquad (5b)$$

and $f^{\mathrm{Rm}}(u_L, u_R)$ denotes the flux that is associated with the solution of the Riemann problem whose initial states are u_L and u_R. Upon temporal integration with an appropriately high-order Runge-Kutta method, the scheme in Eq. 5 is locally r-th-order accurate in the L_1 sense (Harten et al., 1987). The extensions of these schemes to hyperbolic systems and multiple dimensions that are discussed in this work were developed by Harten et al. (1987) and Casper and Atkins (1993).

The most unique aspect of the reconstruction operator R is its use of adaptive stenciling. That is, the interpolation set used for the approximation of $u(x,t)$ within a given cell is allowed to shift in an attempt to use the smoothest possible information. In this way, ENO schemes can approximate the smooth regions of a piecewise continuous function to high-order accuracy without the oscillatory behavior that is associated with interpolation across steep gradients. Furthermore, adaptive stenciling enables high-resolution shock-capturing. Previous research has shown that the accuracy of these schemes can degenerate when the stencils are allowed to freely adapt (Rogerson and Meiberg, 1990). Further research indicates that this accuracy problem can be remedied by biasing the stencils toward those that are linearly stable (Shu, 1990; Atkins, 1991). For present purposes, the desired reconstruction stencils are centered if r is odd and one cell upwind if r is even. In this manner, the resulting schemes have an upwind biased flux, as shown for the cases $r = 4$ and $r = 5$ in Figure 1.

It is important to note that the reconstruction-by-primitive operator R is not dependent on uniformity of the computational mesh. However, a rectangular mesh (or a smooth transformation to a rectangular mesh) is required for its extension to multiple dimensions (Casper and Atkins, 1993). Therefore, the ENO methods described above have a potentially important role to play in solving problems on cartesian meshes. In this work, the application of these methods to piecewise smooth geometries is considered.

ACOUSTIC WAVE IN A QUASI-ONE-DIMENSIONAL NOZZLE

The high-order ENO methods discussed above are now applied to the solution of an acoustic wave in a quasi-one-dimensional converging-diverging nozzle. The governing equations are the quasi-one-dimensional Euler equations:

$$\frac{\partial}{\partial t}(AU) + \frac{\partial}{\partial x}(AF) = H \qquad (6a)$$

where

$$U = \begin{bmatrix} \rho \\ \rho u \\ \rho E \end{bmatrix}, \; F = \begin{bmatrix} \rho u \\ \rho u^2 + P \\ (\rho E + P)u \end{bmatrix}, \; H = \begin{bmatrix} 0 \\ P\frac{dA}{dx} \\ 0 \end{bmatrix} \qquad (6b)$$

The variables ρ, u, P, E, and A are the density, velocity, pressure, total specific energy, and nozzle area, respectively. The equation of state is

$$P = (\gamma - 1)\,\rho\,(E - \frac{1}{2}u^2)$$

where γ is the ratio of specific heats which is assumed to have a constant value of 1.4. The flow variables are normalized with respect to upstream stagnation conditions. The length scale is Δx with $-200 \le x \le 80$. The area distribution is given by:

$$A(x) = \begin{cases} A_0\,, & -200 \le x \le -100 \\ B_0 - B_1\cos(B_2 x)\,, & -100 \le x \le 19 \\ D_0 + D_1 x\,, & 19 \le x \le 80 \end{cases}$$

where $A_0 = 134$ and the parameters B_k and D_k are determined by requiring C^1 continuity at $x = -100$ and $x = 19$. The

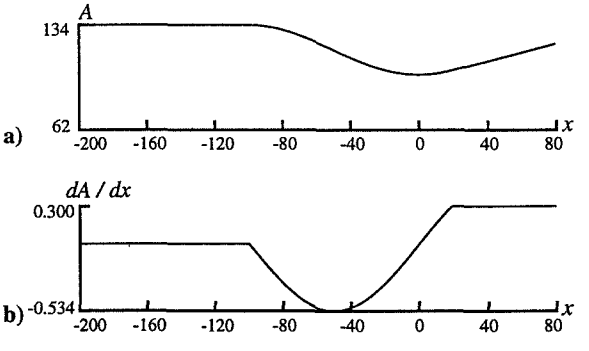

Figure 2: a) Nozzle area $A(x)$, and b) area derivative dA/dx.

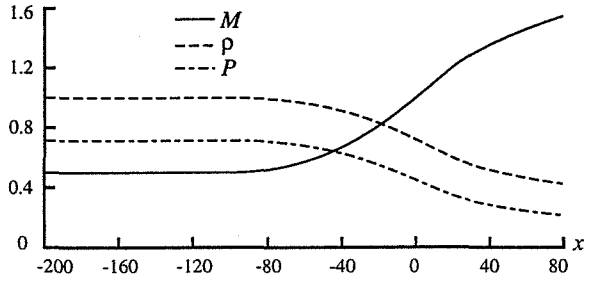

Figure 3: Initial steady-state solution.

prescribed area distribution $A(x)$ and its derivative are illustrated in Figure 2. This problem is taken from the test cases in (Hardin and Ristorcelli, 1995).

A steady-state solution is obtained by implementing a fourth-order ($r = 4$) ENO scheme until residuals are driven to machine zero. The stencils are everywhere biased toward the upwind stencil pictured in Figure 1a, including at the geometric discontinuities. Figure 3 illustrates the steady state solution on a mesh of 280 uniform cells. It should be noted that this numerically converged initial condition cannot be obtained with a freely adaptive stencil algorithm.

After the steady state is achieved, an acoustic disturbance is introduced at the inlet, $x = -200$:

$$
\begin{aligned}
P(t) &= P_i\,[\,1 + \epsilon \sin(\,\omega(\,x/(M+1) - t)\,)\,] \\
\rho(t) &= \rho_i \left[\frac{P(t)}{P_i}\right]^{1/\gamma} \\
u(t) &= u_i + \frac{2}{\gamma - 1}[\,c(t) - c_i\,]
\end{aligned}
$$

Here the subscript i denotes the steady inlet state, ω is the circular frequency, ϵ is the amplitude, and $c = \sqrt{\gamma P/\rho}$ is the local sound speed. The calculation is performed with $\omega = 0.1\pi$, $\epsilon = 10^{-6}$, and a Courant number of 0.5. Time-accurate, nonreflecting numerical boundary conditions (Atkins and Casper, 1994) are employed at inflow and outflow for both the initial steady solution and the time-dependent solution. The inflow is perturbed for $0 < t/T \leq 30$,

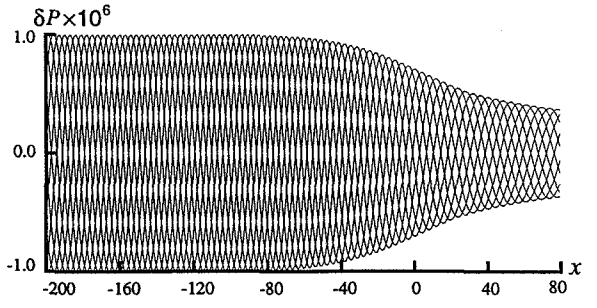

Figure 4: Envelop of pressure perturbation.

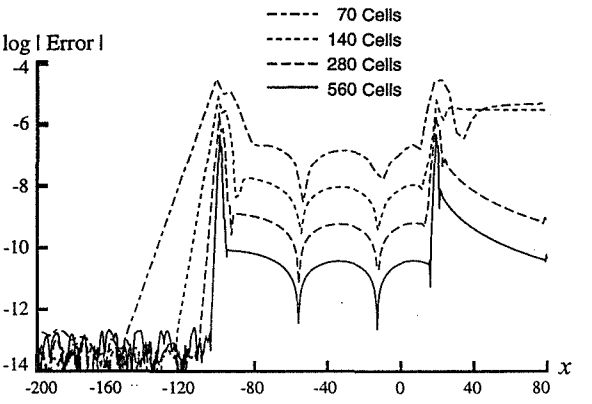

Figure 5: Entropy error of the acoustically perturbed nozzle, using uniform grid spacing.

where $T = 2\pi/\omega$ is one period of the incoming acoustic wave.

Figure 4 depicts the pressure perturbation $\delta P = P(x,t) - P(x,0)$ as a function of the nozzle length, at 10 equally spaced time intervals, during one period of the incoming acoustic wave, on a mesh of 280 cells. Figure 5 shows a grid refinement error study for the acoustically perturbed solution on four uniform meshes. The error in this figure is determined by deviation from isentropy and the plotted variable is δS, where $S = P/\rho^\gamma$. The error is only second order near $x = -100$ and $x = 19$, as expected, but is fourth order away from these points. The lower-order error arising from the geometry has remained local.

The above problem is now reworked, this time using mesh spacing that is discontinuous at the derivative discontinuities in the nozzle. Specifically, for a mesh of N cells, the grid spacing is determined by

$$
\Delta x_i = \begin{cases} 100/N_1\,, & -200 < x_i < -100 \\ 119/N_2\,, & -100 < x_i < 19 \\ 61/N_3\,, & 19 < x_i < 80 \end{cases} \qquad (7)
$$

where $N_1 = N/2$, $N_2 = 5N/14$, and $N_3 = N/7$. This mesh spacing is compared to uniform spacing for $N = 280$ in Figure 6. The staggered mesh is more highly resolved in the upstream region,

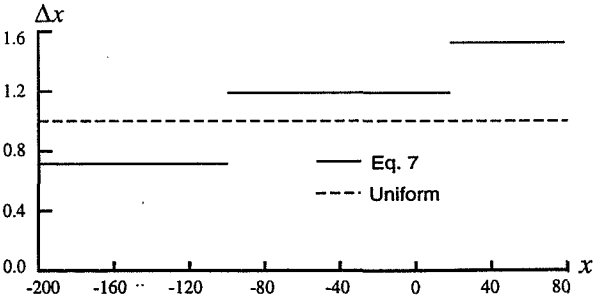

Figure 6: Mesh spacing with 280 cells.

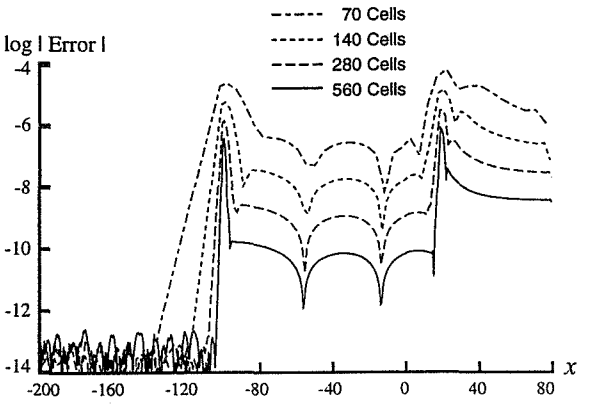

Figure 7: Entropy error of the acoustically perturbed nozzle, using staggered grid spacing.

and less resolved downstream than in the uniform case. This stands to reason for this problem, as the acoustic wavelength becomes longer in the streamwise direction, as the mean flow expands. Figure 7 shows the entropy error for the acoustically perturbed solution on four meshes determined by Eq. 7. The solution error in this figure is qualitatively similar to that on the uniform meshes in Figure 5. Again, the lower-order error at the geometric discontinuities remains local.

This problem is again worked on the staggered mesh in Eq. 7, this time using stencil adaptation near the geometric discontinuities. That is, the operator R is not permitted to interpolate across $x = -100$ or $x = 19$, and therefore the stencils are forced to be one-sided near these points. The entropy error for the acoustically perturbed solution in this case is shown in Figure 8. This plot is virtually indistinguishable from Figure 7, even though the stencils are clearly different, as shown in Figure 9. The pictured stencils are those used in the cubic polynomial interpolation of the characteristic variable associated with the eigenvalue $\lambda = u + c$. The variable plotted in Figure 9 is the stencil offset $j(i) - j_S(i)$, where $j(i)$

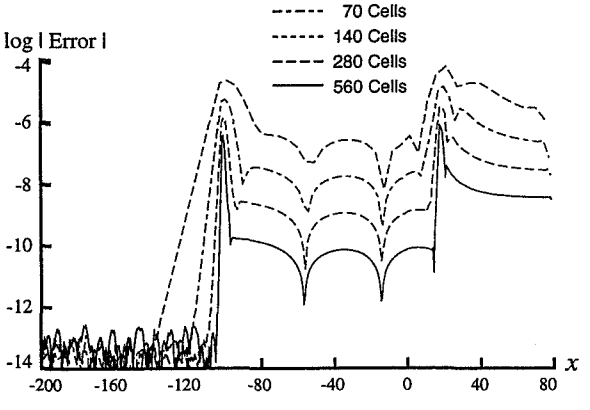

Figure 8: Entropy error of the acoustically perturbed nozzle, using staggered grid spacing and grid-adaptive stencils.

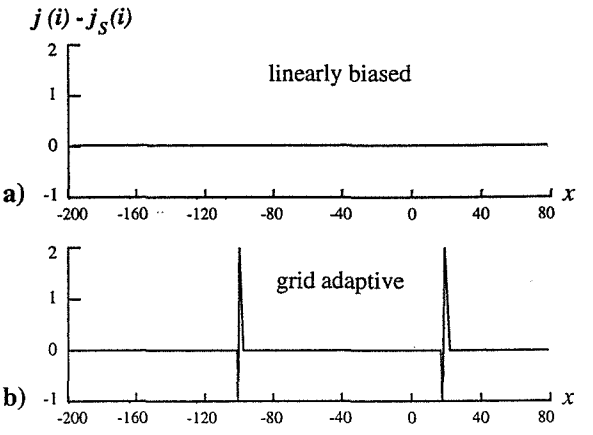

Figure 9: Stencils for the characteristic variable associated with $\lambda = u + c$.

is the left-most stencil index and $j_S(i)$ is the left-most index of the linearly stable stencil. For the present problem, the value of $u + c$ is always positive. Therefore, $j_S(i) = i - 2$ as in Figure 1a. A negative value of this offset represents a further upwind-shifted stencil, and a positive value represents a downwind-shifted stencil.

Given the insignificant difference in Figures 7 and 8, one might question the need for the geometric stencil adaptation, being that it adds to coding complexity while apparently gaining nothing in accuracy. This point is well taken for one-dimensional problems. However, the ability to geometrically adapt stencils without losing accuracy becomes important for multi-dimensional problems, to be discussed in the following section. Another question arises as to the stability of the scheme when some of the stencils are shifted downwind. The stability of a fourth-order upwind scheme with one-sided stencils near a boundary has been demonstrated by Atkins and Shu (1995).

TWO-DIMENSIONAL IMPLEMENTATION

A solution is desired to the scalar hyperbolic equation

$$u_t + f(u)_x + g(u)_y = 0 \tag{8}$$

Let the set $\{ C_{ij} \}$, where

$$C_{ij} = [x_{i-1/2}, x_{i+1/2}] \times [y_{j-1/2}, y_{j+1/2}]$$

denote a rectangular partition of the x-y plane, with (x_i, y_j) denoting the centroid of each rectangle. With a semi-discrete formulation in mind, a weak solution of Eq. 8 must satisfy

$$\frac{\partial}{\partial t} \bar{\bar{u}}_{ij}(t) = -\frac{1}{a_{ij}} \left[\begin{array}{l} f_{i+1/2,j}(t) - f_{i-1/2,j}(t) \\ + g_{i,j+1/2}(t) - g_{i,j-1/2}(t) \end{array} \right] \tag{9}$$

where $a_{ij} = \Delta x_i \, \Delta y_j$ is the area of C_{ij}, and

$$\bar{\bar{u}}_{ij}(t) = \frac{1}{a_{ij}} \int_{x_{i-1/2}}^{x_{i+1/2}} \int_{y_{j-1/2}}^{y_{j+1/2}} u(x, y, t) \, dx \, dy \tag{10}$$

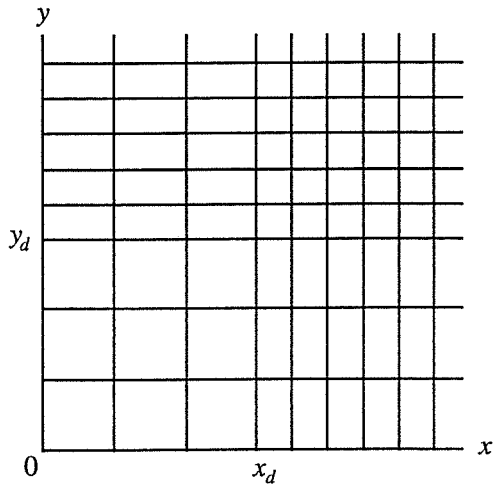

Figure 10: Discontinuous mesh spacing which requires no grid-based stencil adaptation.

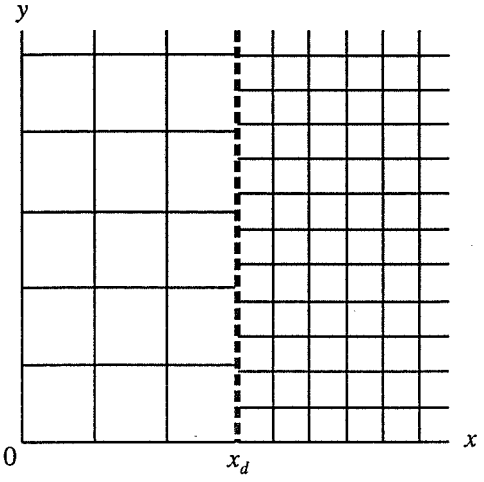

Figure 11: Discontinuous mesh spacing which requires grid-based stencil adaptation.

is the cell average of u in $\mathcal{C}_{ij}$ at time t. The fluxes are

$$f_{i+1/2,j}(t) = \int_{y_{j-1/2}}^{y_{j+1/2}} f(\,u(x_{i+1/2}\,,\,y\,,\,t)\,)\,dy \quad (11a)$$

$$g_{i,j+1/2}(t) = \int_{x_{i-1/2}}^{x_{i+1/2}} g(\,u(x\,,\,y_{j+1/2}\,,\,t)\,)\,dx \quad (11b)$$

As in the one-dimensional case, it is necessary to reconstruct the solution pointwise from the cell averages given by Eq. 10. The two-dimensional extension of the reconstruction-by-primitive operator is denoted by R^2 and is a product of two one-dimensional operators. On each cell $\mathcal{C}_{ij}$, the solution $u(x,y,t)$ is approximated by a polynomial $\mathcal{P}_{ij}$,

$$\begin{aligned} \mathcal{P}_{ij}(x,y) &\equiv R^2(x,y\,;\bar{\bar{u}}(t))\,, \quad x,\,y\,\in\,\mathcal{C}_{ij} \\ &= R(x\,;\,(\,R(y\,;\bar{\bar{u}}(t))\,)) \\ &= u(x,y,t)\,+\,O(h^r) \end{aligned} \quad (12)$$

where $h = \max_{i,j}\{\Delta x_i, \Delta y_j\}$.

The fluxes in Eq. 11 are computed as follows. The integration in Eq. 11 is approximated by an appropriate quadrature formula. The polynomials $\{\,\mathcal{P}_{ij}\,\}$ that are determined by the reconstruction in Eq. 12 are evaluated at the chosen quadrature points along each cell interface. Pointwise fluxes analogous to the one-dimensional flux in Eq. 5b are then computed at each quadrature point and then appropriately weighted and summed. The details of this two-dimensional method, as well as its extension to systems of conservation laws, can be found in (Casper and Atkins, 1993) and are not repeated here.

It is common practice to decompose a computational domain into subdomains when solving multi-dimensional problems on complex geometries or when efficiency demands that solutions of such problems require several levels of local grid resolution. Furthermore, it is often inconvenient, if not cost prohibitive, to connect these subdomains in a manner that is in keeping with a high-order accurate flow solver. The nature of such problems has prompted the development of more generalized versions of high-order accurate finite-volume methods for unstructured geometries (Barth and Fredrickson, 1991; Harten and Chakravarthy, 1991; Abgral, 1991). Depending on the application, these generalized methods can be quite complex and expensive. Of particular concern is an efficient method of stencil adaptation, although some recent progress has been made (Suresh and Jorgenson, 1995).

It is, therefore, of present interest to investigate the use of high-order methods which can be applied to piecewise rectangular meshes. The implementation of the reconstruction operator R^2 as a product of two one-dimensional operators greatly benefits the efficiency of the scheme, relative to the more generalized approach required for unstructured meshes. The structured natured of a rectangular mesh allows for more efficient coding. Furthermore, the stencil search is more straight forward, as a choice is made in each coordinate direction (Casper and Atkins, 1993).

Three cases of two-dimensional, discontinuous, rectangular meshes are considered. The first is one in which the mesh spacing Δx_i is discontinuous in x, but continuous in y, and Δy_j is discontinuous in y, but continuous in x, as pictured in Figure 10. In this case, there is no need to shift stencils away from $x = x_d$ or $y = y_d$, as the grid is fully connected. A solution on this mesh can be computed to high-order accuracy, disregarding the discontinuities in Δx_i and Δy_j, analogous to the one-dimensional case in the previous section.

Figure 11 depicts a mesh which differs from that in Figure 10

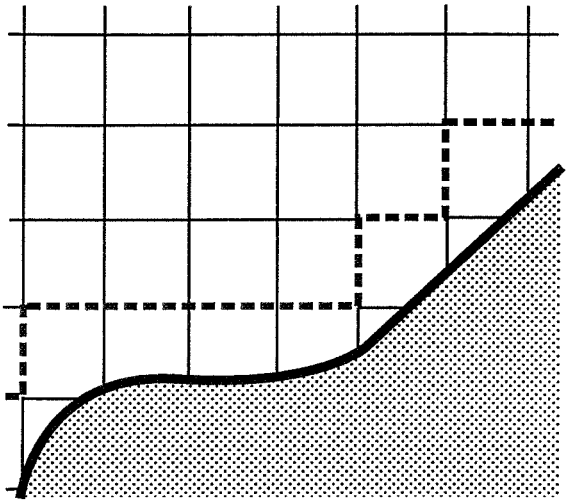

Figure 12: A geometry which requires grid-based stencil adaptation in addition to generalized reconstruction along the boundary.

in that Δy_j is discontinuous in x. In this case, the reconstruction operator R^2 cannot use information on both sides of $x = x_d$ in a straight forward manner. Therefore, the forcing of one-sided stencils near the interface (dashed line) appears to be a more prudent application. The flux integrals in Eq. 11a must be distributed over the subintervals into which a larger cell face is divided by smaller adjoining cells.

Perhaps the most common type of mesh discontinuity encountered when solving problems on rectangular grids is pictured in Figure 12. The mesh must abruptly terminate at a curvilinear boundary, making cells of non-rectangular shape near the boundary. In this case, two different reconstruction methods need be applied. The rectangular operator R^2 can be applied interior to the mesh interface (dashed line). However, near the boundary, the more generalized reconstruction (Harten and Chakravarthy, 1991) must by implemented, as the mesh is unstructured in this region. Again, the fluxes must be appropriately distributed amongst adjoining cells. Furthermore, the fluxes along the boundary must take into account the boundary's curvature (Casper and Atkins, 1993).

CONCLUDING REMARKS

ENO methods that employ reconstruction-by-primitive operators can be useful in solving computational aeroacoustics problems on discontinuous meshes. The retention of accuracy has been demonstrated by the fourth-order results obtained in the solution of an acoustic wave in a quasi-one-dimensional nozzle. Suggestions have been made for the multi-dimensional application of these methods to piecewise smooth rectangular meshes. Multi-dimensional test cases must be investigated, however, in order to support these claims.

ACKNOWLEDGEMENT

The author acknowledges the support of NASA Langley Research Center in Hampton, Virginia, under Grant NAG1-1653.

REFERENCES

Abgrall, R., 1991, "Design of an Essentially Non-Oscillatory Reconstruction Procedure on Finite-Element Type Meshes," NASA Contractor Report 189574, ICASE Report No. 91-84.

Atkins, H., 1991, "High-Order ENO Methods for the Unsteady Navier-Stokes Equations," AIAA Paper 91-1557.

Atkins, H. and Casper, J., 1994, "Non-Reflective Boundary Conditions for High-Order Methods," *AIAA Journal*, Volume 32, No. 3, pp. 512-518.

Atkins, H. and Shu, C. W., 1995 "GKS and Eigenvalue Stability Analysis of High-Order Upwind Schemes," in preparation.

Barth, T. J. and Frederickson, P. O., 1990, "High-Order Solution of the Euler Equations on Unstructured Grids Using Quadratic Reconstruction," AIAA Paper 90-0013.

Casper, J. and Atkins, H. "A Finite-Volume High-Order ENO Scheme for Two-Dimensional Hyperbolic Systems," 1993, *Journal of Computational Physics*, Vol. 106, pp. 62-76.

Hardin, J. C. and Ristorcelli, J. R., eds., 1994, *Proceedings, ICASE/LaRC Workshop on Benchmark Problems in Computational Aeroacoustics*, Hampton, Virginia.

Harten, A., Engquist, B., Osher, S., and Chakravarthy, S., 1987, "Uniformly High Order Accurate Essentially Non-oscillatory Schemes III," *Journal of Computational Physics*, Vol. 71, No. 2, pp. 231-323.

Harten, A. and Chakravarthy, S., 1991, "Multi-Dimensional ENO Schemes for General Geometries," NASA Contractor Report 187637, ICASE Report No. 91-76.

Rogerson, A. and Meiberg, E., 1990, "A Numerical Study of the Convergence Properties of ENO Schemes," *Journal of Scientific Computing*, Vol. 5, No. 2, pp. 151-167.

Shu, C., "Numerical Experiments on the Accuracy of ENO and Modified ENO Schemes," 1990, *Journal of Scientific Computing*, Vol. 5, No. 2, pp. 127-150.

Shu, C. and Osher, S., "Efficient Implementation of Essentially Non-Oscillatory Shock-Capturing Schemes," 1988, *Journal of Computational Physics*, Vol. 77, No. 2, pp. 439-471.

Suresh, A. and Jorgenson, P. C. E. 1995, "Essentially Nonoscillatory (ENO) REconstructions via Extrapolation," AIAA Paper 95-0467.

COMPUTATIONAL CONSIDERATIONS FOR THE SIMULATION OF DISCONTINUOUS FLOWS

MARK H. CARPENTER
NASA Langley Research Center
Hampton, Virginia

AND

JAY H. CASPER
Old Dominion University
Norfolk, Virginia

Abstract.

The numerical study of aeroacoustic problems places stringent demands on the choice of a computational algorithm, because it requires the ability to propagate disturbances of small amplitude and short wavelength. The demands are particularly high when shock waves are involved, because the chosen algorithm must also resolve discontinuities in the solution. In a previous work [1] the capabilities and deficiencies of shock-capturing methods for aeroacoustic problems were demonstrated using a high-order essentially nonoscillatory (ENO) numerical method. It was shown that first-order results are obtained when simulating time-dependent flows with discontinuities. The present study reaffirms this conclusion by comparing the ENO results with those obtained using a conventional linear scheme.

A sixth-order-accurate compact implicit finite difference scheme is used to investigate various discontinuous flows. The design order of accuracy is achieved in the smooth regions of a steady-state, quasi-one-dimensional Euler test case, as well as in the time-dependent Burgers' equation. However, in the unsteady Euler sound-shock interaction, first-order results are obtained downstream of the shock. A comparison is made between the linear and nonlinear results, noting the advantages of each method. A discontinuous linear model problem is then used to identify the cause of the first-order results. Here, the nature of the solution error is quantified as being predominantly a numerical phase shift, and a post-processing procedure is demonstrated which increases the solution accuracy downstream of the discontinuity to second-order.

1. Introduction

This work is motivated by the desire to develop numerical methods that will be useful in the study of aeroacoustic phenomena that occur in flows with shocks. For example, shocks in jet flows, on wings, and in supersonic combustion inlets contribute significantly to sound generation. Problems such as these represent some of the more challenging aspects of ongoing research in the developing area of computational aeroacoustics (CAA). For a computational algorithm, obtaining acoustic information from a numerical solution that involves shock waves is a demanding proposition. In general, high-order accuracy is required for the propagation of high-frequency low-amplitude waves. In addition, the shock must be adequately captured.

In reference [1], a discussion was opened on the relative merits of the numerical methods which can simulate sound sources that are generated in flows with shocks. A fourth-order essentially nonoscillatory (ENO) numerical scheme was used to demonstrate the nature of solution error for steady and unsteady cases. It was shown that the quasi-one-dimensional Euler equations, in the presence of a shock, admit a steady-state solution which is of design order-of-accuracy. The time-dependent Euler equations revert to first-order accuracy downstream of the shock. The magnitude of the error, however, is much larger when using a uniformly first-order scheme.

Given the apparent inability of nonlinear schemes to recover design accuracy downstream of an unsteady shock, one must reassess the potential benefits of nonlinear schemes relative to linear schemes. In this work we begin to open the discussion on the relative merits of linear and nonlinear schemes for discontinuous flows. In addition, we identify a larger class of problems for which design accuracy can be obtained. Finally, we quantify the nature of the solution error downstream of a discontinuity when design accuracy is not obtained.

In the following sections, we introduce a fourth-order-accurate essentially nonoscillatory (ENO) method and a sixth-order compact method, and then use them to simulate a steady-state nozzle flow with a shock. In both cases design accuracy is obtained away from the discontinuity. It is then shown, using Burgers' equation, that design accuracy can be achieved in the time-dependent case, even for nonlinear equations. We then show that accuracy suffers if either numerical scheme is used on the time-dependent sound-shock interaction problem. The disappointing results in regard to the accuracy of this solution are explained through the study of a simpler linear model problem. The solution error is quantified as being phase error, to leading truncation order. We demonstrate in the linear case that post-processing the numerical solution, with the explicit knowledge of the phase error, increases the solution error to second order. Some of the difficult is-

sues and ramifications for current methods that are raised by these results are discussed in the final section.

2. High-Order Accurate Shock-Capturing

Many methods are available in the literature that attempt to balance the properties of high-order accuracy and shock capturing. They can be classified into two categories : linear and nonlinear. We will not attempt to describe the details of either class of numerical methods, and refer those who are interested to a more complete discussion in reference [1]. Rather, we present only a brief theoretical review of linear and the nonlinear strategies.

Within the linear class of numerical shock-capturing schemes, the interpolation set for the approximation of the solution or its derivatives is fixed as a function of grid location. Linear methods admit strong oscillations in regions in which physical gradients are inadequately resolved. Central-differencing operators and spectral methods are particularly prone to these numerical oscillations. For problems with discontinuities, limiters or filters are usually required to keep oscillations from growing without bound.

In the nonlinear class of schemes, the strategy with respect to discontinuities is to employ some sort of adaptive interpolation. The goal is to achieve formal high-order accuracy in smooth regions and high shock resolution without oscillations. The class of ENO schemes [2] - [3] has been designed to have such properties. As originally presented, the local polynomial approximation operator adapts its interpolation set to the smoothest available part of the solution.

Although discontinuous solutions generated by a linear strategy are usually not as pictorially pleasing as solutions in which shock profiles are monotone, linear schemes are more computationally efficient than nonlinear schemes. The efficiency of a numerical algorithm is extremely important for aeroacoustic simulations because such problems are time dependent and require a fine computational mesh for the resolution of high-frequency disturbances. Because nonlinear methods are designed to avoid the production of spurious oscillations, the stability of a calculation of a flow with shocks is more readily obtained. However, their adaptive interpolation operator significantly hampers their efficiency relative to linear schemes.

3. Steady Shock in a Nozzle

A steady-state flow with a shock in a quasi-one-dimensional converging-diverging nozzle is numerically investigated. The governing equations are

the quasi-one-dimensional Euler equations:

$$\frac{\partial}{\partial t}(AU) + \frac{\partial}{\partial x}(AF) = G \tag{1a}$$

where

$$U = \begin{bmatrix} \rho \\ \rho u \\ \rho E \end{bmatrix}, \; F = \begin{bmatrix} \rho u \\ \rho u^2 + P \\ (\rho E + P)u \end{bmatrix}, \; G = \begin{bmatrix} 0 \\ P\frac{dA}{dx} \\ 0 \end{bmatrix} \tag{1b}$$

The variables ρ, u, P, E, and A are the density, velocity, pressure, total specific energy, and nozzle area, respectively. The equation of state is

$$P = (\gamma - 1)\,\rho\,(E - \frac{1}{2}u^2)$$

where γ is the ratio of specific heats, which is assumed to have a constant value of 1.4.

The spatial domain of the nozzle is $0 \leq x \leq 1$. The nozzle shape is determined exactly through the requirement of a linear distribution of Mach number from $M = 0.8$ at the inlet to $M = 1.8$ at the exit, assuming the flow is isentropic and fully expanded. A schematic of the area distribution can be found elsewhere [1].

Given the prescribed area distribution, the Mach 0.8 inflow state is retained at $x=0$, and the outflow condition at $x=1$ is determined such that a shock forms at $x_s = 0.5$, which corresponds to a preshock Mach number of $M = 1.3$. Steady-state solutions are obtained by implementing a fourth-order accurate finite-volume ENO scheme and a sixth-order finite-difference scheme until residuals are driven to machine zero. In the ENO algorithm, the spatial accuracy is achieved by solving the equations in control-volume form as presented in Ref. [2]. The equations are integrated in time via a third-order-accurate Runge-Kutta scheme [3]. This numerical method will be referred to as "ENO-4-3." As has been established in previous research, [4] - [7] the adaptive stencils employed in the spatial operator are biased in smooth regions toward those that are linearly stable.

The finite-difference algorithm uses a compact implicit spatial operator, shown elsewhere to be time-stable and spatially a sixth-order accurate discretization [8]. A small amount of background tenth-order numerical dissipation was added to stabilize the calculation. No explicit filtering is needed in these calculations. The time advancement scheme is a five stage fourth-order low-storage RK scheme [9]. This scheme which is formally sixth-order in space and fourth-order in time will be referred to as the "LIN-6-4" scheme.

One of the simpler methods of determining the error of this solution relies on the fact that the value of the entropy-like quantity $S \equiv P/\rho^\gamma$ is

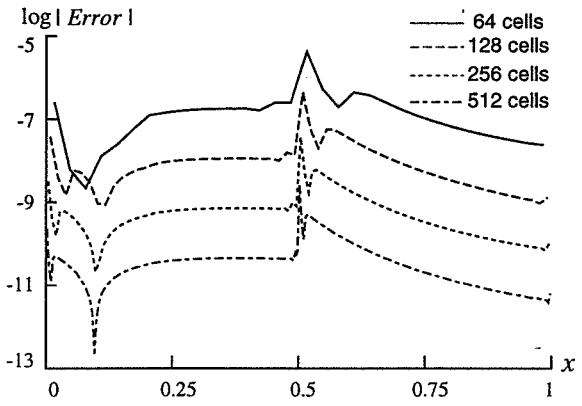

Figure 1. Quasi-1D Nozzle: Entropy error, ENO-4-3.

piecewise constant. The exact magnitude of the jump is known analytically. The pointwise entropy error for this solution on four successively refined meshes is illustrated in Fig. 1. It is evident from Fig. 1 that the accuracy is fourth order on either side of the shock (error decay by a factor of 16 with each grid doubling).

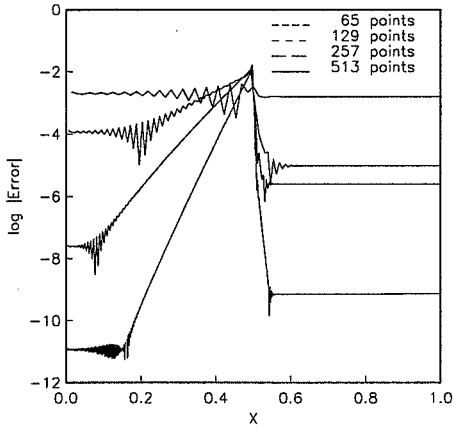

Figure 2. Quasi-1D Nozzle: Entropy error, LIN-6-4.

Fig. 2 shows the steady-state Entropy error as determined by the LIN-6-4 scheme. Note that an order one error always exists at the location of the discontinuity. This error which is not present in the ENO-4-3 results, is inherent in the linear scheme as a consequence of the Gibbs' oscillations. Away from the discontinuity the scheme converges at the design accuracy

of sixth-order. The ENO-4-3 scheme is considerably more accurate than the LIN-6-4 scheme on coarse grids, despite its lower formal accuracy. Similar results were obtained for test cases in which the shock location did not coincide with a grid point.

The time independence of the solution makes this a convenient example for the demonstration of high-order accuracy in the presence of a shock. Both the linear and nonlinear schemes were able to obtain higher-order accuracy away from the discontinuity, and the nonlinear schemes' behavior in the neighborhood of the shock was exceptionally good. We assert that these results are representative of linear and nonlinear schemes, and are general for the steady-state Euler equations in one spatial dimension. (The generalization to multiple spatial dimensions is not straightforward and is the topic of a forth-coming paper).

4. Time Dependent Interactions

A moving shock presents a greater challenge in regard to high-order-accurate shock capturing. As will be seen, many of the desirable attributes of the nonlinear schemes are lost in the time-dependent case. We begin our discussion with a simple test case in which the equation is nonlinear and supports a time-dependent discontinuity.

4.1. BURGERS' EQUATION

Studying Burgers' equation helps to clarify an important issue about solution accuracy in the presence of discontinuities. It is common to use Burgers' equation as a model problem to mimic the nonlinear nature of the Euler equations. The quadratic nonlinearity of the spatial flux in Burgers' equation is similar to the convective terms in the Euler equations. An assertion frequently implied in the literature is that solution error will be qualitatively similar for Burgers' equation and the Euler equations. We show by counter-example that the nature of the solution error for discontinuous flows is fundamentally different. Thus, Burgers' equations is of only limited value in studying time-dependent discontinuous flows.

In the absence of viscosity, Burgers' equation can be expressed as $\frac{\partial U}{\partial t} + \frac{1}{2}\frac{\partial U^2}{\partial x} = 0$. We employ initial conditions $U(x,0) = 1;\ 0 \leq x < \frac{1}{2}, U(x,0) = -1;\ \frac{1}{2} < x \leq 1$ and boundary conditions $U(0,t) = 1 + \epsilon sin(\omega_1 t);\ t \geq 0$, $U(1,t) = -1 + \epsilon sin(\omega_2 t);\ t \geq 0$. Here $\epsilon = 0.01$, $\omega_1 = 12\pi$, and ω_2 is related to ω_1 by a phase shift. A simulation using the LIN-6-4 scheme is run to a physical time $T = 10$. An "exact" solution is obtained using a two-domain Chebyshev discontinuity fitting code. Sufficient resolution in space and time is used to ensure that further refinement does not change

the interpolated solution on the uniform grid.

Large oscillations near the discontinuity can be observed in the numerical solution obtained with the LIN-6-4 scheme. Fig. 3 shows the pointwise error on four successive grids, plotted on a Logarithmic scale. Qualitatively, the solution error is similar to that obtained in the steady-state nozzle using the LIN-6-4 scheme. An order one error exists at the discontinuity, but the solution converges at the design rate of sixth-order on both sides of the discontinuity. We note here, and clarify later in this section, that this high-order behavior is not achieved in more general hyperbolic equations.

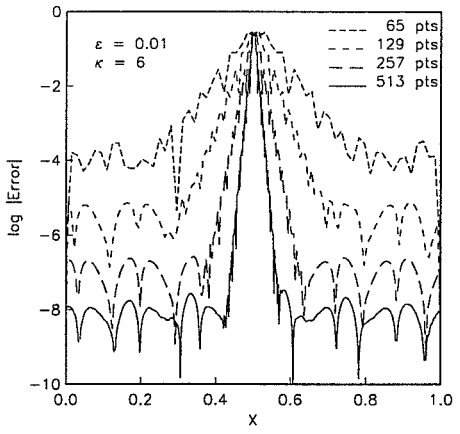

Figure 3. Burgers' equation: solution error, LIN-6-4.

4.2. SOUND-SHOCK INTERACTION

The effects of shocks on sound waves, (and vice versa), are important to the acoustics and performance of aircraft design. Therefore, the ability to obtain an accurate solution to such a model initial-boundary-value problem (IBVP) is important in the development of shock-capturing methods for CAA research.

The governing equations are the one-dimensional Euler equations:

$$\frac{\partial}{\partial t}U + \frac{\partial}{\partial x}F(U) = 0 \tag{2a}$$

where the components of U and $F(U)$ are identical to those given in Eq. 1b. The equation of state is also the same as in the previous example.

The spatial domain is $0 \leq x \leq 1$. The piecewise constant initial conditions, U_L and U_R, are those of a steady shock located at $x_s = 0.5$. The

flow is from left to right, and the state U_L is a Mach 2 flow upstream of the shock. The flow variables are normalized with respect to this upstream flow. At $t = 0$, an acoustic disturbance is introduced at $x = 0$:

$$\begin{aligned} P(0,t) &= P_L\,(1 + \epsilon \sin \omega t\,) \\ \rho(0,t) &= \rho_L \left[\frac{P(0,t)}{P_L}\right]^{1/\gamma} \\ u(0,t) &= u_L + \frac{2}{\gamma - 1}[\,c(0,t) - c_L\,] \end{aligned} \tag{2b}$$

where ω is the circular frequency, ϵ is the amplitude, and $c = \sqrt{\gamma P/\rho}$ is the local sound speed.

The numerical solution of this problem is obtained through the implementation of both the ENO-4-3 and the LIN-6-4 algorithms. Both algorithms should achieve their design spatial accuracy for a suitably small temporal step size. The exact solution is obtained by a two-domain Chebyshev spectral technique [9]. Shock fitting is used to divide the domain into two computational regions. A Chebyshev collocation method is used in each region for the spatial discretization. A fourth-order Runge-Kutta scheme is used to discretize time. Sufficient spatial and temporal resolution are used to guarantee machine precision of the solution.

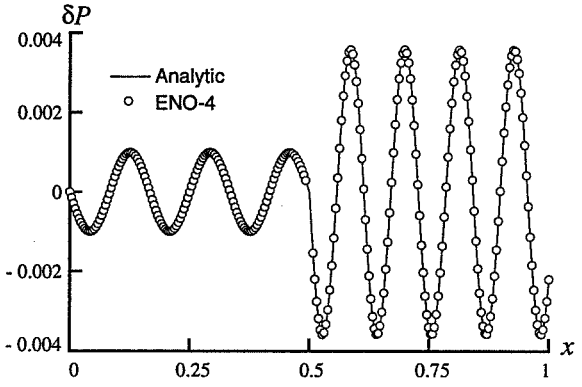

Figure 4. Solution of the sound-shock interaction problem at $t = 30\,T_\lambda$, ENO-4-3.

Fig. 4 depicts the pressure perturbation $\delta P(t) = P(x,t) - P(x,0)$ at $t = 30\,T_\lambda$, where $T_\lambda = 2\pi/\omega$ is one period of the incoming acoustic wave. The acoustic wave amplitude is $\epsilon = 0.001$, and $\omega = 2\pi k(u_L + c_L)$ is determined by requiring a wave number $k = 6$ with respect to unit length and a mean wave speed $u_L + c_L$. The calculation, represented by circles, was performed

on a uniform mesh of 256 cells and a Courant number of 0.5, with the ENO-4-3 code. The exact solution is represented by a continuous line. In this pictorial measure, the numerical algorithm performs well with respect to its prediction of the amplified sound wave at higher frequency downstream of the shock. The missing circle values near the shock are off the plot and are due to the use of the stencil-biasing parameters near a moving discontinuity.

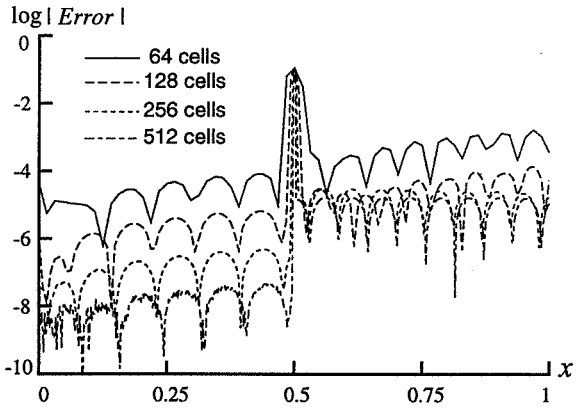

Figure 5. Pointwise error for the sound-shock interaction problem, ENO-4-3.

Even more instructive, however, is the pointwise error made by this calculation with respect to the mesh width. Fig. 5 illustrates this error on four successively refined meshes. The solution is clearly fourth-order accurate upstream of the shock, but only first-order downstream of the shock, as shown by the L_∞ error data in Table 1. The errors are computed on two spatial subdomains: $0 \leq x \leq 0.45$ and $0.55 \leq x \leq 1$. In this manner, the first-order error that is generated in the vicinity of the shock is avoided.

TABLE 1. L_∞ Pressure Errors : ENO-4-3

N_c	$x \leq 0.45$	r_c	$x \geq 0.55$	r_c
64	8.358 E-05		1.677 E-03	
128	6.540 E-06	3.68	1.392 E-04	3.59
256	4.758 E-07	3.78	3.087 E-05	2.17
512	4.511 E-08	3.40	1.689 E-05	0.87

Fig. 6 depicts the solution error for the sound-shock interaction problem, using the LIN-6-4 scheme. (Here, in addition to the tenth-order damping, the solution was filtered with a tenth-order filter every 5 time-steps). The qualitative features of the solution and its error are nearly identical to those obtained with the ENO-4-3 scheme. The order one error near the

discontinuity is a bit more localized in the ENO-4-3 case, but the magnitude of solution error downstream of the discontinuity is nearly the same. The design accuracy is obtained upstream of the discontinuity, but the solution accuracy is first-order downstream of the shock.

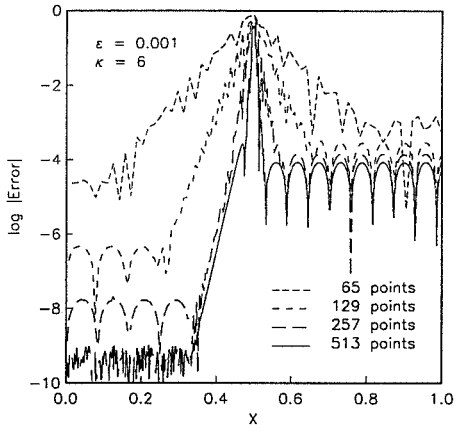

Figure 6. Pointwise error for the sound-shock interaction problem, LIN-6-4.

Comparing the error differences in the Euler and Burgers' equations can lend insight into when a first-order solution will occur at a time-dependent discontinuity. We begin by noting how error propagates in each respective equation. In Burgers' equations, all information propagates towards the discontinuity. Thus, error which is generated at the discontinuity is localized at the discontinuity. In the Euler equations, error that is generated at the discontinuity is swept downstream on the down running characteristics. (It can be shown that all information traveling towards the discontinuity is design-order accurate on both sides of the discontinuity, until nonlinear corruption occurs near the shock). Information traveling away from the discontinuity is first-order. All flow variables being combinations of the two, are no better than first-order accurate. Burgers' equation is not a good model problem for determining the error characteristics of a time-dependent numerical scheme.

The general observation that both linear and nonlinear schemes are first-order downstream of the shock raises considerable concern in regard to the use of high-order-accurate methods in the study of unsteady flows with shocks. If high-order methods only yield first-order results, why use them? Before this question can be fully answered, it must first be determined whether the first-order error from a high-order method is significantly smaller than that of a lower order method. Fig. 7 depicts the error

of the sound-shock interaction problem with a first-order upwind method. Upon comparison with the Fig. 5 or Fig. 6, it is clear that the solution downstream of the shock is more accurate when using either higher-order method. This result is by no means conclusive, as there are many other considerations. For instance, what about second- or third-order methods? What about the cost of using a given method with respect to its accuracy? These and a more general comparison of linear and nonlinear scheme are topics for future research.

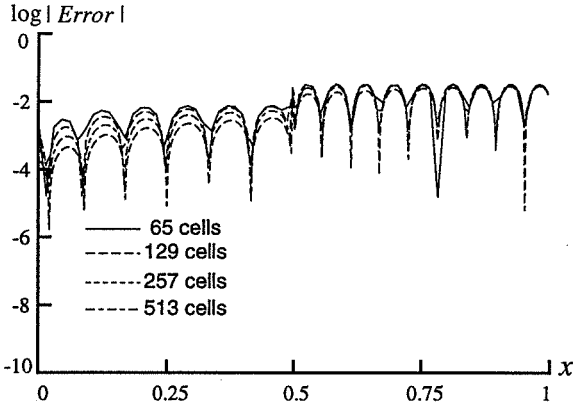

Figure 7. Pointwise error for the sound-shock interaction problem, using a first-order upwind method.

The first-order nature of the solution downstream of the discontinuity is difficult to study using the full Euler equations. In the next section, we construct a simple model problem which contains the underlying mechanism for the degradation to first-order accuracy.

5. A Linear Model Problem

The lower-order accurate results of the previous section can be analyzed through the study of a discontinuous linear scalar model problem, wherein we isolate the important phenomenon of propagation of information through a discontinuity. This trait will be common to almost any aeroacoustic problem that involves shock waves. Consider the scalar equation: $\frac{\partial u}{\partial t} + \frac{\partial [a(x)u]}{\partial x} = 0$, where the piecewise constant wave speed $a(x)$ is $a(x) = a_L\,, \quad x < \frac{1}{2}$ and $a(x) = a_R\,, \quad x > \frac{1}{2}$ on the interval $0 \leq x \leq 1$. (For the finite difference code, the jump value at $x = \frac{1}{2}$ is assigned to be the average of the left and right states.) The initial condition is given by $u(x,0) = \sin(\omega\, x)$ on $0 \leq x \leq 1$, and the boundary condition is $u(0,t) = \sin(\omega\, (-a_L t)$ at $x = 0,\ t \geq 0$. The constant ω is determined by requiring a wave number

$k = 4$ with respect to unit length and the downstream wave speed a_R. The exact solution is given at long times (times after the initial solution has swept out of the domain) by $u(x,t) = \sin[\omega\,(x - a_L t)]$ on the interval $0 \leq x \leq \frac{1}{2}$ and $u(x,t) = \frac{a_L}{a_R}\sin[\omega\,(\frac{a_L}{a_R}(x - \frac{1}{2}) - a_L t + \frac{1}{2}]$ on the interval $\frac{1}{2} \leq x \leq 1$. The exact solution is obtained by requiring conservation of fluxes at the interface.

The loss in accuracy in numerical solutions of linear problems with discontinuous initial data has been the subject of previous research by other authors [11] - [14]. All of these previous studies involved solutions of coupled linear systems. It is, therefore, instructive to note that the solution of this discontinuous linear problem is analogous to that of a coupled system in the following way. The flux conservation condition couples at the discontinuity location the equations in the left and right domains. The coupling occurs at a discrete point (like a boundary) and the information transfer is from one equation to the other. As in the present study, the work of Majda and Osher [11] was concerned with the inherent degradation in accuracy in a region where information is numerically propagated across a discontinuity.

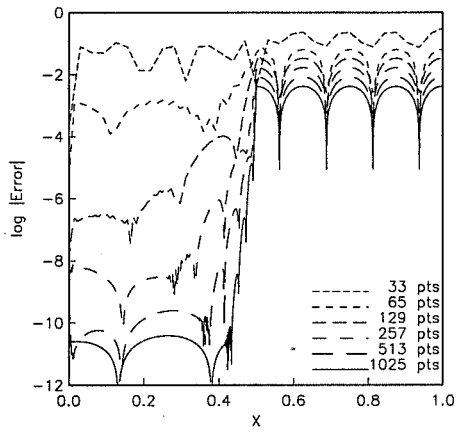

Figure 8. Pointwise error for discontinuous linear model problem run with LIN-6-4

Fig. 8 shows the pointwise error for the discontinuous linear model problem with a wave-speed ratio of $\frac{a_L}{a_R} = 2$. The simulation is run to time $T = 4$ on a series of six grids with the LIN-6-4 scheme. The solution is filtered every five time steps. As with the Euler equations, the solution accuracy is sixth-order upsteam, and first-order downstream of the discontinuity.

Inspection of the numerical solution downstream of the discontinuity reveals that the dominant component of the error is related to phase. Specifically, the amplitude of the waves downstream of the discontinuity is nearly

correct, but the waves are displaced by some fraction of the grid spacing. To quantify this behavior, the Fourier transform of the solution is formed on the interval $\frac{3}{4} \leq x \leq 1$. The exact transform of the downstream sine wave on the interval (made periodic by construction) is the $k = 1$ mode of unit amplitude. Fig. 9 plots the amplitude of the Fourier modes obtained from the numerical solution on this interval. The energy in the spurious higher modes decays very rapidly, indicating that the amplitude portion of the solution error is higher-order.

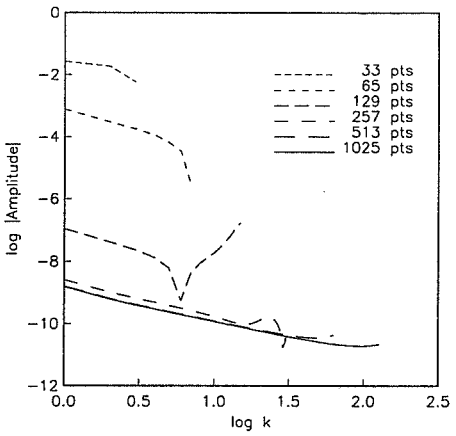

Figure 9. Solution error as a function of Fourier wave number k

The phase shift of the numerical solution as a percentage of grid spacing (as determined by the phase angle of the Fourier transform), asymptotes to a nonzero constant, however. For sufficient resolution, the numerical solution is shifted a finite percentage of the grid spacing, independent of the resolution. If the numerical solution is adjusted to account for this phase shift, then the solution error can be reduced. Fig. 10 plots the data shown in Fig. 8 where the exact solution downstream of the discontinuity is shifted by a constant multiple of the grid spacing. It is apparent that the solution accuracy is increased by this procedure. Unfortunately, the convergence rate downstream of the discontinuity is still only second-order and not the design order of six as would be expected with the LIN-6-4 scheme.

A more troubling observation about the numerical phase shift, is that the shift is amplitude dependent. Table 2. shows the dependence of the phase shift on the wave-speed ratio $\frac{u_L}{u_R}$. Multiple waves interact at a shock in the Euler equations, each having a different wave-speed ratio. To correct the multiple wave situation would require component by component shifting and would be more difficult to implement.

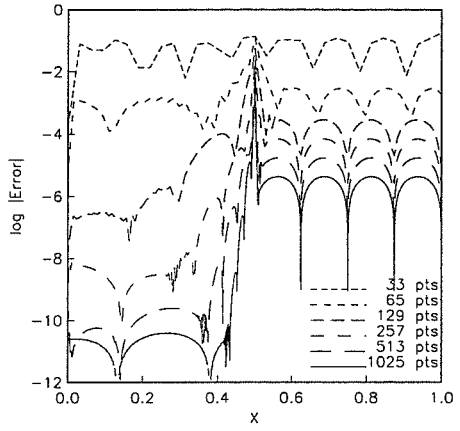

Figure 10. Pointwise solution error after correcting for the numerical phase shift, with LIN-6-4

TABLE 2. Phase shift verses $\frac{U_L}{U_R}$.

$\frac{U_L}{U_R}$	$\frac{\delta}{\Delta x}$
4/1	0.2351
2/1	0.08412
1/2	0.1700
1/4	0.9674

6. Discussion

In this work, and elsewhere [1], we provide a systematic study of the effects of discontinuities on solution accuracy. We focus on the ENO-4-3 and LIN-6-4 formulations as being representative of high-order nonlinear and linear schemes in use today. We show for higher-order formulations, that the solution accuracy is strongly dependent on the mathematical character of the governing equations, and only weakly dependent on the numerical method.

Specific conclusions include: 1) The quasi-one-dimensional Euler equations admit design accuracy away from a steady discontinuity. The ENO-4-3 results are significantly better than the LIN-6-4 results for the steady case. 2) The unsteady Burgers' equation admits design accuracy away from a discontinuity, in contrast to the unsteady Euler equations. Equations that focus information at the discontinuity maintain design accuracy away from

that discontinuity. 3) The unsteady Euler equations are first-order accurate downstream of a discontinuity. The ENO-4-3 and LIN-6-4 schemes achieve similar solution accuracy downstream of the shock for the sound-shock interaction problem.

We use a linear model problem with a discontinuous wave speed, to study the nature of discontinuity related solution error. We recover first order solution error downstream of a discontinuity in the linear case, and quantify the error as being phase related to leading truncation order. Second-order results, are obtained by post-processing the solution with the known phase shift. It is doubtful whether this post-processing step is general for systems of equations in multiple dimensions.

Research continues in several directions. It is questionable whether design accuracy can be obtained for the discontinuous steady Euler equations in multiple spatial dimensions. (The mathematical character of the 2-D steady and the 1-D unsteady Euler equations is similar, and we know the later to be first-order downstream of discontinuities). Further investigation continues into the relative merits of high-order-accurate shock-capturing schemes, and in particular, the relative merits of linear and non-linear schemes. Attention focuses on shock resolution, design accuracy, and computational efficiency. Work continues into developing general techniques which recover design accuracy in the presence of discontinuities. Linear schemes suffer from a first order phase shift which is wave-speed jump dependent. It is possible, therefore, to correct the time-dependent solution for the full Euler equations making use of phase shift information.

We conclude by noting that the inability to recover design accuracy downstream of a discontinuity is not a proof of inherent first-order accuracy; but rather only a demonstration that design accuracy has not been found!

References

1. Casper, J., and Carpenter, M. H., "Computational Considerations for the Simulation of Shock-Induced Sound," NASA TM 110222, Dec., 1995, to appear *SIAM J. of Sci. Comput.*, Vol. 19, No. 1, January, 1998.
2. Harten, A., Engquist, B., Osher, S., and Chakravarthy, S., "Uniformly High Order Accurate Essentially Non-Oscillatory Schemes III," *Journal of Computational Physics*, Vol. 71, No. 2, 1987, pp. 231-323.
3. Shu, C. and Osher, S., "Efficient Implementation of Essentially Non-Oscillatory Shock-Capturing Schemes," *Journal of Computational Physics*, Vol. 77, No. 2, 1988, pp. 439-471.
4. Rogerson, A. and Meiberg, E. "A Numerical Study of the Convergence Properties of ENO Schemes," *Journal of Scientific Computing*, Vol. 5, No. 2, 1990, pp. 151-167.
5. Shu, C., "Numerical Experiments on the Accuracy of ENO and Modified ENO Schemes," *Journal of Scientific Computing*, Vol. 5, No. 2, 1990, pp. 127-150.
6. Atkins, H., "High-Order ENO Methods for the Unsteady Navier-Stokes Equations," AIAA 91-1557, June, 1991.
7. Casper, J., Shu, C. W., and Atkins, H., "A Comparison of Two Formulations for